Universitat Autònoma de Barcelona

Development of Advanced Silicon Sensors for Neutron Detection and Microdosimetry

Sergi Esteban Martí

PhD Thesis

Development of Advanced Silicon Sensors for Neutron Detection and Microdosimetry

Author: Sergi Esteban Martí

Director:
Dra. Celeste Fleta Corral

Tutor:
Prof. Enrique Fernández Sánchez

PhD program in Physics

Physics department - Science faculty

2016

La Dra. Celeste Fleta Corral, investigadora de l'Institut de Microelectrònica de Barcelona, IMB-CNM (CSIC), i el Prof. Enrique Fernández Sánchez, cetedràtic de la Universitat Autònoma de Barcelona,

CERTIFIQUEN:

que la memòria de la present tesi doctoral titulada **"Development of advanced silicon sensors for neutron detection and microdosimetry"** presentada per Sergi Esteban Martí per a optar al grau de Doctor en Física per la Universitat Autònoma de Barcelona ha estat realitzada sota la seva direcció dins l'Institut de Microelectrònica de Barcelona del Consell Superior d'Investigacions Científiques.

Barcelona,
Setembre 2016

L'autor:

Sergi Esteban Martí

Directora de Tesi:

Dra. Celeste Fleta Corral

Tutor de Tesi:

Enrique Fernández Sánchez

Abstract

This thesis presents the development of advanced silicon sensors fabricated at IMB-CNM for neutron detection applications and for microdosimetry measurements of hadron therapy ion beams.

The accurate detection of neutrons has great interest for the medical community, for homeland security and for many other different fields such as material science or space exploration. Given their biological effect, neutron detection is essential to control, for example, the neutron flux produced during a radiotherapy or hadrontherapy treatment to minimize the patient's risk of secondary radiation-induced tumours. Moreover, for national security purposes, neutron detection is crucial to elude radiological threats since the nuclear materials, that could be used to assemble nuclear weapons or dirty bombs, are a significant source of fission neutrons. These applications mostly rely on ^{3}He gas proportional counters but due to the shortage of this gas, a replacement technology for neutron detection is required in the near future.

The presented sensors in this thesis for neutron detection are the ultra-thin 3D (U3DTHIN) and the microstructured (MS) sensors, which are covered and filled respectively with a thermal neutron converter material. The U3DTHIN sensors are only 10 or 20 µm thick, allowing for a high gamma rejection, which is necessary to discriminate the signal coming from the neutrons in a mixed neutron-gamma ray environment. The MS

sensors consist of an array of microchannels etched inside the silicon bulk and filled with a converter material. They lead to an improvement of the neutron detection efficiency due to the increased contact area between the silicon sensitive volume and the converter material.

Hadron therapy is an expanding branch of external radiation therapy for treating cancer using protons or heavy ion beams. The commissioning of such beams, to lead to a more accurate treatment plan, requires a complete characterization of the radiation quality (i.e. particle types and their energy spectra) that results from microdosimetric measurements. To perform these measurements, the presented sensors in this thesis are the U3DTHIN and the 3D cylindrical microdosimeter. The U3DTHIN, already introduced for neutron detection, is also used for such measurements due to its thin thickness, while the 3D cylindrical microdosimeter was manufactured specifically for microdosimetry measurements. This new generation device consists of an array of micro-sensors that have 3D-cylindrical electrodes resulting in a well-defined micrometric radiation sensitive volume.

The research presented in this work includes the fabrication processes of the sensors, their electrical characterization, the GEANT4 simulations to optimize the designs and to validate the experimental results and the experimental tests performed at different irradiation facilities.

A la meva família

Agraïments

En aquesta secció voldria dedicar unes senzilles paraules a totes aquelles persones que han fet possible aquesta tesi.

Primerament voldria donar les gràcies al Prof. Manuel Lozano i al Dr. Giulio Pellegrini per haver-me donat l'oportunitat de realitzar el doctorat al Centre Nacional de Microelectrònica de Barcelona, i iniciar-me així al món de la recerca.

Voldria donar les gràcies també a la Dra. Celeste Fleta, la directora de tesi, per confiar en mi i donar-me llibertat a l'hora de realitzar tot tipus de mesures i experiments. Gràcies Celeste per inculcar-me precisió i coherència en el meu treball cientfic i gràcies també per tots aquells entretinguts viatges que hem compartit durant aquests quatre anys de doctorat.

Gràcies a tots els membres del Grup de Detectors de Radiació per haver-me acollit com un més i pel bon ambient que regnava en totes les reunions. Voldria En particular, voldria agrair a la Dra. Consuelo Guardiola i al Dr. David Quirion la seva total predisposició per discutir idees i per aclarir dubtes. Gràcies Consuelo per mostrar-me el camí a seguir en els detectors de neutrons, i gràcies David per introduir-me en l'apassionant món de la sala blanca. Gràcies Victor Benítez, Marta Baselga i Pablo Fernández per ajudar-me tant en els meus inicis al CNM i gràcies per intentar fer-me veure la programació com una cosa divertida.

Vull donar també les gràcies al professor Faustino Gómez, amb qui he compartit diversos experiments, pel seu saber fer, pel seu entusiasme i per

les seves ganes de compartir coneixement.

Gràcies també a tots aquells amb els qui he compartit àpats dia rere dia: gràcies Carlos Jumilla per entretenir els nostres dinars amb recomanacions i crítiques de pel·lícules, gràcies Daniela Bassignana per ensenyar-me a no cuinar macarrons a la carbonara, gràcies David Quirion per no preguntar resultats en jornades dolentes, gràcies Celeste Fleta per compartir idees i visions de diverses sèries de televisió, gràcies Mar Carulla per la teva amistat i per les teves postres casolanes, gràcies Xavier Fernández per deixar-nos gaudir de la teva presencia de tan en tan, gràcies Marta Baselga per aportar tocs orientals als nostres dinars, i gràcies Rosela Zaffino per compartir els teus estudis d'art urbà.

Als companys de despatx: la Carolina, la Núria, la Maribel, en Javier i en Juan Pablo, pel bon ambient de treball i les converses disteses.

Als companys del CNM: la Maria José, la Mar, la Laura, la Carme, en Gonzalo, en Txema, en Joa... entre molts d'altres amb els qui he compartit infinitat de divertidíssims moments tan dins com fora del centre, i amb els qui estic segur que continuarem trobant-nos per explicar batalles i compartir cerveses fins altes hores de la nit.

Finalment un especial agraïment a la Helen i a la meva família ja que, tot i no rebre massa informació del meu dia a dia, sempre han confiat en mi i en tot el que feia.

Contents

List of Figures

List of Tables

Part I

General Introduction

1

Semiconductor radiation detectors

The first semiconductor detector was made in 1951 by McKay, who demonstrated the detection of alpha particles using a germanium pn-diode [1]. Currently, semiconductor radiation detectors are used in many science fields, such as nuclear physics, medical imaging, astrophysics, material studies, security systems, etc.

In many radiation detection applications the use of a solid detection medium is of great advantage. For example, for the measurement of high-energy electrons or gamma rays, detector dimensions can be kept much smaller than the equivalent gas-filled detector because solid densities are

some 1000 times greater than that for a gas.

Scintillation detectors provide a solid detection medium, however one of their major limitation is the relatively poor energy resolution[1]. Other option are the semiconductor materials, which present properties that make them more suitable for radiation detection. Among these properties are: compact size, relatively fast timing characteristics, very large number of charge carriers generated per unit energy lost by the incident radiation and an effective active volume that can be varied to match the requirements of the application.

Depending on the type of radiation and on the information to be obtained, different semiconductor materials and configurations can be used. For example, for heavy ions and low energy charged particles it is enough with very thin detectors, as the range of such particles in most solids is typically lower than 100 microns. In the case of beta particles, the thickness of the material must be increased. Thicknesses of several centimeters or more can be needed for gamma rays due to their extremely high penetration characteristics. In the case of neutrons, their detection is made via secondary particles (like alphas, betas, gamma-rays, X-rays, etc.) as neutrons produce only indirect ionization, so materials with high interaction cross sections with neutrons are required.

The large majority of semiconductor radiation detectors presently in use are manufactured from either silicon or germanium. The widespread popularity of these materials is attributable to their excellent charge carrier transport properties, which allow the use of large crystals without excessive charge carrier losses from trapping and recombination. Silicon is the most investigated and used semiconductor in microelectronics technology and in the detection of charged particle while germanium is more widely used in gamma-ray measurements. Diamond is also a good candidate for radiation detectors due to its properties of radiation hardness,

[1]Semiconductor detectors used in alpha spectroscopy can have an energy resolution less than 1%, whereas scintillation detectors used in gamma-ray spectroscopy normally show an energy resolution in the range of 5-10%.

high carrier mobility and high band gap, however it is expensive and its availability is limited. The applications of diamond detectors are mainly on radiation therapy dosimetry because its atomic number (Z=6), close to the effective atomic number of a soft tissue (Z= 7.4), makes diamond nearly tissue equivalent. The main characteristics of intrinsic silicon, germanium and diamond are presented in Table 1.1.

Table 1.1: Properties of intrinsic Silicon, Germanium and Diamond semiconductors at T=300 K . Data from [2].

	Si	Ge	Diamond
Atomic number	14	32	6
Atomic weight	28.09	72.60	12.01
Density [g/cm^3]	2.33	5.32	3.51
Dielectric constant	11.9	16.2	5.7
Gap energy [eV]	1.12	0.66	5.47
Intrinsic carrier density [cm^{-3}]	$1.4 \cdot 10^{10}$	$2.4 \cdot 10^{13}$	$< 10^3$
Intrinsic resistivity [Ωcm]	$2.3 \cdot 10^5$	47	$> 10^{12}$
Electron mobility [cm^2/V/s]	1450	3900	1800
Hole mobility [cm^2/V/s]	450	1900	1200
Mean E to create e^-h^+ pair [eV]	3.63	2.96	13.1

Compound semiconductors are also useful as radiation detectors due to the possibility of achieving a wide range of stopping powers and band gaps by mixing different elements. However, these detectors have much higher trap densities than the elemental semiconductors and hence, shorter lifetimes of the created charge [3]. The most common compound semiconductors are derived from groups III and V (like GaAs or InP) and groups II and VI (like CdTe) of periodic table.

Silicon is a type IV material (four valence electrons) and it can be doped with impurities to alter its electrical properties. One can produce *n-type* silicon (Figure 1.1b) by adding a type V material like phosphorus (donor impurity; excess of electrons) or produce *p-type* silicon (Figure

1.1c) by adding type III material like boron (acceptor impurities; excess of holes).

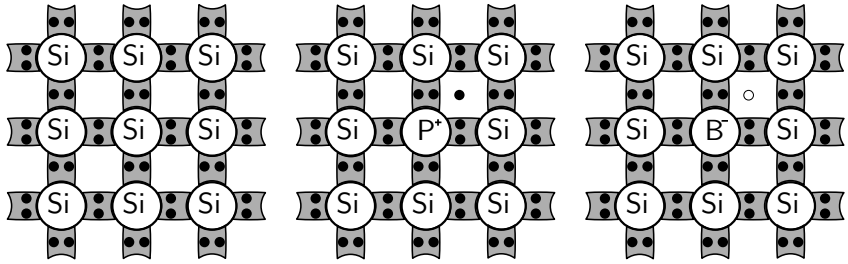

(a) intrinsic silicon **(b)** n-type silicon **(c)** p-type silicon

Figure 1.1: Two-dimensional schematic bond representation - (a) silicon crystal; (b) silicon crystal with one atom replaced by a phosphorous atom and (c) silicon crystal with one atom replaced by a boron atom.

In this work different types of silicon detectors developed and manufactured at CNM-Barcelona for different applications will be presented.

1.1 Semiconductor detectors

A semiconductor detector is usually a silicon or germanium p-i-n (PIN) junction operating in reverse bias mode. A PIN diode consists in a wide and lightly doped intrinsic[1] semiconductor between p-type and n-type extrinsic semiconductors, which are highly doped (Fig. 1.2). Both p-type and n-type regions are used for ohmic contacts with metalization.

When a p-type and an n-type semiconductors are brought into contact, holes from the p side will diffuse into the n region, leaving negatively charge atoms behind, and simultaneously electrons from the n side will diffuse into the p region, leaving positively charged atoms. This creates and electric field that counteracts the diffusion and sweeps away any mo-

[1]In practice, the intrinsic region does not have to be truly intrinsic but only has to be highly resistive (lightly doped *p-* or *n-region*)

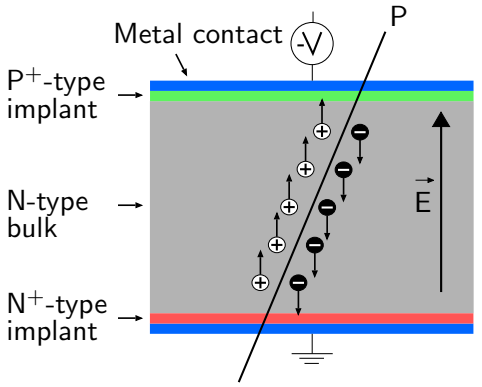

Figure 1.2: Schematic of a PIN diode - Sketch of a PIN diode that is transversed by a particle (P), which creates e-h pairs into the diode bulk. The diode is reversely biased to separate the e-h pairs and drift them to their respective electrodes. Figure adapted from [4].

bile charge carriers in the region around the boundary. This region is called *space charge region* or *depleted region* and will act as the active area of the detector.

The fundamental information carriers of semiconductor detectors are electron - hole pairs (e^-h^+ pairs), which are produced by ionization along the path taken by the particle (primary or secondary) through the active area of the detector. The motion of these e^-h^+ pairs in an electric field generates the basic electrical signal from the detector. The average energy necessary to create an e^-h^+ pair in semiconductors is in the range of few eV (Table 1.1), 10 and 100 times smaller than the required for gaseous and scintillation detectors respectively so the energy resolution of semiconductor neutron detectors is higher (see section 1.2.1).

The reverse bias mode consists on applying a positive polarity voltage on the n-side and a negative on the p-side. In this configuration the depleted region (active volume of the detector) is increased and the current flow through the detector is decreased. Silicon sensors are usually operated in reverse bias mode.

When an incoming ionizing radiation passes through the detector, the

e^-h^+ pairs created in the active volume induce an image charge on the electrodes [5] resulting in a small electrical current pulse[1]. Then, that pulse is processed in an external readout electronics and, as the total number of e-h pairs created is proportional to the energy transmitted by the radiation to the semiconductor, the energy of the incident radiation can be found. The e^-h^+ pairs created in the non-depleted zone recombine with free majority carriers and are lost.

The width of the depleted region, W_{dep}, depends on the reverse bias applied and can be calculated as:

$$W_{dep} = \sqrt{\frac{2\varepsilon}{q}(\frac{1}{N_a} + \frac{1}{N_d})(\phi_{bi} - V_{bias})} \tag{1.1}$$

where q is the charge of the electron, ε the product of the vacuum permittivity (ε_0) and the relative permittivity of the semiconductor ($\varepsilon_r = 11.8$ for silicon), ϕ_{bi} the built-in voltage of the diode, V_{bias} the bias applied, and N_a and N_d the concentrations of donors and acceptors respectively.

As already stated, the junction is usually realized by a shallow and highly doped ($N_a > 10^{18}\text{cm}^{-3}$) p^+ implant in a low-doped ($N_d \approx 10^{12}\text{cm}^{-3}$) bulk material, therefore the term $1/N_a$ in Equation 1.1 can be neglected, meaning that the resulting asymmetric junction depletes into the bulk. In addition, the built-in voltage is normally considered negligible because it is orders of magnitudes lower than the bias voltage applied. It is worth to say that the variable active volume of semiconductor detectors (W_{dep} depends on the voltage applied) is unique among radiation detectors.

If the voltage V_{bias} is increased far enough, the depletion region eventually extends across virtually the entire thickness of the detector and it results in a *fully depleted* (or *totally depleted*) detector. In that case, V_{bias} is known as the full depletion voltage (V_{FD}) and it is calculated by:

$$V_{FD} = \frac{q|N_{eff}|d^2}{2\varepsilon} \tag{1.2}$$

[1]The signal from the charged particles detected in the silicon is typically of the order of picoamperes.

being $N_{eff} = N_d - N_a$ the effective density and d the full depletion width. At higher bias voltage an electrical breakdown, where the current starts to increase dramatically, is observed.

As the depleted region is free of mobile charge, it may be assimilated to a capacitor bounded by the conducting p- and n-type semiconductor on each side. This capacitance per unit area for a diode with planar geometry is given by:

$$C_{bulk}^2 = \frac{\varepsilon}{W_{dep}} = \begin{cases} \frac{q|N_{eff}|}{2\varepsilon V_{bias}} & \text{if } V_{bias} < V_{dep} \\ \frac{\varepsilon^2}{d^2} & \text{if } V_{bias} > V_{dep} \end{cases} \tag{1.3}$$

The capacity-voltage curve is used as a standard method to experimentally determine V_{FD}. A mode of example, a silicon diode with 100 µm thickness has a capacitance of about $1\,\mathrm{pF/mm^2}$.

1.2 Radiation interaction with matter

In general, ionizing radiation is any electromagnetic or particulate radiation capable of producing ions, directly or indirectly, by interaction with matter. Directly ionizing particles are charged particles having sufficient kinetic energy to produce ionization by collisions, and indirectly ionizing particles are uncharged particles which can liberate directly ionizing particles or can initiate nuclear transformations.

Radiation interaction with semiconductor materials produces the creation of e^-h^+ pairs that can be detected as electric signal. When the incident ray consists of charged particles, ionization may occur along the path of flight by many interactions with the orbital electrons. In presence of uncharged radiation, such as X-ray or neutrons, a first interaction with either a target electron or with the semiconductor nucleus must take place in order to get a detected electric signal.

1.2.1 Creation of e^-h^+ pairs in semiconductors

The energy ε required to create an electron-hole pair in a given semiconductor at a given temperature is independent of the type and the energy[1] of the ionizing radiation and is roughly proportional to the band-gap, yielding a good fit to the expression [7]:

$$\varepsilon \approx 2.8E_g + 0.6\,\text{eV} \tag{1.4}$$

Since the forbidden gap value is 1.115 eV for silicon (see Table 1.1) it is clear that not all the energy of the ionizing radiation is spent in electron-hole creation. Energy can be absorbed by either lattice excitation, i.e. phonon production (with no formation of mobile charge), or ionization, i.e. formation of a mobile charge pair.

For a fixed absorbed energy, fluctuations always exist in the fraction of energy that ends up in phonon generation and in e^-h^+ creation. In the particular case of silicon about 70% of the ionization energy goes into phonon excitations and only 30% into signal charge.

Fluctuations in the signal charge: The Fano factor

A key characteristic of signal sensors is not just the magnitude of the signal, but also the fluctuations of the signal for a given absorbed energy. Both determine the minimum signal threshold and the relative resolution of the detector (ΔE/E). For a given radiation energy, the signal will fluctuate around a mean value N given by:

$$N = \frac{E}{\varepsilon} \tag{1.5}$$

with E the energy absorbed in the detector and ε the mean energy spent for creating an electron-hole pair.

The variance in the number of signal electrons (or holes) N is given by

$$\langle \Delta N^2 \rangle = F \cdot N = F\frac{E}{\varepsilon} \tag{1.6}$$

[1]For very low radiation energy in the few-eV range (when $E \approx E_g$), the energy required to create an electron-hole pair is expected to be energy-dependent [6].

with F the Fano factor (F).

For good energy resolution, one would like the Fano factor to be as small as possible. The true vale of F for silicon and germanium is still unknown; theoretical values of F in semiconductors have tended to disagree with experimental results[1] [8], however by assuming a value of $F = 0.1$ in both silicon and germanium, satisfactory agreement with measured results is found in most cases.

1.2.2 Electromagnetic radiation

Although a large number of possible interaction mechanisms are know for gamma-rays in matter, only three major types play an important role in radiation measurements: the photoelectric effect, the Compton scattering, and the pair production (Figure 1.3).

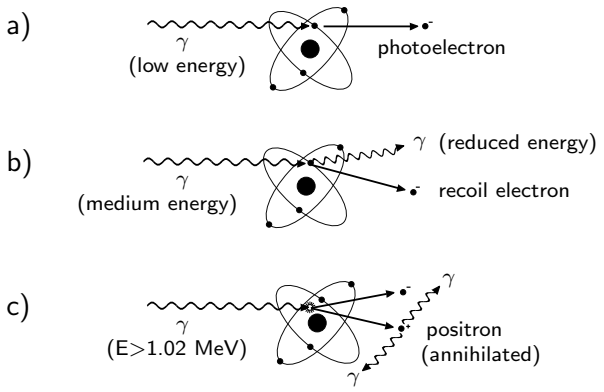

Figure 1.3: Electromagnetic interaction with matter - (a) photoelectric effect; (b) Compton effect; (c) pair production

1.2.2.1 Photoelectric effect

The photoelectric effect converts a single photon into a single free electron. When the photon interacts with a bound electron, the photon can be

[1] Experimentally, the Fano factor is derived from an analysis of the distribution of pulse heights in a detector resulting from exposure to a monochromatic X-ray source.

completely absorbed and the electron emerges with a kinetic energy (E_k) that corresponds to:

$$E_k = h\nu - E_b \tag{1.7}$$

where $h = 4.136 \cdot 10^{-15}$eV s is the Planck's constant, ν is the frequency of the photon and E_b is electron binding energy.

In addition to the photoelectron, the interaction also creates an ionized absorber atom with a vacancy in one of its bound shells. This vacancy is quickly filled through the capture of a free electron from the medium and/or through a rearrangement of electrons from other shells of the atom.

The photoelectric effect is the predominant interaction mechanism for low energy photons (few eV to some keV) and for materials of high atomic number (Z).

1.2.2.2 Compton scattering

In Compton scattering the incident beam interacts with an electron, transfers to it some of its energy and is deflected an angle θ with respect to its original direction. The scattered radiation wavelength (λ') is linked both to the wavelength of the incident beam (λ) and to the deflected angle according to the following expression:

$$\Delta\lambda = \lambda' - \lambda = \lambda_e(1 - \cos\theta) \tag{1.8}$$

where $\Delta\lambda$ is the wavelength Compton shift and λ_e is the electron Compton wavelength.

It is evident that $\Delta\lambda$ grows as the scattering angle increases and it reaches the maximum value for $\theta = \pi$. The energy transferred from the incident beam to the electron can vary from zero to a large fraction of the incident ray energy, according to the following relation:

$$h\nu' = \frac{h\nu}{[1 + \frac{h\nu}{m_0c^2}(1 - \cos\theta)]} \tag{1.9}$$

with $h\nu$ the outgoing electron energy, m_0c^2 the electron rest mass (0.511 MeV) and h the Planck's constant.

The Compton scattering is the predominant interaction mechanism for photons with energies between few keV and 1 MeV.

1.2.2.3 Pair production

In pair production, a high-energy photon near a nucleus gives up its energy to produce an electron-positron pair. The photon energy goes into the rest-mass and the kinetic energy of the electron-positron pair. The minimum energy necessary for this effect is set by elementary relativistic considerations at the value of 1.022 MeV (amount equivalent to two electron rest masses). The probability of this interaction remains very low until the gamma ray energy approaches several MeV and therefore pair production is predominantly confined to high-energy gamma-rays.

1.2.2.4 Gamma ray attenuation coefficient

Each electromagnetic interaction processes previously described can be characterized by a probability of occurrence per unit path length in the absorber. This probability, denoted by μ and having dimensions of an inverse length is called the *linear attenuation coefficient* and it is calculated as:

$$\mu = \tau + \sigma + \kappa \tag{1.10}$$

where τ, σ and κ are the probability of photoelectric, Compton and pair production interactions respectively.

Gamma ray photons can also be characterized by their *mean free path* λ, ($\lambda = \mu^{-1}$), defined as the average distance traveled in the absorber before an interaction takes place. As the coefficient μ is dependent on the material density, a more convenient figure is introduced: the *mass attenuation coefficient*, which is defined as μ/ρ with ρ denoting the medium density. Figure 1.4 shows the mass attenuation coefficient of silicon and germanium as a function of the photon energy.

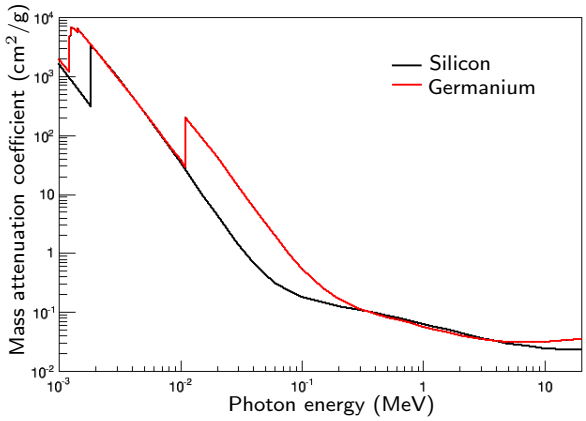

Figure 1.4: Values of the mass attenuation coefficient: - μ/ρ of silicon and germanium as a function of photon energy. Data taken from NIST [9]

1.2.3 Heavy charged particles

Heavy charged particles lose energy by Coulomb or nuclear interactions within the absorbing material. The collision of heavy charged particles with free and bound electrons results in the ionization or excitation of the absorbing atom, whereas the interactions with nuclei occur only rarely and they are not normally significant in the response of radiation detectors.

Since the maximum energy that can be transferred from a charged particle to an electron in a single collision (T_{max}) is a small fraction of the total incident beam energy, many interactions occur during the traveling of radiation through the matter. Electrons ejected during their motion can produce other ion pairs or secondary electrons. As a consequence of interactions, the charged particle velocity decreases until the particle is stopped.

The rate at which charged particles lose energy as they travel through a given material is called the *stopping power (S)* of the material:

$$S = -\frac{dE}{dx} = S_{electronic} + S_{nuclear} \approx S_{electronic} \tag{1.11}$$

where the *electronic stopping power* for moderately relativistic charged

heavy particle is well-described by the Bethe equation:

$$-\langle\frac{dE}{dx}\rangle = Kz^2\frac{Z}{A}\frac{1}{\beta^2}\left[\frac{1}{2}\ln\frac{2m_ec^2\beta^2\gamma^2T_{max}}{I^2} - \beta^2 - \frac{\delta(\beta\gamma)}{2}\right] \tag{1.12}$$

$\langle dE/dx\rangle$ = mean rate of energy loss per unit length
$K = 4\pi N_{Av}r_e^2m_ec^2 = 0.307075$ MeVcm^2/mol
z = charge of incident particle
Z = atomic number of absorber
A = atomic mass of absorber [gmol^{-1}]
$\beta\gamma$ = relativistic parameters
m_ec^2 = electron mass $\times$ c^2
I = mean excitation energy in eV.
T_{max} =maximum kinetic energy transfer to the electron in one single collision.
$\delta(\beta)$ = density effect correction to ionization energy loss

Equation 1.12 describes the mean rate of energy loss due to ionization or excitation processes, however this equation is valid only in the region of $0.1 \lesssim \beta\gamma \gtrsim 1000$. At the lower limit the projectile velocity becomes comparable to atomic electron velocities and the energy loss increases with the energy till reaching a maximum when the particle velocity is equal to the typical electron velocity. After this maximum, the energy loss decreases according to the Bethe equation. At the upper limit radiative effects begin to be important and other corrections need to be done [10].

1.2.4 Electrons

Electrons lose energy by Coulomb interactions or by radiative processes within the absorbing material. These radiative losses take the form of *bremsstrahlung* radiation, which can emanate from any position along the electron track.

The collision of electrons with matter can cause large deviations in the electron path because its mass is equal to that of the orbital electrons with

which it is interacting, and a much larger fraction of its energy can be lost in a single encounter.

The total linear stopping power for electrons is the sum of the collisional losses (ionization and excitation) and radiative losses:

$$\frac{dE}{dx} = \left(\frac{dE}{dx}\right)_{collisional} + \left(\frac{dE}{dx}\right)_{radiative} \tag{1.13}$$

where the collisional loses are similar to the electronic interaction between charged particles and electrons discussed above (Equation 1.12).

The ratio of the two contributions to the stopping power depends on the atomic number of the material, Z, and the electron kinetic energy, E_k:

$$\frac{S_{\text{radiative}}}{S_{\text{collisional}}} \approx \frac{ZE_k}{800\,\text{MeV}} \tag{1.14}$$

which indicates that the radiative contribution is only significant for large atomic numbers ($Z \approx 80 - 90$) and high electron energies ($E \approx 10 - 100\,\text{MeV}$).

1.2.5 Neutron interactions

Neutrons do not interact by Coulomb force with the orbital electrons of the medium and consequently they are highly penetrating. A neutron will move through the material along a straight line with a constant energy until it undergoes a strong interaction with a nucleus via nuclear forces[1]. That interaction may be through scattering (elastic and inelastic) or absorption processes. (Figure 1.5)

The cross-section of each interaction depends on the target type, on the kinetic energy of the incident neutron and, to a lesser extent, on the target temperature and on the relative angle between the target nucleus and the incident neutron. Many neutron interactions are characterized by resonances, where the cross section for such interaction shows a pronounced peak at a particular energy. At the resonance, the cross section

[1]Neutrons only have a very small interaction probability with electrons through their magnetic dipole moment that can be ignored.

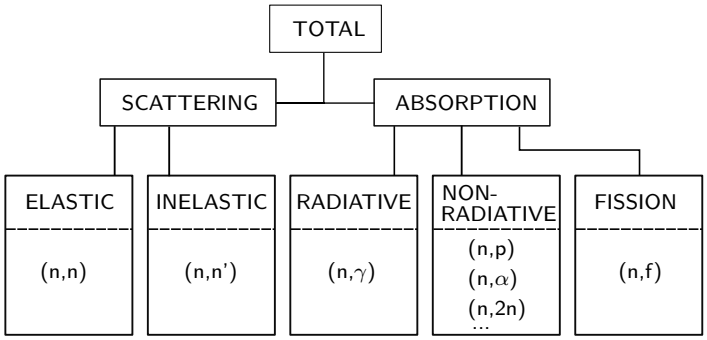

Figure 1.5: Neutron interacting processes.

can be many orders of magnitude larger than at slightly higher or lower energy. This is illustrated in Figure 1.6.

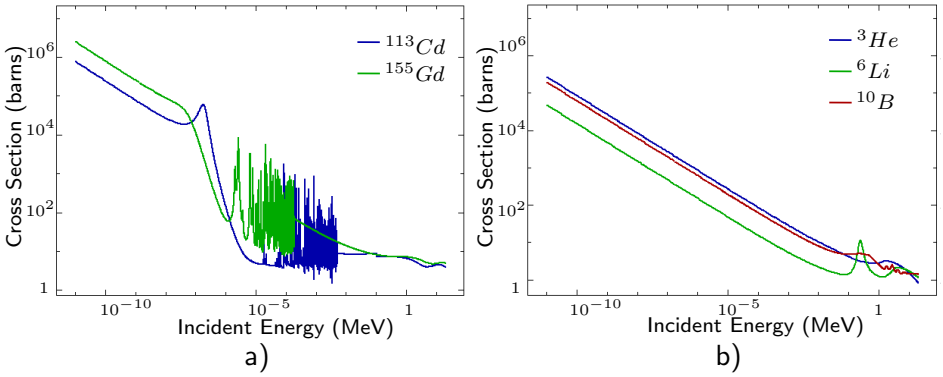

Figure 1.6: Total neutron cross-section of ^{113}Cd, ^{155}Gd, ^{3}He, ^{6}Li and ^{10}B - a) the cross-section become roughly constant at energies higher than 0.01 MeV and show resonance peaks from 1 eV to 0.01 MeV; on b) the cross-section become very large at thermal energies and decrease inversely proportional to the neutron energy. Data obtained from the ENDF database [11].

1.2.5.1 Neutron scattering

The neutron scattering interaction involves changing the energy and direction of the incident neutron, but the target nucleus remains with the

same number of protons and neutrons. The scattering can be subdivided into elastic and inelastic.

It is elastic scattering if the total kinetic energy of the incident neutron and target nucleus is conserved in the center-of-mass frame, and it is inelastic scattering if the nucleus undergoes an internal rearrangement into an excited state from which it eventually releases radiation. In inelastic scattering the total kinetic energy of the outgoing neutron and nucleus is less than the kinetic energy of the incoming neutron due to part of the original kinetic energy is used to place the nucleus into the excited state.

Neutron elastic scattering: Elastic scattering, A(n,n)A, is the most likely interaction between lower energy fast neutrons and low Z materials. For a neutron of kinetic energy E encountering a nucleus of atomic weight A, the average energy loss is $2EA/(A+1)^2$. This expression shows that in order to reduce the speed of neutrons (that is, to moderate them) with the fewest number of elastic collisions, target nuclei with small A should be used. By using hydrogen, with $A = 1$, the average energy loss has its largest value of $E/2$.

A neutron with 2 MeV of kinetic energy will (on average) have 1 MeV left after one elastic collision with a hydrogen nucleus, 0.5 MeV after a second such collision, and so on. To achieve a kinetic energy of only 0.025 eV would take a total of about 27 such collisions. A neutron of energy 0.025 eV is roughly in thermal equilibrium with its surrounding medium and is considered a *thermal neutron*. In general, after n elastic collisions, the neutrons energy is expected to be:

$$E_n = E_0[(A^2+1)/(A+1)^2]^n \tag{1.15}$$

Neutron inelastic scattering: The inelastic scattering, A(n,n')A*, is the most likely interaction between high energy (>1 MeV) neutrons and high Z materials. It is not easy to write an expression for the average energy loss because it depends on the energy levels within the nucleus,

but the net effect on the neutron is again to reduce its speed and change its direction.

If all the excited states of the nucleus are too high in energy to be reached with the energy available from the incoming neutrons, inelastic scattering is impossible. To cause inelastic scattering neutron energies from 0.5 to 5 MeV are necessary for light nuclei, whereas for heavy nuclei, neutron energies in the keV range are enough. In particular, the hydrogen nucleus does not have excited states, so only elastic scattering can occur in that case.

1.2.5.2 Neutron absorption (or capture)

Instead of being scattered by a nucleus, the neutron may be absorbed or captured. Three main categories of neutron absorption can be distinguished: radiative capture, non-radiative capture and fission.

Radiative capture: In the radiative capture process, A(n,γ)A+1, the neutron is captured by the target nucleus giving a compound nucleus in an excited state which decays emitting γ-rays. It can occur for a wide range of neutron energies and it is always an exoenergetic reaction (positive Q-values). One of the most common radiative capture takes place with hydrogen:

$$ {}^{1}_{1}H + n \rightarrow ({}^{1}_{2}H)^{*} \rightarrow {}^{1}_{2}H + \gamma \tag{1.16} $$

Non-radiative capture: In non-radiative capture reactions the resulting nuclei ejects or charged particles or neutrons (the emission of only one neutron is indistinguishable from a scattering event). These reactions take place by quantum tunneling since the energy of the incident particle is usually below the coulomb barrier of the compound nucleus.

Most of the non-radiative capture reactions are endoenergetic but there are some interesting nucleis in neutron detection that can undergo an exoenergetic reaction. Some of these interesting reactions of neutron capture are listed in Table 3.2.

Fission: When a neutron interacts with a heavy nucleus ($Z \geq 92$), the compound nucleus may split into two daughter nucleis of lighter mass. This process always releases one or more fast neutrons that, in turn, can trigger other fissions in a self-sustained nuclear chain reaction. Controlled chain reactions are usually used in nuclear reactors for research and power generation. Fission reactions are likely for uranium (^{233}U and ^{235}U), plutonium (^{239}Pu), thorium (^{232}Th) and higher mass actinides.

Bibliography

[1] Kenneth G McKay. **Electron-Hole Production in Germanium by Alpha-Particles**. *Phys. Rev.*, **84**(4):829–832, nov 1951. 3

[2] Gerhard Lutz. *Semiconductor radiation detectors. Device Physics*, **170** of *Accelerator Physics Series*. Springer, 1999. 5

[3] Alan Owens. **Semiconductor materials and radiation detection**. *Journal of Synchrotron Radiation*, **13**(2):143–150, mar 2006. 5

[4] Daniela Bassignana. *New technologies of silicon position-sensitive detectors for future tracker systems*. PhD thesis, 2012. 7

[5] Simon Ramo. **Currents Induced by Electron Motion**. *Proceedings of the IRE*, **27**(9):584–585, 1939. 8

[6] Helmuth Spieler. *Semiconductor Detector Systems*. Oxford University Press, 2007. 10

[7] Alan Owens and A Peacock. **Compound semiconductor radiation detectors**. **531**:18–37, 2004. 10

[8] Alan Owens, G W Fraser, and Kieran J McCarthy. **On the experimental determination of the Fano factor in Si at soft X-ray wavelengths**. *Nuclear Instruments and Methods in Physics Research Section A: Accelerators, Spectrometers, Detectors and Associated Equipment*, **491**(3):437–443, 2002. 11

[9] **NIST. Physical reference data website**. 14

[10] K.a. Olive. **Review of Particle Physics (Electroweak Model)**. *Chinese Physics C*, **38**(9):090001, 2014. 15

[11] **ENDF. Evaluated Nuclear Data File (ENDF)**. 17

2

Monte Carlo simulations of radiation transport

The Monte Carlo (MC) method can generally be described as a broad class of computational algorithms that rely on repeated random sampling to obtain numerical results. It was developed in the 1940s by John von Neumann and Stanislaw Ulam [1] to solve with statistical approximations complex integro-differential equations that appear in several fields of mathematics and physics. With the advances in computer technology and power, computers are able to perform millions of simulations quickly. Hence, MC methods have become widely used to simulate problems with a large number of coupled degrees of freedom that are difficult and consume

too much time to be resolved with classic analytic methods.

The technique of random sampling to solve mathematical problems is known from 1770, but only with the advent of quantum mechanics, in which matter-radiation interactions were interpreted using cross sections as probabilities, the Monte Carlo technique was applied to nuclear and ionizing radiation physics. In the last decades, there has been an enormous increase and interest in the use of Monte Carlo techniques in all aspects of medical physics, including radioprotection, ionizing radiation dosimetry, nuclear medicine, diagnostic radiology, radiotherapy, etc.

2.1 Introduction to MC method

In general, a Monte Carlo simulation of particle transport requires a great deal of information regarding the interaction properties of the particle and the media through which it travels. The main steps involved in ionizing radiation transport trough a certain media are given in Figure 2.1. A particle history starts by creating the particle with position and energy coordinates according to a specified source distribution. Then, the particle travels a certain distance before undergoing an interaction. The type of interaction and the resulting particles are determined by the interaction cross-sections at that point. Any secondary particles created must also be transported and the particle history ends when all particles have either deposited their energy within the medium or have left the geometry.

Using a large set of N individual particles in the Monte Carlo method, the result of a studied magnitude or variable (x) is the average value of all contributions (x_i) of the N simulated events, i.e. it is an approximate solution of such magnitude. Therefore, following the Central Limit Theorem[1] (CLT), for any variable x its estimated value by MC calculation is:

[1]CLT is a theorem in probability theory that states that, given certain conditions, the mean of a large number of independent random variables (each of them with a variance) is approximately normally distributed.

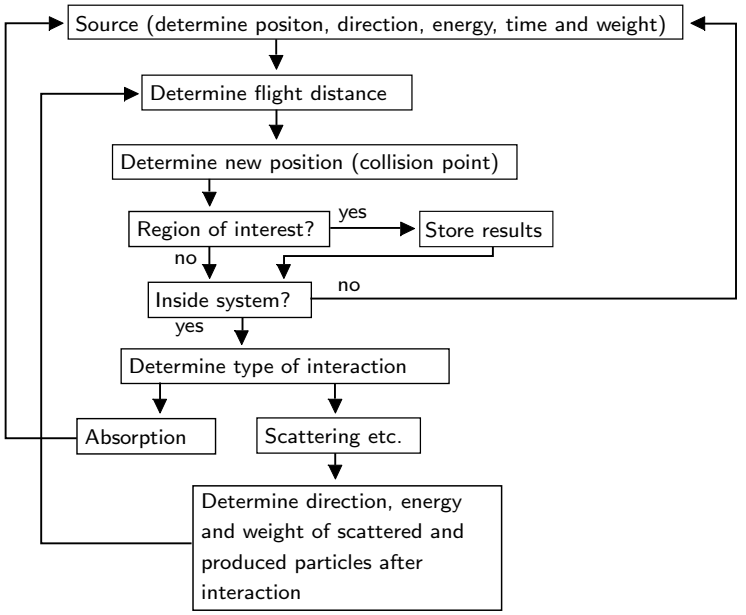

Figure 2.1: Basic flowchart of the Monte Carlo method of radiation transport [2].

$$\bar{x} = \frac{1}{N}\sum_{i=1}^{N} x_i \tag{2.1}$$

with an associated variance $S^2 = \frac{1}{N-1}\sum_{i=1}^{N}(x_i - \bar{x})^2 \approx \bar{x^2} - \bar{x}^2$. The estimated variance for $\bar{x}$ is:

$$S_{\bar{x}}^2 = \frac{1}{N}S^2 \tag{2.2}$$

In the MC code the statistical precision is given in each out-file by means of the relative error:

$$R = \frac{S_{\bar{x}}}{\bar{x}} \tag{2.3}$$

The relative error is proportional to $1/\sqrt{N}$ and it is considered acceptable for values $R < 0.1$. R decreases when the number of events N goes up and therefore, when more time of calculation is employed.

2.2 GEANT4 - A MC simulation toolkit

GEANT4 Monte Carlo toolkit [3] is a well established general purpose Monte Carlo code using Objected-Oriented Technology and C^{++} programming to describe how particles interact with matter. It is the latest incarnation in the GEANT-series of particle transport tools emanating from the high-energy physics community around CERN. GEANT4 was originally developed for the new generation of experiments in high-energy physics to be performed at the Large Hadron Collider (LHC). However, nowadays the code is also widely used in other research fields like medical physics, space astrophysics, radiation protection, dosimetry and radiobiology, etc. The code has been developed and maintained by a worldwide international collaboration of universities, laboratories and institutes including CERN, CIEMAT, IN2P3 and INFN in Europe, KEK in Japan, and SLAC, Fermilab and TRIUMF in North America.

The name Geant4 stands for "GEometry ANd Tracking". The program is able to follow individual particles in an advanced 3-D geometry and to calculate their interaction probabilities with the constituent atoms and nuclei in the geometry medium. Libraries from GEANT4 provide abundant set of physical models to handle the interaction processes over a wide energy range and different particle types. Moreover, the code also includes tools for geometry handling, particle tracking, detector response visualization an user interface. The source code is freely availabe from the website of the project, http://geant4.cern.ch/.

2.2.1 General properties of Geant4

The general term "Monte Carlo method" refers to the solution of a numerical problem using probability statistics and random numbers. In the case of Geant4 this method is used to let different possible particle interactions with different interaction probabilities compete against each other to determine how far a particle can travel in a heterogeneous material before an interaction occurs. Geant4 divides the particle trajectories into series

of steps with certain length λ (the mean-free-path), which represents the average distance that the particle travels before undergoing an interaction. The mean-free-path is calculated according to:

$$\lambda = \frac{1}{\sum \sigma_i(E)N} \tag{2.4}$$

being σ_i the cross section for the physical process that takes place and N the atomic density of the material. To achieve a simulation as real as possible it is necessary to have accurate cross-sections. Geant4 calculates the cross-sections by formulas, parameterisations, or interpolation of databases depending on the particle type, material, and energy. The probability distribution of the traveled distance before interaction (l) is:

$$f(l) = (\sigma_i \cdot N) \cdot e^{-\sigma_i \cdot N \cdot l} \tag{2.5}$$

and the interaction distance l_i is sample for each process as:

$$l_i = -\ln(\xi) \cdot \lambda_i \tag{2.6}$$

being ξ a random number uniformly distributed in the range of (0,1).

To perform the radiation transport, the code selects the process with the smallest interaction distance and execute the step, which entails changes in energy and trajectory. Then the state of the particle is updated and a new step is calculated. This chain is iterated until the particle is absorbed, escapes from the simulation boundaries, or its energy is below than its energy cut-off. Since some types of interactions occur very frequently these are condensed into "continuous" processes. Such processes continuously modify the particle energy, and thus the cross-section, during a step. Therefore a limitation on the step size has to be introduced. The limit has to be small enough for all relevant cross-sections to be approximately constant during the step, but not so small that computation time is greatly increased.

Geant4 is a Toolkit where the user must implement their own software applications by using the tools distributed with the source code.

The user has to develop a GEANT4-based application that must include, at least, three classes: the primary generator action class (*G4VUserPrimaryGeneratorAction*), the detector construction class (*G4VUserDetectorConstruction*) and the physics list class (*G4VUserPhysicsList*) (sections 3.9, 3.10, 3.11 respectively). In addition to these three mandatory classes, the user needs to implement classes to handle and score the physical quantities of interest, such as the particle fluence in the detector, the energy deposition or the energy spectrum. Different facilities to access such physical quantities at different stages of the simulation are provided by the toolkit.

The GEANT4 Monte Carlo toolkit was adopted in this thesis to model the response of the:

- Silicon sensors for neutron detection
- Solid state silicon microdosimeters

2.2.2 Primary Generator Action

The G4VUserPrimaryGeneratorAction class determines the particle source, i.e., create the initial event state or radiation source to be transported. The radiation source has to be modeled as realistic as possible since the simulation results depend strongly on the irradiation configuration. In this work the modelation of the radiation field has been done through the General Particle Source (GPS). GPS is a component provided by GEANT4 which allows complex radiation fields to be modeled with simple pre-defined user interface commands.

A source with different shapes can be defined with the GPS component; including 2D and 3D surfaces such as discs, spheres, or boxes. The angular distribution of particles such as unidirectional, isotropic, cos-law, and beam or arbitrary can also be defined and moreover, the energy of the radiation field can be defined as monochromatic or with an energy spectrum.

2.2.3 Detector Construction

The G4VUserDetectorConstruction class specifies the geometry (shape, size and position) and material composition of all the components present in the simulated set-up. In addition, electromagnetic fields can also be modelled in this class.

The materials are defined as composition of different elements and elements, are defined through their atomic number, mass, and density. Isotopes can also be defined and moreover, it is also possible to attribute to each material a temperature, pressure, and state (solid, liquid or gaseous). It is worth to mention that even though technically any material can be defined in GEANT4, the user has to ensure that both cross-section data and physics models are updated, and with a correct performance, for the simulated elements at the energy range of interest. The composition of materials used in the simulation projects of this thesis were derived from the NIST Atomic Weights and Isotopic Compositions database [4].

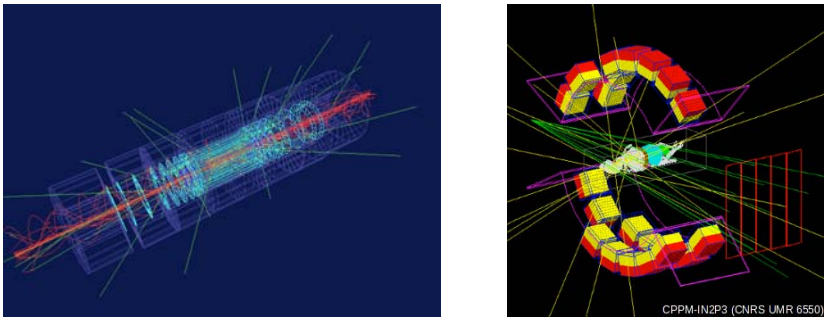

Figure 2.2: Examples of GEANT4 simulations architectures - (a) Sketch of the ATLAS inner detector and (b) phantom in a PET prototype detector. Images from [5].

Figure 2.2 shows two examples of GEANT4 constructions defined in the G4VUserDetectorConstruction class. The code allows the modeling of both large and sub-micrometre scale geometries such as the ATLAS detector of the LHC or a DNA helix [6] respectively.

2.2.4 Physics List

The G4VUserPhysicsList assigns physical *processes* and *models* to the particles as well as the associated cross sections. In GEANT4 a process is a class which describes how and when a specific kind of physical interaction takes place along a particle track and a model is another class whose methods implement the details of the interaction. A detailed description of the available physical models is given in the GEANT4 Physics Reference Manual [7].

GEANT4 lets the user to establish a clear and customizable correspondence between particles types and processes and also, offers a choice of models and cross sections to implement to each process. A set of models for a given process can be chosen with great flexibility invoking the appropriate one depending on the particle type, energy range and other characteristics[1]. Therefore, a given particle typically has several processes assigned to it and several models assigned to each process. As the configuration of the G4VUserPhysicsList class is often a difficult task, the GEANT4 collaboration provides predefined physics lists suitable for specific simulations purposes.

The GEANT4 collaboration used three different methods to obtain all models available in the toolkit. Models can be: i) Data driven: phenomenological, inspired by theory; ii) Parameterized: using data and physical meaningful extrapolation, depend mostly on fits to data and some theoretical distributions; and iii) Theory driven: fully data driven approach, based on phenomenological theory models.

Four main categories of physical processes are provided by GEANT4 [8]: electromagnetic (EM), Hadronic, Decay and Parameterized[2] and Trans-

[1] GEANT4 describes physical interactions with complementary and alternative physics models in an energy range that could span more than 15 orders of magnitude (from thermal for neutron interactions to high energy for cosmic rays physics). Therefore, depending on the the setup simulated, the full range or only a small part might be needed in a single application.

[2] Decay includes weak and electromagnetic decays processes while Parameterized is a fast simulation functionality which provides hook to the user to shortcut the detailed

portation.Electromagnetic, hadronic and transportation apply for the simulations developed along this work and therefore, are briefly summarized as follows:

2.2.4.1 Electromagnetic processes

These processes manage the electromagnetic interactions of leptons, photons, hadrons and ions. The electromagnetic package includes the processes of: ionisation, bremsstrahlung, multiple scattering, Compton and Rayleigh scattering, photo-electric effect, pair conversion, annihilation, synchrotron and transition radiation, scintillation, refraction, reflection, absorption and Cherenkov effect and it is organized as a set of five class categories [3]:

- standard: handling basic processes for electron, positron, photon and hadron interactions;
- low energy: providing alternative models extended down to lower energies than the standard category. A more precise description description at low energy with more atomic shell structure detail is obtained;
- muons: handling muon interactions;
- X-rays: providing specific code for X-ray physics;
- optical: providing specific code for optical photons;

The standard electromagnetic processes are commonly used for high energy physics experiments and cannot be expected to simulate details below 1 keV. For the purpose of this thesis, low energy studies are required so the low energy processes category was used. This category is designed for applications which require higher accuracy for electrons, hadrons and ion tracking without magnetic field. It adopts a more complex design

tracking

approach covering processes for electrons, photons, positive and negative charged hadrons and positive ions mainly in the keV − MeV range. In the particular case of hadrons and ions, the low energy process that handles the ionization adopts different models depending on the energy range and the particle charge [7].

With electromagnetic physics, a production cut for secondary gamma, electron, positron and proton[1] must be defined. The cuts are specified as range cuts, which are converted at initialision time into energy thresholds. If the range of the secondary gamma, electron, positron or proton is larger than the cut, it is generated and tracked, otherwise there is no generation and their energy is considered to be deposited locally. In the simulations of this thesis, the cut was defined to achieve fast simulation execution speed without sacrificing the accuracy of the results.

2.2.4.2 Hadronic processes

Hadronic processes manage the elastic, fission, capture and inelastic processes of hadron and ion interactions with atomic nuclei[2]. Hadronic interactions are handled by different models which cover the high, intermediate and low energy domains (see Figure 2.3). String models are used for high energy interactions (from ≈10 GeV to 50 TeV); intra-nuclear cascade models for intermediate energies (≈10 MeV to 10 GeVs) and the pre-compound model for low energies (from 0 to 170 MeV). The description of each model as well as its interaction details can be found in the Physics Reference Manual [7] provided by the GEANT4 collaboration.

Geant4 also provides a high-precision data-driven model of low-energy neutron interactions from thermal kinetic energies up to about 20 MeV. Radiative capture, elastic scattering, fission and inelastic scattering are considered according to cross section from Evaluated Nuclear Data File (ENDF/B-VII) [9] library. In case information on a specific element is not

[1] The cut for proton is applied by elastic scattering processes to all recoil ions.

[2] These four processes are known as pure hadronic but radioactive decay and gamma-lepto-nuclear processes are also included in this category

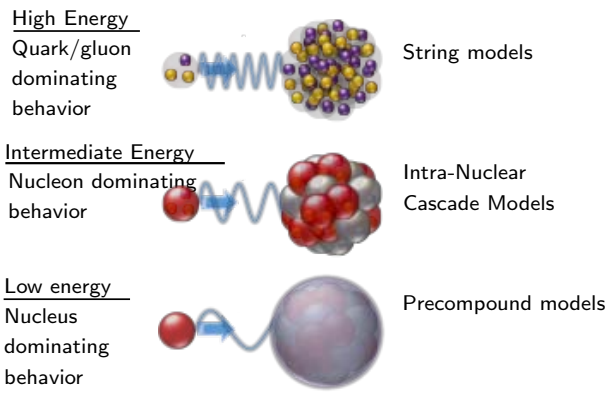

Figure 2.3: Energy domain representations for hadronic interactions - On the right the main models used by GEANT4 to describe that interaction details.

available, parameterized models [7] are used instead of the high-precision models. All simulations of chapter 3 have been performed with this high precision neutron package.

Details of the hadronic models implemented in the simulation of the solid state silicon microdosimeters are explained in the section 4.4.

2.2.4.3 Transportation process

The transportation process is responsible for determining the geometrical limits of a step. It calculates the length of step with which a track will cross into another volume. When the track actually arrives at a boundary, the transportation process locates the next volume that it enters. If the particle is charged and there is an electromagnetic (or potentially other) field, it is responsible for propagating the particle in this field. It does this according to an equation of motion. This equation can be provided by GEANT4, for the case a magnetic or EM field, or can be provided by the user for other fields.

Bibliography

[1] N Metropolis and S Ulam. **The Monte Carlo method.** *Journal of the American Statistical Association*, **44**(247):335–341, 1949. 23

[2] H Hirayama and Y Namito. **Lecture Notes of Radiation Transport Calculation by Monte Carlo Method**. *KEK Internal 2000-20*, (March), 2001. 25

[3] S Agostinelli, J Allison, and K Amako. **Geant4-a simulation toolkit**. *Nuclear Instruments and Methods in Physics Research A*, **506**:250–303, 2003. 26, 31

[4] **NIST. Physical reference data website**. 29

[5] Gunter Folger. **Geant4 Applications**, 2013. 29

[6] S. Incerti, G. Baldacchino, M. Bernal, R. Capra, C. Champion, Z. Francis, P. Guèye, A. Mantero, B. Mascialino, P. Moretto, P. Nieminen, C. Villagrasa, and C. Zacharatou. **The Geant4-DNA Project**. *International Journal of Modeling, Simulation, and Scientific Computing*, **01**(02):157–178, 2010. 29

[7] **Physics Reference Manual**. **2**(December), 2015. 30, 32, 33

[8] Geant Collaboration. **Geant4 User ' s Guide for Application Developers**. (December), 2014. 30

[9] **ENDF. Evaluated Nuclear Data File (ENDF)**. 32

Part II

Neutron Detection

3

Silicon sensors for neutron detection

Neutrons are generally detected in silicon detectors through nuclear reactions that result in the production of energetic charged particles such as protons, tritiums and alpha particles. Virtually every type of semiconductor silicon neutron detector involves the combination of a target material, known as the converter material and responsible to carry out this conversion, together with one of the conventional silicon charged particle radiation detectors.

We limit our discussion in this thesis to those methods that are intended to indicate only the detection of a neutron, with no attempt made

to measure its kinetic energy. Devices that can measure slow neutron energies such as crystal spectrometers or mechanical monochromators are generally complex research-oriented instrumentation systems and are not covered here.

3.1 Neutron classification

Neutrons are frequently classified by their kinetic energy as shown in Table 3.1[1]. Although, in somewhat of an oversimplification, we will divide neutrons into two categories on the basis of their energy, either *slow neutrons* or *fast neutrons*, and discuss their interaction properties separately (sections 3.2.1 and 3.2.2). The dividing line of these two categories will be at about 0.5 eV, the so called *cadmium cut off energy*, where the neutron absorption cross section in cadmium suffers and abrupt drop.

Table 3.1: Classification of free neutrons according to kinetic energies.

Neutron Type	Kinetic Energy Range
UltraCold	$< 2 \cdot 10^{-7}$ eV
Very cold	$2 \cdot 10^{-7}$ eV - $5 \cdot 10^{-5}$ eV
Cold	$5 \cdot 10^{-5}$ eV 0.025 eV
Thermal	$\approx$ 0.025 eV
Epithermal	1 eV - 1 keV
Intermediate	1 keV - 0.1 MeV
Fast	>0.1 MeV

For neutrons with energies below 1 eV a thermal equilibrium with their surroundings can be reached and then, their energy is distributed according to the Maxwell-Boltzmann formula:

$$f(E) = \frac{2\pi}{(\pi k_B T)^{3/2}}\, e^{-E/k_B T} E^{1/2} \tag{3.1}$$

[1]The terminology and energy ranges may vary for different references.

where $f(E)$ is the probability, per unit energy, of finding the particle with an energy E, k_B is the Boltzmann constant (k_B =8.61x10^{-5}eV/K) and T is the temperature of the medium.

The most probable energy value is k_BT while the average energy is $\langle E \rangle = 3/2k_BT$. For neutrons at room temperature (293 K) the most probable value is 0.025 eV which is equivalent to a velocity of 2200 m/s.

3.2 Neutron detection methods

Many neutron detection systems exist today and depending on the time needed to provide a response they can be classified in two general types: passive and active detectors.

Passive detectors need to be read at a later stage in order to ascertain the level of exposure recorded. The signal consists of detector changes of diverse nature such as electrical, mechanical, optical or chemical. Examples of passive detectors are radiographic films, neutron activation foils and thermoluminescent dosimeters (TLDs). On the other hand, active detectors give the response to the radiation immediately[1], usually by means of electric current or current pulses. The category of active detectors comprises gaseous and semiconductor detectors, which are based on ionization, and scintillator detectors, based on excitation. In this chapter we will focus on active neutron detectors.

There are different detection methods as a function of the energetic range of study since the interaction cross section of neutrons is strongly dependent on their energy. If neutrons have low energy, they can undergo non-radiative processes and be detected through the secondary charged particles emitted and, on the other hand, if neutrons have high energy they

[1]The time required to fully collect the charge varies greatly from one detector to another. For example, in ion chambers the collection time can be as long as a few milliseconds, whereas in semiconductor diode detectors the time is a few nanoseconds. These times reflect both the mobility of the charge carriers within the detector active volume and the average distance that must be traveled before arrival at the collection electrodes.

can suffer elastic scattering and be detected through the recoil nucleus. Methods of slow and fast neutron detection are explained as follows.

3.2.1 Slow neutron detection

Because of the small kinetic energy of slow neutrons, very little energy can be transferred to the nucleus in elastic scattering. Consequently, this is not an interaction on which detectors of slow neutrons can be based, but these interactions bring the slow neutrons into thermal equilibrium with the medium. Once neutrons have been thermalized, they can undergo an absorption process and be indirectly detected through the ionization produced by the reactions products of the reaction.

The main isotopes used for slow neutron detection together with the absorption reaction they undergo and their thermal neutron cross-sections (σ_n) are listed in Table 3.2 and briefly discussed in the following paragraphs.

Table 3.2: Absorption reactions of common neutron converters.

Absorption reaction	σ_n **(barn)**
${}^{3}_{2}\mathrm{He} + {}^{1}_{0}\mathrm{n} \rightarrow {}^{3}_{1}\mathrm{H}\ (0.191\,\mathrm{MeV}) + {}^{1}_{1}\mathrm{p}\ (0.574\,\mathrm{MeV})$	5330
${}^{10}_{5}\mathrm{B} + {}^{1}_{0}\mathrm{n} \rightarrow {}^{4}_{2}\mathrm{He}\ (1.47\,\mathrm{MeV}) + {}^{7}_{3}\mathrm{Li}\ (0.84\,\mathrm{MeV}) + \gamma\ (0.48\,\mathrm{MeV})$ ${}^{10}_{5}\mathrm{B} + {}^{1}_{0}\mathrm{n} \rightarrow {}^{4}_{2}\mathrm{He}\ (1.78\,\mathrm{MeV}) + {}^{7}_{3}\mathrm{Li}\ (1.01\,\mathrm{MeV})$	3840
${}^{6}_{3}\mathrm{Li} + {}^{1}_{0}\mathrm{n} \rightarrow {}^{3}\mathrm{H}\ (2.73\,\mathrm{MeV}) + {}^{4}_{2}\mathrm{He}\ (2.05\,\mathrm{MeV})$	940
${}^{155}_{64}\mathrm{Gd} + {}^{1}_{0}\mathrm{n} \rightarrow {}^{156}_{64}\mathrm{Gd} + \gamma\ (0.09{,}0.20{,}0.30\,\mathrm{MeV}) + \mathrm{e}^{-}$	60791
${}^{157}_{64}\mathrm{Gd} + {}^{1}_{0}\mathrm{n} \rightarrow {}^{158}_{64}\mathrm{Gd} + \gamma\ (0.08{,}0.18{,}0.28\,\mathrm{MeV}) + \mathrm{e}^{-}$	255011

3.2.1.1 The ^{3}He(n,p)^{3}H reaction

Helium-3 is an isotope widely used for neutron detection in gaseous detectors. When a thermal neutron interacts with a ^{3}He nucleus, that nucleus may capture the incident neutron and eject a proton and a tritium ac-

cording to the next reaction:

$$^{3}_{2}He +^{1}_{0} n \rightarrow^{3}_{1} H +^{1}_{1} p \tag{3.2}$$

The microscopic thermal neutron cross section for this reaction is 5330 b, significantly higher than that for the boron reaction (see Table 3.2). The total cross section decreases with increasing neutron energy, with a dependence proportional to the inverse of the neutron velocity over much of the energy range (Figure 1.6).

Since the incoming neutron kinetic momentum is very small (E=0.025 eV for thermal neutrons), the reaction products must also show a net momentum of essentially zero. As a consequence, both reaction products are ejected in opposite directions and the overall energy of the reaction is distributed between them by the conservation of energy and momentum principles as follows (in the center-of-mass frame):

$$E_H + E_p = Q = 0.764 \text{ MeV} \tag{3.3}$$

$$m_H + v_H = m_p + m_p \tag{3.4}$$

whose simultaneous solution gives: E_H =0.191 MeV and E_p =0.573 MeV.

Due to its gaseous nature, ^{3}He is only used in gas detectors but in this work only solid form of neutron reactive materials will be considered as converters to be used in silicon neutron detectors.

3.2.1.2 The ^{10}B(n,α)^{7}Li reaction

The ^{10}B(n,α)^{7}Li reaction leads to the following reaction products:

$$^{10}_{5}B +^{1}_{0} n \rightarrow \begin{cases} ^{4}_{2}\alpha(1.777\,\text{MeV}) +^{7}_{3} Li(1.015\,\text{MeV}) & Q = 2.792\,\text{MeV} \\ ^{4}_{2}\alpha(1.470\,\text{MeV}) +^{7}_{3} Li^{*}(0.840\,\text{MeV}) & Q = 2.310\,\text{MeV} \end{cases} \tag{3.5}$$

where the values in parenthesis are the reaction product energies for negligible incoming neutron energy.

The alpha and triton particles produced in the reaction must be oppositely directed when the incoming neutron energy is low. After absorption,

94% of the reactions leave the ^{7}Li ion in its first excited state, which rapidly de-excites to the ground state ($\approx 10^{-13}$s) by releasing a 480 keV gamma-ray. The remaining 6% of the reactions result in the ^7Li ion dropping directly to its ground state.

The microscopic thermal neutron cross section for this reaction is 3840 b and the total cross section falls off, as in the case of ^{3}He, with a 1/v or 1/E energy dependence (Figure 1.6).

3.2.1.3 The ^{6}Li(n,α)^{3}H reaction

The ^{6}Li(n,α)^{3}H reaction leads to the following products:

$$^6_3Li +^1_0 n \rightarrow^3_1 H(2.73\,\mathrm{MeV}) +^4_2 \alpha(2.05\,\mathrm{MeV}) \quad Q = 4.78\,\mathrm{MeV} \tag{3.6}$$

where the reaction products are again oppositely directed if the neutron energy is sufficiently small.

The microscopic thermal neutron absorption cross section for this reaction is 940 barns for ^{6}Li and the total neutron cross section also shows a (1/v) dependence, except at a salient resonance above 100 keV, in which the absorption cross section surpasses that of ^{10}B for energies between approximately 150 keV to 300 keV (Figure 1.6).

Pure ^{6}Li is not widely used as neutron converter material because it is corrosive and its reactive nature results in cumbersome handling procedures but the stable compound of ^{6}LiF is one popular form of using this isotope.

The ^{10}B(n,α)^{7}Li reaction leads to a generally higher reaction probability than the ^{6}Li(n,α)^{3}H reaction for neutron energies below 100 keV, however the higher energy reaction products emitted from the ^{6}Li(n,α)^{3}H leads to greater ease of detection.

3.2.1.4 The Gd neutron absorption reaction

The gadolinium neutron absorption results in an assortment of prompt reaction products that include low energy gamma-rays and beta particles

at energies ranging up to 280 keV (the most significant is a 72 keV beta particle that is emitted in 39% of the capture reactions [1]).

Gadolinium coated devices are attractive due to the large microscopic thermal neutron absorption cross sections of ^{155}Gd and ^{157}Gd isotopes (58 000 b and 240 000 b respectively). Purified ^{157}Gd is too expensive to be used as a practical coating for semiconductor detectors, however natural Gd (14.7% of ^{155}Gd and 15.7% of ^{157}Gd) has still a thermal neutron cross section of 46 000 b and it is not cost prohibitive.

Despite the high value of thermal neutron cross section, a fundamental drawback of gadolinium is that the particle range of the conversion electrons is limited to only a few microns in the gadolinium material and the signal produced in the semiconductor is difficult to distinguish from gamma ray background and electronic noise. Because of that this material has no clear advantage over ^{10}B- or ^{6}LiF-coated devices and it will not be studied in this work.

3.2.2 Fast neutron detection

The previously described slow neutron detection methods can be also applied to detect fast neutrons, however the efficiency of these methods is limited because the reaction probability decreases rapidly with increasing neutron energy.

The more commonly fast neutron detection methods are based either on using neutron moderation or using the recoil nuclei coming from an elastic scattering process. In neutron moderation, neutrons are slowed down via elastic and inelastic scattering with a suitable material and then, some slow neutron detection method is applied. In the second case, if the incoming neutron is in the keV range or higher, the recoil nuclei from an scattering event can generate a usable detector signal and be detected directly.

The elastic cross section for fast neutrons is large in several materials, specially in hydrogen, which is the most popular target nucleus used for neutron detection. Also, due to the fact that the fraction of energy trans-

ferred in the neutron-nucleus collision increases as the mass of the recoil nucleus decreases, hydrogen and hydrogen-rich materials such as polyethylene, paraffin, water, etc, are preferred to deliver recoil protons through the (n,p) elastic reaction. Moreover, observing recoil nuclei with the time-of-flight method [2] enables neutron energy measurements by assessing their velocities.

3.3 State of the art in active neutron detectors

Since there is not a perfect detector for all application fields, the main properties of active radiation detectors have to be considered to select the most suited in each case. These main properties are the following:

- Absolute efficiency: ratio between the measured number of counts recorded by the detector and the total number of emissions from the radiation source. The absolute efficiency is dependent on the experimental setup (primarily the distance from the source to the detector and the detector geometry).

- Intrinsic efficiency: absolute efficiency multiplied by $(4\pi/\Omega)$, where Ω is the solid angle of the detector seen from the actual source position[1]. It is much more convenient to tabulate values of intrinsic rather than absolute efficiencies because the geometric dependence is much milder. However a slight dependence on distance between the source and the detector does remain in intrinsic efficiency because the average path length of the radiation through the detector will change somewhat with this spacing.

- Energy resolution: defined as the accuracy with which the system can measure the energy of a radiation and its ability to distinguish radiations of slightly different energies.

[1] From now on, if it is not specified in the text, efficiencies will be intrinsic efficiencies

- Linearity: a detector is lineal if there is a linear relationship between the energy of the detected radiation and the response of the detector.
- Dead time: minimum amount of time that should separate two events in order to count each one individually. The dead time of the detector may be set by physical processes taking place in the detector itself or by the associated electronics.
- Sensitivity: ability to produce a valid detector signal. It depends on the interaction cross section with the detector material, on the detector mass, on the detector noise and on the material around the detector.

In the particular case of the neutron detectors, there are two other criteria: the gamma rejection and the neutron/gamma-ray discrimination. These are important parameters since most of the environments where neutron detectors operate are composed by neutron and gamma radiation.

- Gamma rejection: detector response in the presence of a gamma-ray source.
- Neutron/gamma-ray discrimination: ability to distinguish between gamma and neutron radiation events in neutron detectors. Gamma-rays may interact with the detector and create secondary electrons that can produce ionization and create a false count in the detector.

As previously mentioned, the three main types of active neutron detectors are: gaseous detectors, scintillators and semiconductor detectors. Each of them is briefly reviewed in as follows. This section is based on the information from [3], [4] and [5], as well as general information from [6].

3.3.1 Gaseous detectors

A gaseous detector consists of a volume of gas between two electrodes, with an electrical potential difference applied between the electrodes. Ionizing

radiation loses energy in the gas by creating excited molecules and/or generating electron-ion pairs. A simple sketch of a gaseous detector is shown in Figure 3.1.

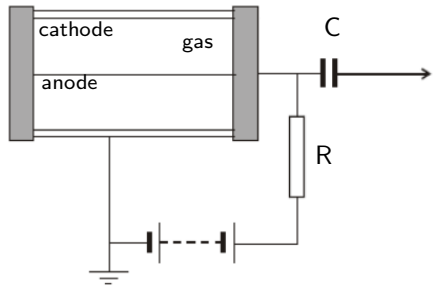

Figure 3.1: Diagram of the simple circuit for a gas-filled detector - Operating in pulse mode.

The measured charge or current in a gaseous detector is proportional to the applied voltage and the detector sensitivity depends on the volume and pressure of the gas and on the associated electronic readout components. Depending on the operating voltage applied between the electrodes, different regions of detector operation can be distinguished. These different regions are depicted in Figure 3.2 and are briefly explained as follows:

- Ion Chamber region: in this region only discrete charges created by each interaction between the charged particle and the gas are used. The applied voltage is sufficiently high so that only a negligible amount of recombination occurs. Detectors operating in this region are called ionization chambers.

- Proportional counting region: rely on the phenomenon of gas multiplication to amplify the charge represented by the original ion pairs created within the gas. The collected charge is linearly proportional to the energy deposited. This region is used in situations which the number of ions pairs generated by the radiation is too small to permit

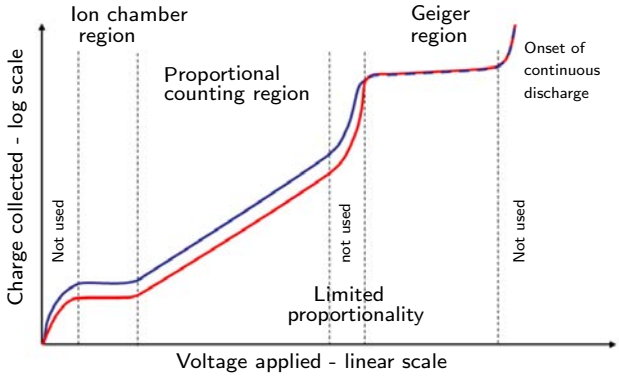

Figure 3.2: The different regions of operation of gas-filled detectors - The observed pulse amplitude is plotted for events depositing two different amounts of energy within the gas.

satisfactory operation as ionization chambers. Detectors operating in this region are called proportional counters.

- Geiger-Mueller region: in this region all pulses are of the same amplitude regardless of the number of original ion pairs that initiated the process. Therefore, Geiger counters can function only as a simple counters of radiation-induced events and cannot be applied in direct radiation spectroscopy because all information on the amount of energy deposited by the incident radiation is lost. Neutron detectors in Geiger-Mueller region are not used because its not possible to discriminate neutron signals from gamma rays signals.

There are four main types of gaseous detectors used for neutron detection: the ^{3}He-filled gas proportional counters, the boron trifluoride (BF^3) proportional tubes, the boron-lined proportional counters and the fission counters. These detectors rely on the high cross section for thermal neutrons but, as already mentioned, fast neutrons can also be detected if devices are surrounded by a suitable hydrogen-rich material.

3.3.1.1 ^{3}He-filled gas proportional counters

The proportional counters filled with helium-3 are the 'gold standard' thermal neutron detectors since ^{3}He has a large capture cross section and a very low sensitivity to γ-ray interference (high γ-ray rejection). ^{3}He tubes usually operated in the range of 1200 to 1800 volts and achieve intrinsic efficiencies up to 77%.

In some gaseous detectors, other gases are often added to improve the detector performance. For example, in ^{3}He devices the addition of a heavy gas, such as argon, reduces the proton range and guarantees total energy deposition in the cavity. Moreover, argon also speeds up the charge collection time but with the adverse effect of increasing the gamma-ray sensitivity [6]. In table 3.3 the efficiencies of two ^{3}He-filled gas proportional counters are shown.

One of the main issues of the the ^{3}He-filled gas detectors is that within the last few years, the amount of ^{3}He available for use in gas neutron detectors has become more restricted, while the demand has significantly increased, especially for homeland security applications after the attack of September 11, 2001. This restriction is due to the fact that the ^{3}He reserves are foreseen to be consumed in the coming decades[1] and besides, no significant amount of new tritium is being produced anywhere in the world (^{3}He is a byproduct form the beta decay of tritium ($t_{1/2} = 12.3$ years), and it is separated as a part of the tritium purification process [8]). Therefore, other alternative technologies need to be investigated. Nowadays one of the replacement technology options for ^{3}He-filled tubes are the boron-lined proportional counters.

3.3.1.2 Boron Trifluoride filled proportional tubes

The BF_3 counters are a direct physical replacement for ^{3}He-filled gas proportional counters and they were widely used as neutron detectors before helium-3 became a commonly used conversion material. The gas is com-

[1] Although hopes are focused in newly discovered deposits in Tanzania [7]

posed of fluoride atoms and boron atoms (B atoms enriched in boron-10).

BF_3 tubes have equivalent gamma-ray rejection as ^{3}He tubes but lower thermal neutron detection efficiency because of the lower cross section of ^{10}B, BF_3 tubes are about 30 to 50% as efficient at detecting neutrons as helium-3 tubes.

The main drawback of these tubes is that safety-related limitations have to be taken into account due to the hazardous nature of BF_3 gas, which is toxic. The operation voltages of the (BF_3) detectors are between 1500 and 3000 V.

3.3.1.3 Boron-lined proportional counters

Boron lined proportional counters are sensitive to neutrons in the same way as BF_3 proportional counters but incorporate the boron as a solid coating on the walls of the detector rather than in gaseous form.

The detection efficiency is about 10 to 15% that of a helium-3 tube. The efficiency of boron-lined proportional counters is also lower than BF_3 gas-filled counters, however higher gamma-ray rejection is achieved. This is due to the lower fill pressure and lower operating voltage used in boron-lined counters, which reduce the size of gamma-ray pulses relative to neutron pulses.

These devices operated at a voltage of 600 to 850 V and are typically used where circumstances, e.g. high operating temperatures, prevent the use of BF_3 as the neutron detecting medium and where it is necessary to detect neutrons in the presence of high gamma-ray fields.

3.3.1.4 Fission counters

The most popular form of fission detector is an ionization chamber because the ionization caused by the fission fragments is sufficient to create signal and no further charge multiplication within the detector is necessary. They detect neutrons that induce fissions in fissionable material coated on the inner walls of the chamber. The fissionable material is usually

uranium highly enriched in ^{235}U. The fission chamber uses only a small quantity of fissionable material and has a low detection efficiency. For thermal neutrons, the intrinsic efficiency is typically between 0.5% - 1 % and the applied voltage is in the range of 200 to 600 V. Fission chambers typical operate in pulse mode for nonreactor applications but they can also function in current mode in applications like reactor neutron flux monitors.

3.3.2 Scintillators

Scintillator materials operate by absorbing incident radiation that raises electrons to excited states. After the subsequent de-excitation, which usually takes from nanoseconds to tens of nanoseconds, the scintillator emits a photon in the visible light range. An scintillation detector is obtained when a scintillator material is coupled to an electronic light sensor such as photomultiplier tube (PMT), photodiode, or silicon photomultiplier. The electronic sensor absorbs the light emitted by the scintillator and re-emits it in the form of electrons via the photoelectric effect. The subsequent multiplication of those electrons (sometimes called photo-electrons) results in an electrical pulse which holds information about the initial incident particle. Figure 3.3 illustrates the working principle of an scintillator detector.

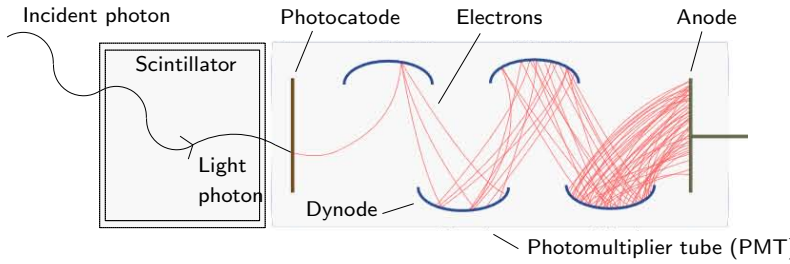

Figure 3.3: Schematic diagram of a scintillation detector - Sketch of a scintillation material (left) coupled to a photomultiplier tube (right).

As already known, thermal neutrons do not produce ionization directly in the scintillator material, but they can be detected with loaded

scintillators (plastic or liquid scintillator which has been loaded with an element in order to alter its properties). Loaded scintillators containing elements with high thermal neutron cross section like boron or lithium are suitable for the detection of thermal neutrons. One of the most used loaded scintillator detector for neutron detection is the highly enriched ^{6}Li(Eu) crystal, where it is possible to have enrichment up to 96% of ^{6}Li. These detectors exhibit a thermal neutron detection efficiency of about 50% and low gamma ray sensitivities comparable to ^{3}He. Boron-loaded plastic scintillators have been also investigated but they are much less effective at discrimination against gamma-ray backgrounds than BF_3 proportional tubes.

Like in gaseous detectors, fast neutrons can also be detected by surrounding the scintillator with a suitable material that moderates the neutrons. Another possibility for fast neutron detection is using an organic scintillators (plastic or liquid) that contains a large concentration of hydrogen atoms. By means of elastic scattering the energy of the neutrons can be partially transferred to the protons which on their turn can produce scintillation light.

The following table (Table 3.3) summarizes the main characteristics of both gaseous and scintillators thermal neutron detectors cited above:

Table 3.3: Typical values of efficiency and gamma-ray sensitivity for some common neutron detectors - The efficiency values depict the interaction probability for neutrons hitting the detector face at right angles and the gamma-ray sensitivity is an approximate upper limit of gamma-ray dose that can be present with detector still providing usable neutron output signals. Table obtained from [6].

Detector type	Neutron active material	σ (b)	Efficiency (%)	Gamma-ray sensitivity (mSv/hour)
^{3}He (4 atm), Ar (2 atm)	^{3}He	5330	77	10
^{3}He (4 atm), CO_2	^{3}He	5330	77	10^2
BF_3 (0.66 atm)	^{10}B	3840	29	10^2
BF_3 (1.18 atm)	^{10}B	3840	46	10^2
^{10}B-lined chamber	^{10}B	3840	10	10^4
Loaded scintillator	^{6}Li	940	50	10
Fission chamber	^{235}U	680	0.5	10^7

3.3.3 Semiconductor neutron detectors

The interest in neutron detection with semiconductor sensors has increased in recent years. This has been prompted, on the one hand, by the need to replace the ^{3}He tube detectors because of the exhaustion of helium reserves and on the other hand, there are several environments which require features that only the semiconductor devices possess, such as low weight, low size, compactness, robustness and low battery consumption for transportability, as well as a fast response and insensibility to electromagnetic fields [3].

Two subclasses of semiconductor neutron detectors are defined: direct- and indirect- conversion semiconductors (Figure 3.4). In direct conversion the semiconductor material is neutron sensitive, like CdTe and GaAs materials, while in indirect-conversion the semiconductor is coupled with a converter material material that strongly absorbs neutrons. Within the

indirect-conversion subclass, two main configurations can also be distinguished: the 2D or planar configuration and the 3D or microstructured configuration.

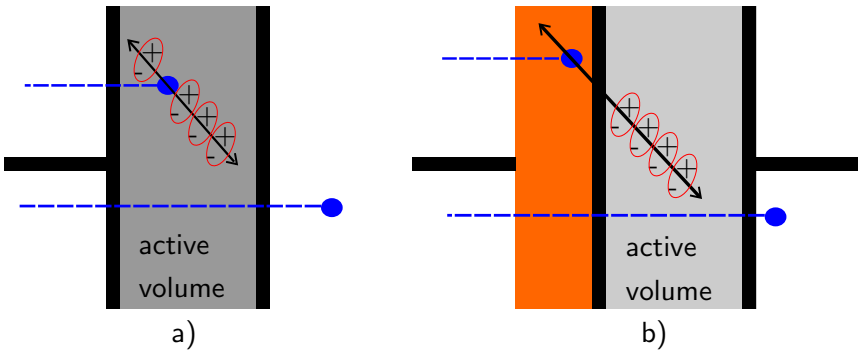

Figure 3.4: Representation of neutron absorption from direct- and indirect-conversion semiconductor neutron detectors - (a) Direct-conversion and (b) indirect conversion. In the figure, the thermal neutrons are represented as blue trajectories and the $e^{-}h^{+}$ pairs responsible of creating the detector signal are also depicted in each case.

For direct-conversion geometries the neutron sensitive material and space charge layer are the same, so all the energy of charged reaction products is available for e^{-}-h^{+} pairs creation.

Direct-conversion geometries are the most straightforward to construct and are potentially capable of the highest total efficiencies, however they have a lot of limitations: they are usually very thick bulks which need high voltage bias (300 -1000 V) and, what is more important, the charge carrier transport properties of these materials are very bad and there is trapping, which severely limits the detector signal. Consequently, the collected charge is very low, with the risk of being confused with the noise level. In order to discriminate signal from noise, it is necessary to increase threshold levels and then, the detection efficiency is dramatically reduced.

For indirect-conversion geometries the semiconductor is coated (or filled) with the converter material to make the arrangement a semiconductor neutron detector. Several converter requirements must be considered

to achieve a good detecting efficiency:

- The cross-section for non-radiative capture interactions is in the energetic range of interest.
- The converter should be made up of elements with high isotopic abundance of those isotopes which capture neutrons.
- The energy of the reaction, Q, should be high enough to allow a simple pulse height discrimination of gamma-rays, which are usually present in neutron fields.
- The products of the neutron interaction must have range of flight in the converter material long enough to reach the sensitive volume of the detector and create a sufficient signal there.

In 1959, R. V. Babcock group was the first one to apply a neutron absorbing material to a diode semiconductor [9]. They used the basic planar configuration, where only one semiconductor side is covered by the converter layer. This configuration has been also studied by several groups [10, 11, 12, 13, 14, 15] concluding that the maximum detection efficiency cannot exceed 5% for ^{10}B and ^{6}LiF converter materials due to geometrical restrictions of the planar configuration[1]. Both natural Gadolinium and Gadolinium-157 were also studied due to their high thermal neutron cross section but their expensive commercial price and the low energy of the reactions products makes them not valid for achieving high thermal neutron efficiency with the basic planar configuration [16].

The main limitation of the 2D or planar configuration is that suffers from self-absorption effects which ultimately limit neutron detection efficiency [16]. The probability of the neutron interaction increases with the thickness of the converter layer, but at the same time this reduces the probability that the reaction products reach the sensitive volume of

[1]Detectors coated with pure ^{6}Li metal can achieve 11% [16] but the reactivity of Li metal complicates fabrication

the semiconductor due to energy loss within the converter itself. Other configurations of planar semiconductor-based neutron detectors (Figure 3.5) have been studied and several straightforward methods to increase the thermal neutron detection efficiency were proposed [16, 17]. Stacking individual devices can increase the overall system neutron detection efficiency, although the increase in efficiency does not accumulate linearly. The initial neutron flux will be attenuated by each of the neutron absorbing layers. As a result, the neutron flux decreases for each subsequent detector and the effect must be taken into account when calculating the overall neutron detection efficiency of the stack.

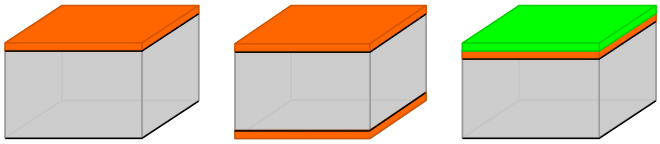

Figure 3.5: Different configurations of 2D or planar designs.

The other possible configuration for semiconductor neutron detectors is the so called 3D or microstructured design (Figure 3.6). In the late 80's Muminov, in a theoretical study, suggested that the incorporation of channels in a semiconductor substrate subsequently backfilled with a neutron reactive material might increase the thermal neutron detection efficiency [18]. The 3D design overcomes the geometric constraints that limit the efficiency in planar configurations by providing an extended surface area between the converter and the semiconductor and by increasing the probability that reaction products escape into the semiconductor.

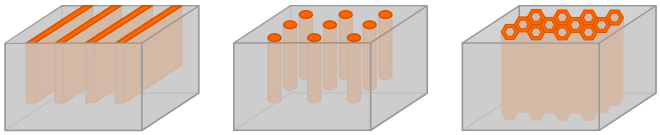

Figure 3.6: Some configurations of 3D or microstructured desings.

The first operational device to prove this concept was fabricated by

D.S. McGregor's group [19] and since then several research groups have worked on different kind of patterns etched deeply into the substrate and filled with different neutron reactive materials [20, 21, 22, 23, 24]. Optimized microstructured designs theoretically predicted to reach 70% thermal neutron detection efficiency for aggressive structures [25, 26] unfortunately, achieving high aspect ratio etching and conformal converter material deposition have proven to be challenges that have limited detector efficiencies to ≈45% [26, 27].

A maximum thermal neutron detection efficiency of 48% was achieved by Q.Shao et. al. [28] using silicon pillars surrounded by ^{10}B while McGregor et al.[29] reported an efficiency of 25% for an individual device filled with ^{6}LiF powder. An efficiency of 42% was also reported by McGregor et al. [30] with a double stacked single devices.

The Radiation Detectors Group at IMB-CNM has produced at the clean room facilities two different silicon designs to detect neutrons; the ultra-thin 3D sensor and the microstructured sensor, which are covered and filled respectively with a converter material. Moreover, a novel semiconductor imaging detector to obtain images with thermal neutrons was also manufactured. These sensors are explained in the following sections.

3.4 Ultra-thin 3D silicon sensors

The ultra-thin 3D sensors (U3DTHIN) fabricated at IMB-CNM are PIN diodes fabricated on silicon-on-insulator (SOI) wafers (Figure 3.7(a)). These wafers have an active thickness of 10 µm or 20 µm and a 1 µm buried silicon oxide layer over a 300 µm-thick silicon support[1]. Thanks to the thin thickness of the active volume a high γ-ray rejection is achieved, a key requirement in order to discriminate the signal coming from the neutrons in a mixed neutron-gamma ray environment.

The diodes have three-dimensional electrodes etched through the sili-

[1]This support can be removed using plasma etching or chemical solutions which stop at the silicon-oxide interface of the SOI wafer.

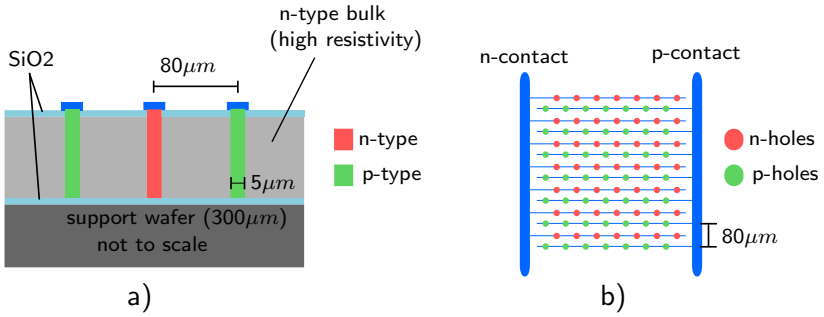

Figure 3.7: Sketch of the ultra-thin 3D silicon detector - The converter layer is not shown in the sketch, but this would be deposited over the detector front-side. (a) Cross section layout and (b) front-side view.

con and distributed in a square array with 80 µm pitch between columns of the same doping type (Figure 3.7(b)). The total area of the sensor is 0.57 cm^2. The electrode columns are an inactive volume inside the detector and therefore, they should be fabricated as narrow as possible. For the U3DTHIN the electrodes have 5 µm diameter and only one readout channel is present because all electrodes of the same type are connected together with aluminum lines.

Due to the electrodes penetrating into silicon, the depletion voltage in the 3D silicon detectors does not depend on the substrate thickness and the depletion region grows laterally as a cylinder from the p^+ electrodes. Considering the approximation of a coaxial-cable capacitor, the capacitance for 3D electrodes can be calculated as:

$$C = \frac{2\pi\varepsilon L}{ln(r_d/r_c)} \tag{3.7}$$

being L the column length, r_d the radius of the depleted region, and r_c the radius of the columnar electrode.

The lateral depletion of the ultra-thin devices allows for a much lower capacitance compared to a planar sensor of the same thickness (see Figure 3.8). For example, for a silicon U3DTHIN sensor with 20 µm thickness and 80 µm pitch, the capacitance is one order of magnitude smaller than

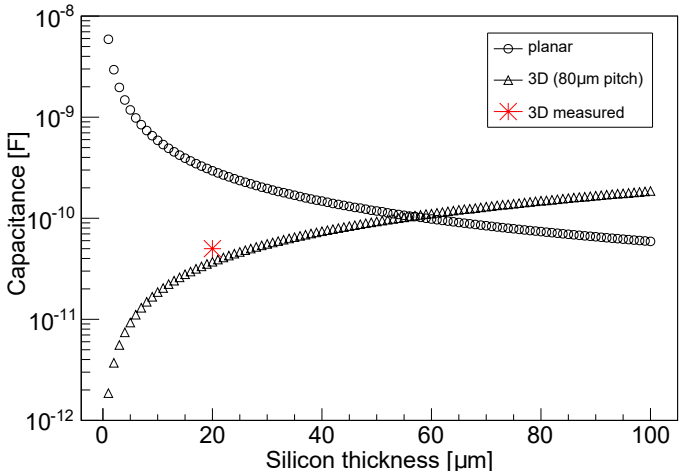

Figure 3.8: Capacitance of the planar and 3D (80 µm pitch) detectors versus silicon thickness - The parallel plate and cylindrical capacitor approximations were respectively used. The U3DTHIN structure is advantageous for thicknesses lower than 50 µm. The measured capacitance of a U3DTHIN with 20 µm thickness and 80 µm pitch is also shown in the plot.

for a planar silicon detector with the same thickness and surface area. The lower capacitance of these structures allows for lower electronic noise [31].

3.4.1 Fabrication process

The ultra-thin 3D silicon sensors were manufactured at the clean room of IMB-CNM on 4-inch SOI wafers supplied by Icemos Technology Ltd. A total of 6 n-type wafers doped with phosphorous with a nominal resistivity $>3.5\,\mathrm{k\Omega\,cm}$ and a active thickness of 10 or 20 µm were processed. The buried oxide and the support silicon thicknesses are 1 µm and 300 µm respectively. The whole fabrication process consists of 76 steps (without the deposition of the neutron converter layer). The main fabrication steps are briefly explained in the following paragraphs:

1. Before starting the fabrication process, the wafers were individually labeled in the backside for future identification, engraving the run[1] and the wafer number (this step is realized in all wafers processed wafers at the IMB-CNM clean room). Then, after cleaning the wafers with a "piranha" etch (H_2SO_4 and H_2O_2) and with HF to keep the surface free of any impurity, a silicon dioxide layer of 400 nm was grown with wet oxidation on both wafer sides (Figure 3.9).

Figure 3.9: SOI wafer and wet oxidation process.

2. First photolithography process to define the n-type columnar electrodes. The photoresist was spun on the front surface of the wafer and illuminated through the mask level I (holes-n) exposing the n-parts to ultraviolet light. The exposed resist was removed with a developer solution and afterwards, the SiO_2 underneath was removed with a buffered HF (Hydrogen Fluoride) mixture (Figure 3.10).

Figure 3.10: Photolitography process and SiO_2 etching.

[1] Word used in IMB-CNM to describe all fabrication steps required to manufacture a device

3. A column etching with a Deep Reactive Ion Etching (DRIE) process was then realized. The DRIE is an anisotropic process which, in order to get vertical high-aspect-ratio trenches, combines a plasma etching (with sulfur hexafluoride (SF_6)) with cycles of passivation (octafluorocyclobutane C_4F_8). After the DRIE process, all the photoresist was removed (Figure 3.11).

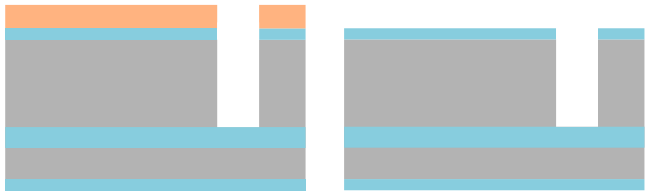

Figure 3.11: DRIE for n^+ columns and photoresist removal.

4. A 500 nm polysilicon deposition process was realized to fill partially the etched columns. Next, the polysilicon layer was doped n^+ with phosphorous atoms from a gas source ($POCl_3$) to form the ohmic contact of the sensor. Phosphorous atoms in contact with the deposited polysilicon create a PSG (phosphosilicate glass) layer which acts as a source of donor impurities and create the n-doped region. The next step was to etch away the PSG layer and to clean the wafer (Figure 3.12).

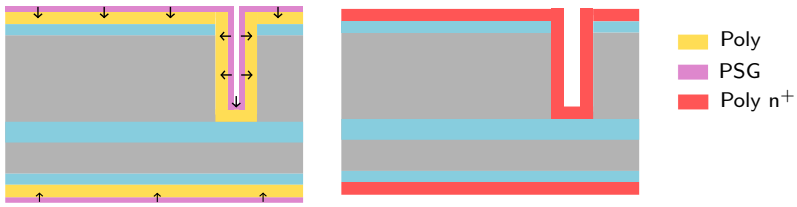

Figure 3.12: Polysilicon deposition and $POCl_3$ doping.

5. The next step is a second photolithography process to define the n-electrodes (mask level II (poly-n)). Then, the exposed photoresist and the 500 nm polysilicon layer under it were removed. The next

step was to clean all photoresist and to grow a silicon oxide layer of 100 nm on both sides that will protect the n^+ electrodes from the following steps (Figure 3.13).

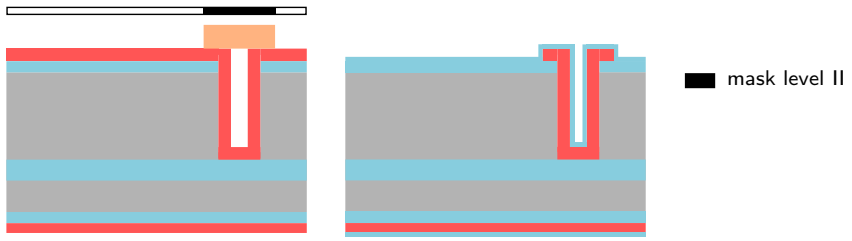

Figure 3.13: Photolithography process to pattern the poly-n^+ contacts and SiO_2 growth.

6. To define the p-type columnar electrodes the steps 2, 3, 4 and 5 were repeated with the following differences: i) the mask levels used were the mask level III (holes-p) and mask level IV (poly-p) and ii) the doping of polysilicon was done with p-type impurities from a solid BN source. Boron creates a BSG (borosilicate glass) layer in the polysilicon which acts as a source of acceptors impurities and creates the p-doped region (Figure 3.14).

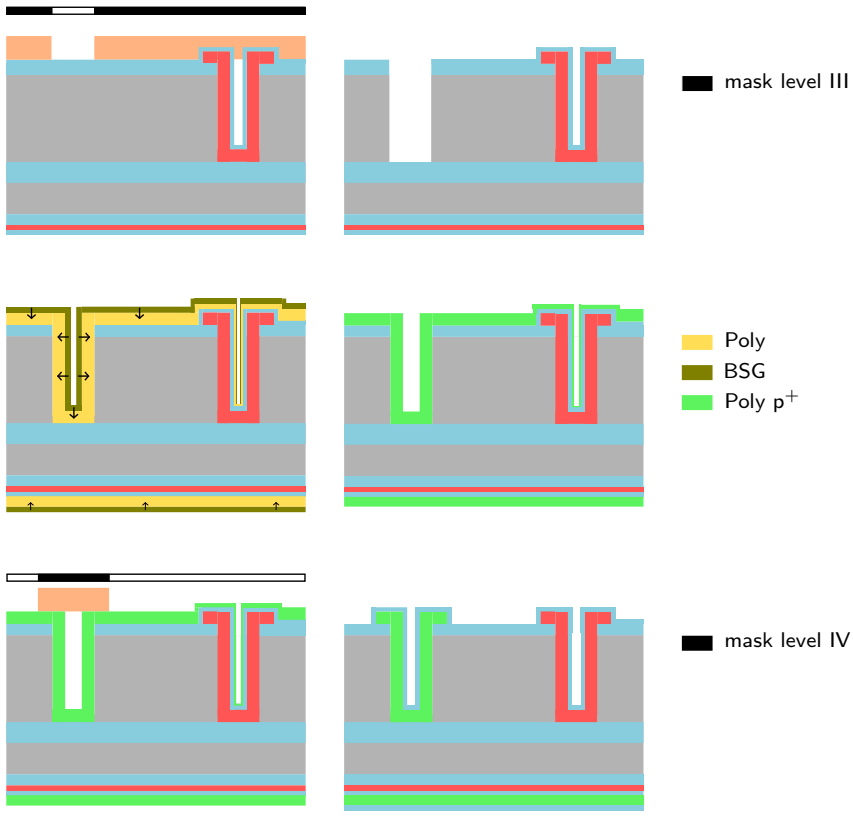

Figure 3.14: Fabrication process of the p-type columnar electrodes.

7. After the fabrication of both columnar electrodes, the photolithography process number five, through the mask level V (window), was realized to etch the SiO_2 layer on the top of the columnar electrodes. This process is done to provide a direct contact between the doped polysilicon and the metal (Al/Cu), which is deposited in the next step. The deposited metal is 0.5 µm thick (Figure 3.15).

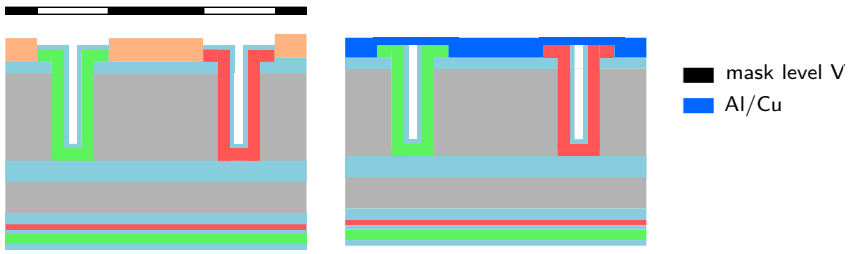

Figure 3.15: Photolithography process to etch the SiO_2 and metal deposition.

8. To end the fabrication, the photolithography process number six, through the mask level VI (metallization), was done to define the metal lines connecting the p^+ electrodes and the n^+ electrodes. Next, a passivation layer (SiO_2/Si_3N_4) was deposited by PECVD in order to protect the detectors from external exposure such as humidity and scratches. Finally, the contacts for the signal exit were opened through the passivation layer with the last photolithography process (mask level VII - passivation). This last photolithography process is not depicted in Figure 3.16 because the opened contacts are outside of the shown area.

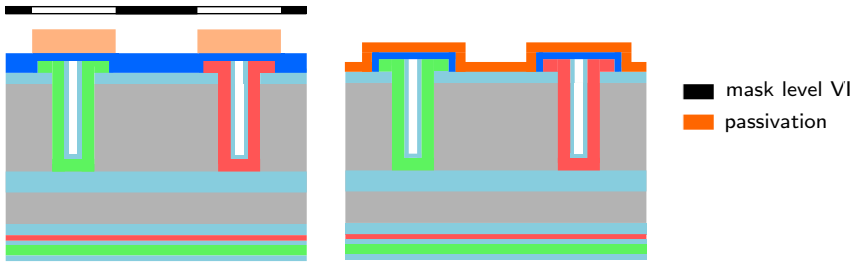

Figure 3.16: Photolithography process to each metal and passivation layer deposition.

The final step to achieve the neutron detector is to cover the ultra-thin 3D sensor with a neutron converter material. Section 3.4.3 explains the different converter materials and deposition techniques that have been

studied for this type of sensors.

One important parameter to take into account in neutron detectors is the entrance windows ("dead" or "contact" layer) that exists between the converter material and the silicon sensitive volume. This entrance window has to be as thin as possible in order to minimize the energy loss by the reaction products inside it. For the U3DTHIN structure this layer is in the range of 400 - 500 nm of SiO_2, as verified by SEM observation of the fabricated devices (see Figure 3.18), and is present in the 92.8% of the total surface area. The area not covered by the entrance windows, i.e. area covered by metal or polysilicon, is considered as inactive area and only constitute a 7.8% of the total area.

Figure 4.16c shows a picture of a U3DTHIN manufactured wafer.

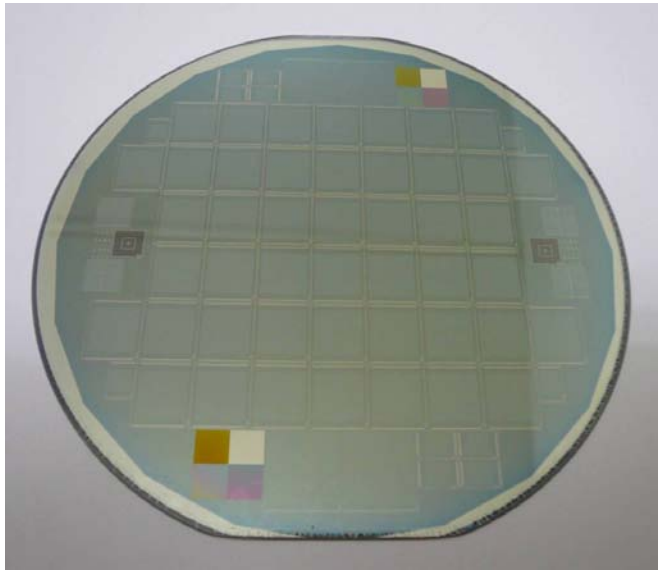

Figure 3.17: Photograph of manufactured wafer with ultra-thin 3D sensors - The central area contains an array of 42 7x7 mm^2 U3DTHIN sensors.

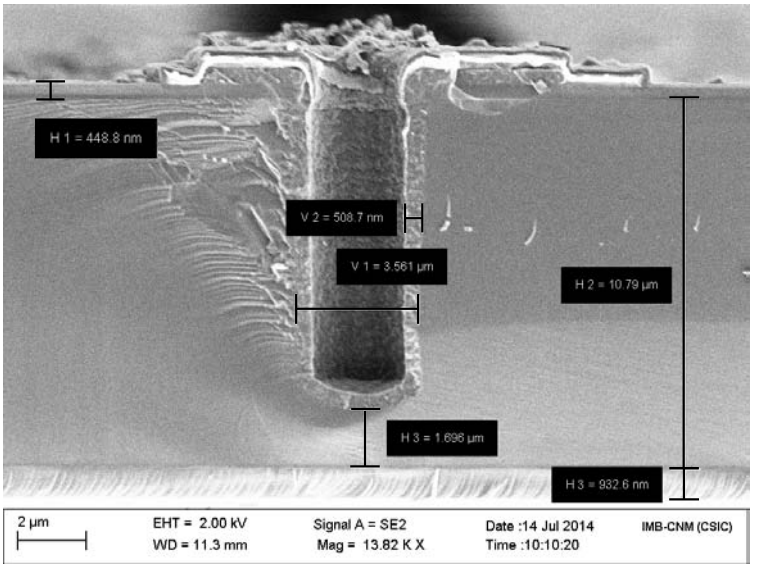

Figure 3.18: SEM image of a columnar electrode of the U3DTHIN sensor - Detail of a hole that forms a columnar electrode (from the up bottom): ∼400 nm field oxide (dead layer), ∼500 nm doped polysilicon, ∼3.5 µm etched column width, ∼10 µm-thick sensor active thickness, ∼1.5 µm space between column and buried silicon oxide, ∼1.0 µm-thick buried silicon oxide layer.

3.4.2 Electrical characterization of U3DTHIN

The electrical characterization of all wafers was performed as is explained in Appendix A. Figure 3.19a shows the current versus reverse voltage curves for all the sensors in one wafer (42 sensors, 20 µm thick). From that measurements two conclusions are extracted: i) only a few devices suffer early breakdown (red curves) while the rest have breakdown voltages >50 V (green curves); ii) average leakages currents at 20 °C are (0.09 ± 0.02) µA/cm^2 at 10 V and (0.34 ± 0.12) µA/cm^2 at 30 V.

Figure 3.19b shows the measurements of capacitance versus reverse voltage of some sensors. Due to surface effects, two different depletion regions can be distinguished in the figure; one at 10 V representing the lateral depletion of the columnar electrodes, and the other at 30 V corre-

sponding to full depletion. A full sensor depletion is not reached at 10 V due to the positive charges present at the SiO_2, which create an accumulation layer of electrons at the Si-SiO_2 interface. This electron layer requires an increase of bias voltage to fully deplete the detector. Therefore, the U3DTHIN full depletion voltage presents a strong dependence with the surface oxide charge and the detector thickness [32]. The full depletion voltage for the 20 µm thick sensors is approximately 30 V with a capacitance of $(50 \pm 10) \cdot 10^{-12}$ F (see Figure 3.8).

The total manufacturing yield (ratio of devices with good electrical characteristics to all fabricated devices) of the entire fabrication batch was 91%.

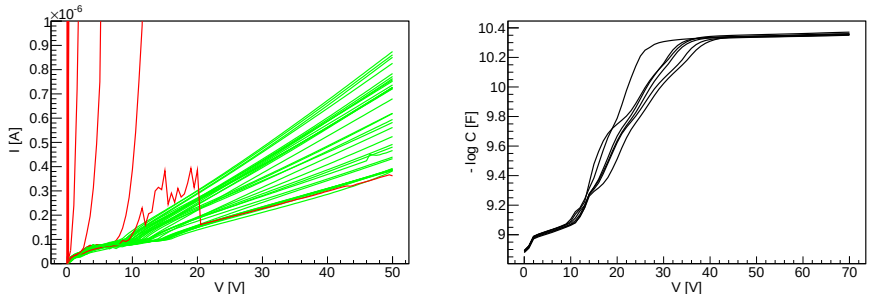

(a) **(b)**

Figure 3.19: Characterization of the ultra-thin 3D sensors - (a) I-V curve of all sensors in one wafer and (b) C-V curve.

3.4.3 Neutron converters for U3DTHIN

In order to adapt the U3DTHIN sensor for thermal neutron detection a boron-based converter layer was deposited on its front surface. Two different converters were tested; boron carbide 99% enriched in ^{10}B ($^{10}B_4C$) and the BE10 screen manufactured by Kodak. Moreover, the U3DTHIN sensor was also tested as a fast neutron detector. To adapt the sensors for this purpose a polyethylene layer was placed on their front surface.

3.4.3.1 Boron carbide deposition

Boron carbide ($^{10}B_4C$) enriched 99% in ^{10}B was deposited in the front side of the ultra-thin silicon sensors by Physical Vapor Deposition (PVD) at the University of Barcelona (Figure 3.20) [33, 34, 35, 36]. Boron carbide is technically less challenging to deposit than pure ^{10}B, has high hardness (up to 40 GPa) and moreover, high chemical and thermal stability.

PVD is a collective set of processes used to deposit thin layers of material, typically in the range of few nanometers to several micrometers, onto a solid substrate. The two most common PVD processes are thermal evaporation and sputtering. In this work $^{10}B_4C$ was synthesized as target for sputtering PVD process.

Sputtering PVD process is a plasma-assisted technique that creates a vapor from the target (material that is going to be deposited) through bombardment with accelerated gaseous ions (typically Argon) and then, the resulting vapor phase is subsequently deposited onto the desired substrate through a condensation mechanism.

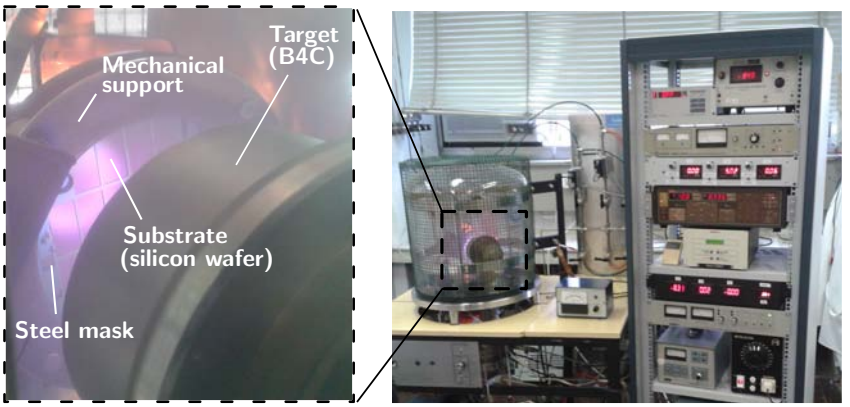

Figure 3.20: Photographs of the RF sputtering machine at the University of Barcelona - The chamber base pressure was 10^{-4}Pa, the RF power was 350 W and the substrate bias voltage was kept to a positive value of +10 V using the tuned RF magnetron sputtering technique [37].

Prior to deposition, the silicon wafer containing the ultra-thin sensors

was cleaned in an ultrasonic bath with de-ionized water and dried in dry nitrogen, then it was mounted in a mechanical support which was fitted inside the sputtering machine.

A key parameter in this process is the control over the energy of the bombardment of the argon ions. This has influence on the mechanical properties of $^{10}B_4C$ films because when the argon ion energy increases, the stress of the $^{10}B_4C$ coating increases as well [38]. Another important parameter is the deposition rate which in our case was constant to 0.5 µm/h. By means of a thin steel mask (see Figure 3.20), the $^{10}B_4C$ was selectively deposited only on the active areas of the wafer leaving the electrical contacts of the sensors free.

To estimate the optimum $^{10}B_4C$ thickness, the intrinsic thermal neutron detection efficiency was previously calculated with Geant4 simulations. The intrinsic efficiency of a sensor, ε, for a normally incident neutron beam is defined as the ratio of the detector response (counts or count rate) R_{det} to the total neutrons hitting the detector active area R_i (Equation 3.8). The intrinsic efficiency takes into account the projected detector areas as a function of the angle relative to the radiation beam.

$$\varepsilon = \frac{R_{det}}{R_i} \tag{3.8}$$

Figure 3.21a shows the simulated intrinsic thermal neutron efficiency of the U3DTHIN silicon detector for different layer thicknesses and densities of the $^{10}B_4C$ converter material[1] (to compare, the efficiency of a ^{10}B bulk density (2.46 g/cm^3) layer is also depicted). For low converter densities, the range of the charged particles is higher, but at the same time there is a lower number of ^{10}B target atoms per unit volume, resulting in a smaller number of neutron captures. Hence, for converter with higher density the efficiency rises faster than for those with lower density and, once peaked, decreases more rapidly.

[1]The bulk density of $^{10}B_4C$ is 2.52 g/cm^3 but densities of deposited layers are likely to be lower than the bulk value and depend strongly on the conditions of the deposition process [13].

The highest possible detection efficiency of $^{10}B_4C$, independently of the density layer, is about 3.68%. This value is achieved with 3.00 µm of 2.00 g/cm^3, with 2.75 µm of 2.25 g/cm^3 or with 2.50 µm of 2.52 g/cm^3.

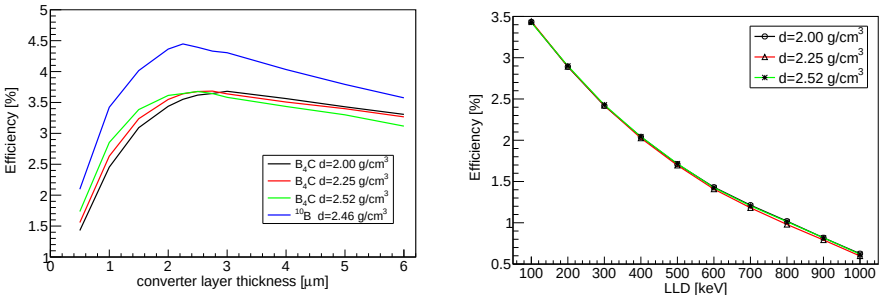

(a) **(b)**

Figure 3.21: Simulated thermal neutron detection efficiency of a 20 µm U3DTHIN covered with a $^{10}B_4C$ or ^{10}B converter layer. The front-face configuration was used. (a) Efficiency as a function of different $^{10}B_4C$ densities with an LLD=0 keV. The efficiency of a 2.46 g/cm^3 of ^{10}B layer is also depicted. (b) Efficiency of a 3.00 µm (d=2.00 g/cm^3), 2.75 µm (d=2.25 g/cm^3), 2.50 µm (d=2.52 g/cm^3) $^{10}B_4C$ layer thicknesses for different LLD values.

The reduction efficiency factor of $^{10}B_4C$ in comparison with ^{10}B is due to the atomic fraction of ^{10}B in $^{10}B_4C$ ($^{10}B_4C$ contains 78.6% of ^{10}B in weight).

Figure 3.21b shows the efficiency as a function of different LLD values for the thicknesses which achieve the highest efficiency. Changes in the lower values of LLD show bigger drops of efficiency because for the ^{10}B reaction products, more counts are placed in the low energy range of the spectrum.

Another important aspect that has to be considered in the neutron coated sensors is the side of the irradiation because neutrons, when passing through the converter, follow the exponential attenuation law. Figure 3.22a depicts the two possible irradiation configurations and also shows that exponential attenuation. If the detector is irradiated from the front side (beam hitting first the converter material) more neutrons are captured

close to the neutron beam and therefore the chance of reaction products reaching the sensitive volume is lower. On the other hand, if the detector is irradiated from the back side, higher number of neutrons are captured close to the boundary between the semiconductor and the converter, and therefore the probability of reaction products reaching the silicon sensitive volume is higher.

Figure 3.22b shows the simulated differences in efficiency when the detector is irradiated from front-side or from back-side. The simulated detector is a 20 µm thick U3DTHIN covered with $^{10}B_4C$ (density of 2.0 g/cm^3). In both curves the detection efficiency is increasing up to the optimum layer thickness, however, for thicker layers there is an efficiency reduction in the front irradiation while in back irradiation it is kept constant. It is important to mention that for boron based converters, due to low range of its reaction products, this irradiation-side dependance is observable for thicknesses ≥3 µm while for ^{6}LiF, the effect is only significant for converter thicknesses ≥15 µm.

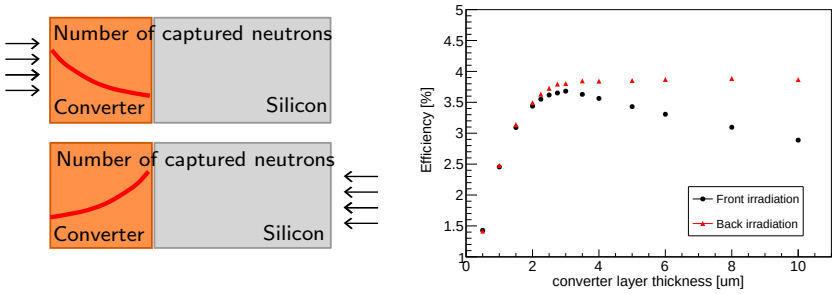

Figure 3.22: (a) Schematics of the frontal and the backside irradiation showing the number of neutrons captured in the neuron converter. (b) Simulated detection efficiency as a function of the $^{10}B_4C$ converter thickness (density of 2.0 g/cm^3) for the front and backside irradiation.

Following the simulation results, a $^{10}B_4C$ layer in the range of 2.5 - 3 µm was deposited by PVD on the front side of the whole silicon wafer.

Figure 3.23 shows the thickness profile of the layer through two entire sensors obtained with a mechanical profilometer. The figure shows the desired step produced by the steel mask and the roughness due to the metal lines that connect the electrodes. The layer showed good adhesion and homogeneity over the whole wafer.

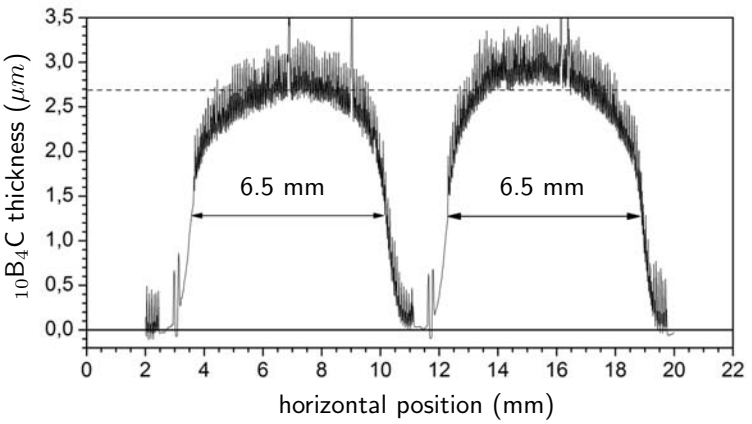

Figure 3.23: Profilometry measurements of the $^{10}B_4C$ layer deposited over the silicon wafer - The mean $^{10}B_4C$ thickness is 2.7 µm.

After the layer deposition, the wafer was diced and some of the U3DTHIN detectors were re-tested. The measurement showed that their electrical characteristics had not been significantly affected by the $^{10}B_4C$ deposition and wafer dicing. Detectors with the best electrical performance were selected for testing in the nuclear reactor beam.

3.4.3.2 BE10 screen

The BE10 screen manufactured by Kodak consists in a 40 µm mixture of 93% enriched boron-10 boron carbide with glue coated on a 100 µm thick polyester base (Figure 3.24a). The BE10 screen was supplied by Dosirad [39]. Despite additional substances in the converter material (carbon and glue) may reduce neutron detection efficiency, this method has been used due to its simplicity to adapt the U3DTHIN sensor into a neutron detector;

the BE10 screen is cut to the desired size and stuck manually over the sensor. The 100 µm polyester base on the top of the screen is an invisible layer for thermal neutrons.

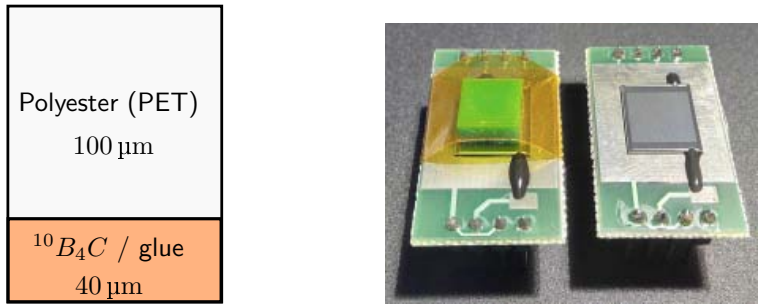

(a) **(b)**

Figure 3.24: (a) Sketch of the BE10 screen manufactured by Kodak. (b) Two U3DTHIN sensors with and without the polyethylene (7x7x3 mm^3) for fast neutron detection.

3.4.3.3 Polyethylene layer

To adapt the U3DTHIN sensors for fast neutron detection an hydrogen-rich 3 mm thick polyethylene sheet was placed on its front surface (Figure 3.24b). Fast neutrons interact by direct elastic scattering with the hydrogen nuclei (protons) in the polyethylene and the recoiling protons that enter the silicon ionize the surrounding material and are detected (see section 3.6.2.2).

3.5 Microstructured sensors

The microstructured (MS) sensors fabricated at the IMB-CNM clean room consist of an array of sinusoidal or hexagonal microchannels etched inside the silicon bulk (Figure 3.25). The p-n junction that turns these structures into a particle detector is located inside the trench walls. Compared with planar devices, these structures increase the contact surface between the

converter and the silicon detector and thus are able to achieve high neutron detection efficiencies.

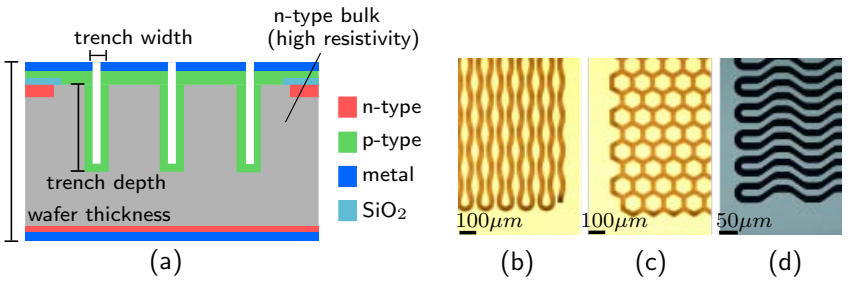

Figure 3.25: Sketch of the microstructured silicon sensor - (a) schematic cross-section (not to scale). Right: Top view optical microscope images of (b) sinusoidal and (c) hexagonal arrays for the first fabrication batch, and (d) optimized sinusoidal array for the second fabrication batch. The total area of the sensors is 1 cm^2.

The MS sensors are fabricated on n-type high resistivity wafers with active thickness of 300 or 400 µm. Two fabrication batches of the microstructured neutron detectors were done in the clean room facilities:

The first batch was fabricated on 300 µm thick wafers with the patterns shown in Figure 3.26. The design and dimensions of these patterns (trench width (L) and depth (h) and width of the silicon wall between channels (W)) were based on a previous MCNPX-Monte Carlo simulation study of rectangular patterns etched into the silicon substrate and filled with boron-based converter materials [40]. The final decision for the first fabrication batch was to manufacture four different trench width values, all with 150 µm trench deep for both sinusoidal and hexagonal patterns, to enhance the probability of obtain satisfactory results in the filling process. The main parameters of these patterns are summarized in Table 3.4.

A complete GEANT4 simulation study of the first batch microstructured neutron sensors filled with boron-10 or lithium-^{6}Li fluoride is presented in section 3.5.4.

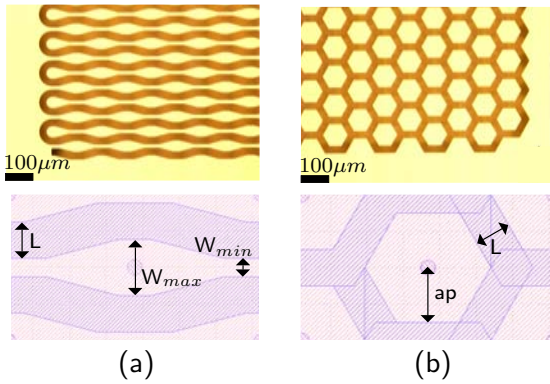

Figure 3.26: Top view pattern designs for the first fabrication batch - Optical microscope image and unit cell layout of the (a) sinusoidal and (b) hexagonal design.

Table 3.4: Main parameters of the first batch fabricated designs - Table summarizing the main parameters as well as the percentage of converter material inside unit cell (%cell fraction). For all sinusoidal geometries W_{min} is fixed to 12 µm.

channel width L	SINUSOIDAL		HEXAGONAL	
	W_{max} (μm)	% cell fraction	apothem (μm)	% cell fraction
06 μm	26.0	23.4%	22.0	22.5%
10 μm	28.0	36.0%	25.0	30.8%
15 μm	28.0	46.0%	27.5	38.6%
25 μm	38.0	54.2%	37.5	43.9%

The second batch was fabricated with the pattern shown in Figure 3.27. The dimensions of this pattern were optimized with GEANT4 simulations considering ^{6}LiF as a neutron converter material (and not boron-based converter materials as in the first batch) and only viable ranges for MEMS fabrication techniques, i.e. designs that may be produced with standard MEMS techniques in a clean room facility that ensures the repetitiveness and viability of mass-production. The sensor active area is 1.00 cm^2 with

230 or 345 µm trench depth. The GEANT4 simulations are also shown in section 3.5.4.

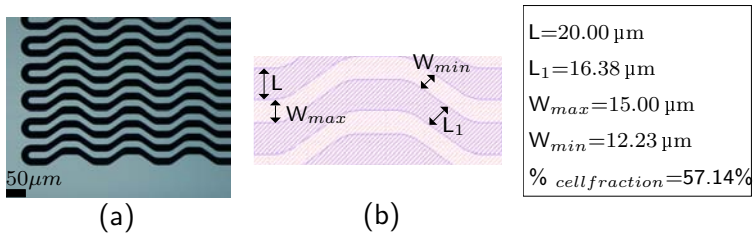

Figure 3.27: Sinusoidal design of the second fabrication batch - (a) Optical microscope top view image and (b) Unit cell layout (160x70 µm^2) with the optimized GEANT4 values for ^{6}LiF.

3.5.1 Fabrication process

The microstructured silicon sensors were manufactured at the IMB-CNM clean room on high resistivity wafers supplied by Topsil. A total of 28 n-type wafers (12 sensors per wafer) doped with phosphorous with a nominal resistivity >5.0 kΩ cm were processed. The first batch of sensors were fabricated on 300 µm wafers while in the second batch 400 µm wafers were also used. The whole fabrication process consists of 63 steps (without the deposition of the neutron converter layer) which are depicted in Figure 3.28 and briefly summarized in the following paragraphs:

First, the wafers are chemically cleaned and a 800 nm silicon oxide is grown on both sides of the clean wafers. Then, a photolithography process followed by a SiO_2 removal and a phosphorous implantation is realized to define the channel stop[1] on the front-side and the ohmic contact (n^+ region) on the backside of the wafer.

Two photolitography process are then realized; the first one to define the sensor area on the wafer and the second one to pattern the trench geometry. A 1 µm metal layer is deposited before the second photolithography process to act as a mask for the DRIE.

[1] n^+ region at the edge of the chip to isolate the detector structure of surface currents

Then, after metal and SiO_2 etching, the array of microchannels is etched into silicon by the DRIE process. Trenches are partially filled with 200 nm of polysilicon and are doped with boron (p^+ region). The final step is to deposit a metal layer of 0.2 µm and 1 µm in front and back-face respectively, to create the electrical contacts, and dicing the individual sensors.

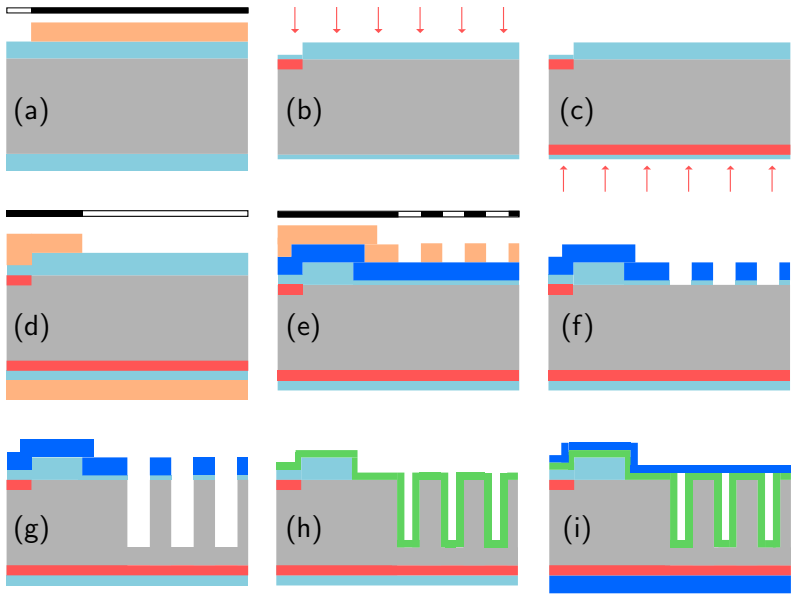

Figure 3.28: Summarized sketch of the microstructured sensor fabrication process - (a) 800 nm SiO_2 growth and photolithography process to etch the SiO_2. (b) and (c) Phosphorous implantation for the channel stop and ohmic contact respectively. (d) Photolithography to define the sensor area. (e) Metal layer deposition plus photolithography process to pattern the trench geometry. (f) Metal and SiO_2 etching. (g) DRIE process to etch the silicon. (h) Polysilicon deposition and polysilicon doping (p^+ region). (i) Metal deposition.

Figure 3.29 shows a picture of a manufactured wafer of the MS sensors and Figure 3.30 shows a cross-section SEM image of one MS sensor from the second fabricated batch.

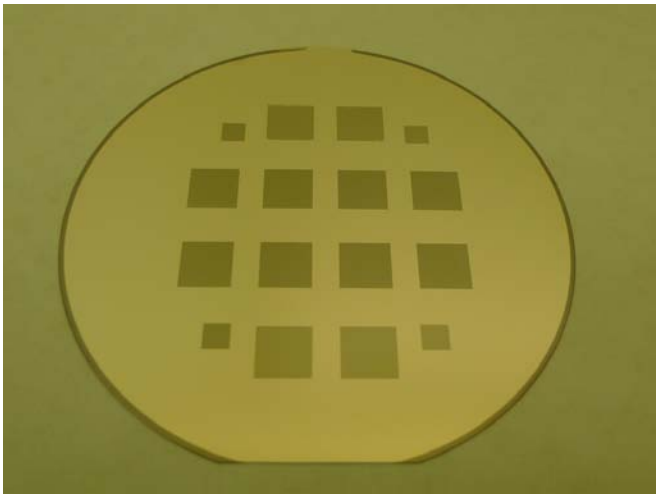

Figure 3.29: Photograph of manufactured wafer with microstructured sensors - The wafer contains 12 1x1 cm^2 and 4 5x5 mm^2 MS sensors.

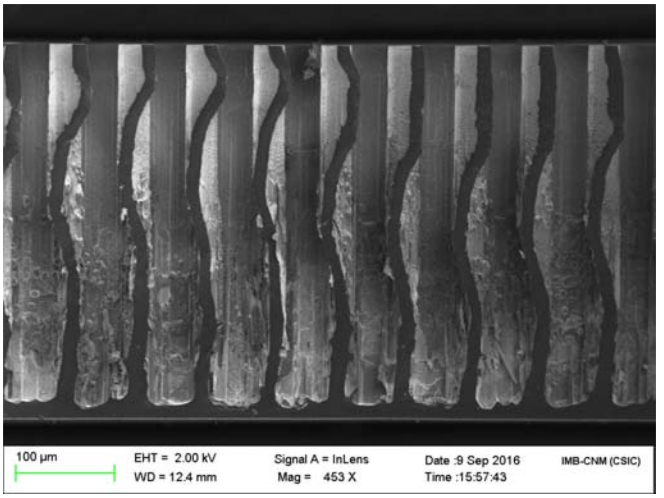

Figure 3.30: SEM image of the MS sensor cross-section - The image corresponds to a sensor of the second fabrication batch in a wafer of 400 µm.

3.5.2 Electrical characterization of microstructured sensors

The electrical characterization of all wafers was done as explained in Appendix A. Figure 3.31a shows the current versus reverse voltage curves for some sensors from the first fabrication batch. No difference in current behavior has been observed between the sinusoidal and hexagonal structures. Average leakage currents at 20 °C are (0.18 ± 0.08) µA/cm^2 at 3 V for most of the sensors (green curves). Figure 3.32a shows the same plot for sensors of the second fabrication batch. Comparing these figures it is observed that current increases as the trench depth becomes larger due to surface effects in the wall of the trench. For the second batch of sensors there is a wider set of current behaviors so, in a first approximation sensors were considered suitable for the filling process if leakage current at 20 °C is $\leq$5.0 µA/cm^2 at 3 V (green curves).

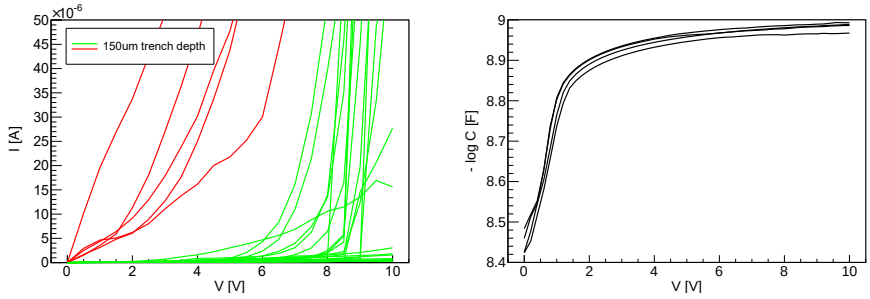

(a) (b)

Figure 3.31: Characterization of the first batch microstructured sensors - (a) I-V (b) C-V curves for some sensors

Figure 3.31b shows the measurements of capacitance versus reverse voltage of some sensors from the first fabrication batch. According to the structure of devices, two depletion regions would be observed; the first one corresponding to lateral depletion (region between the etched columns) and the other corresponding to full depletion, where all wafer thickness is depleted. In Figure 3.31b only a lateral depletion at $\approx$1.5 V is observed for voltages up to 10 V. To fully deplete the sensor higher voltage values are

required but, as it will be seen in section 3.6.3, it is no needed; a partially depleted detector is already optimum to collect all the signal produced by the charged particles from the nuclear neutron reaction and moreover, a fully depleted sensor would reduce its gamma discrimination factor. For microstructured first batch sensors, the operating voltage was defined as 3 V in order to have a compromise between the electronic noise and sensitivity to gamma radiation. The capacitance versus voltage characteristics of sensors from the second fabrication batch (Figure 3.32) present comparable behavior as the first batch but with a more pronounced increase from 0 to 1.5 V. This means faster lateral depletion that could be attributed to the use of wafers with slightly higher resistivity.

The lateral depletion voltage for the measured 150 µm trench deep sensors is 1.5 V with a capacitance of $1{\cdot}10^{-9}$ F.

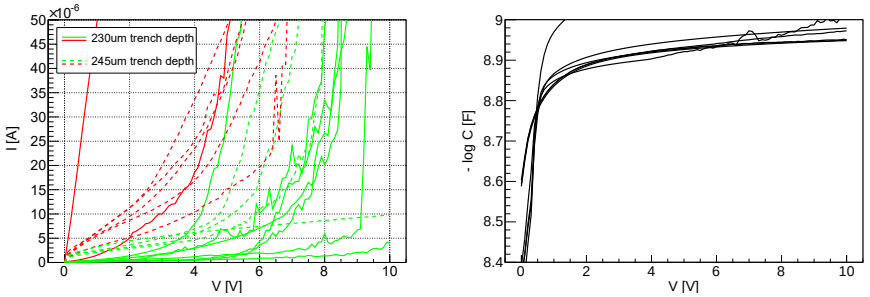

(a) (b)

Figure 3.32: Characterization of the second batch microstructured sensors - (a) I-V (b) C-V curves for some sensors

3.5.3 Neutron converters for microstructured sensors

In order to adapt the microstructured sensors for a thermal neutron detection, boron-10 and lithium-6Li fluoride materials supplied by Sigma-Aldrich Products [41] (Figure 3.33) were selected as converter materials to fill the perforated trenches.

The main advantages of ^{10}B over ^{6}Li are higher microscopic thermal

(a) **(b)**

Figure 3.33: Converter materials used to fill the microstructured sensors - (a) Boron-^{10}B, 90 atom % ^{10}B. (b) Lithium-6Li fluoride, 95 atom % ^{6}Li, 99% (CP).

neutron absorption cross section (3840 b versus 940 b) and cheaper price, however the reaction products from ^{6}Li are more energetic than those from the ^{10}B and hence, are much easier to detect and discriminate from background radiations.

Over the past 10 years various filling methods like physical vapor deposition, ultrasonic deposition of particles, pressure filling (handpacking), plasma deposition, low pressure condensation and centrifugation have been explored by other groups [25, 27, 42] and also by IMB-CNM reporting, in all cases, a challenging issue for deep microstructures with high aspect ratio.

The Physical Vapor Deposition with an Electron-Beam-Gun (EBPVD) and the liquid filling [43, 44] were the previously explored methods by the CNM Radiation Detector Group to achieve a complete filling of trenches with optimum packaging density and without pinholes or hollows inside them. However, the ^{10}B EBPVD showed little filling success for high aspect ratio designs and adhesion problems due to stressed evaporated layers, while liquid filling with o-carboranes presented toxicity and complicated filling processes. Due to these drawbacks, the selected filling method used in this thesis was the pressure handpacking, that consists of spreading the

converter material on the sensor surface and applying pressure by hand to force the converter to enter into the perforated structure.

Both boron-10 and lithium-6Li fluoride powders were previously ground by a vibratory ball mill to achieve micron-sized homogenized granules and make the filling process more efficient. A vibration ball mill (Figure 3.34a) performs high speed vibrations to a grinding jar filled with the grinding balls and the material to be processed. The inertia of the grinding balls causes them to impact with high energy on the sample material at the rounded ends of the grinding jars and pulverize it.

(a) **(b)**

Figure 3.34: Vibratory ball mill and grinding jars balls - (a) Vibratory ball mill model Mixer Mill MM 200 and (b) grinding jars and balls of different sizes and materials. Typical materials of grinding tools are hardened steel, stainless steel or tungsten carbide.

Although the first fabrication batch of microstructured sensors were optimized for boron-based converter materials [40], both sinusoidal and hexagonal patterns were also filled with ^{6}LiF to compare the detection efficiencies. Figure 3.35 shows SEM images of sinusoidal and hexagonal designs filled with loose ^{6}LiF powder via the first hand-packing tests. These SEM images of cross-sections have been done with a diamond point scribe to avoid removing the converter filling. Even then, some parts of the fillings have come out, as it visualized in the images. From these photos, it can be concluded that the powder-fill method is effective and fills the

perforations; however it leaves few voids which reduce the packing fraction of the neutron converter. No differences were found in the ^{10}B and ^{6}LiF filling processes.

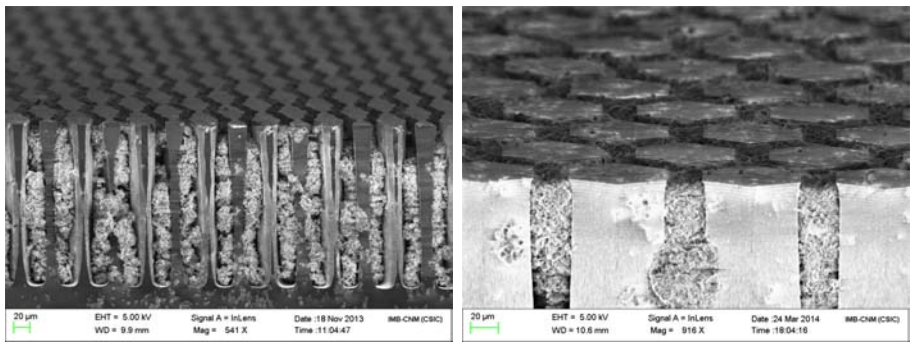

(a) **(b)**

Figure 3.35: SEM image of hand-packed ^{6}LiF powder in the first fabrication batch sensors - (a) sinusoidal and (b) hexagonal patterns from the first fabrication batch. The trench width is 15 µm for the sinusoidal design and 25 µm for the hexagonal. Trench depth is 150 µm. Note that the cleaving process dislodges the packed converter from the trenches, so the SEM images are only indicative of the final filling within the trenches.

It must be said that only sensors with 15 or 25 µm trench width were considered as thermal neutron detectors because the filling process of 6 and 10 µm trench widths was not efficient. For 6 and 10 µm a non uniform packaging with pinholes and hollows inside the trench was observed by SEM images. In most cases, for these small trench widths, the converter material formed agglomerations above the perforations preventing the filling.

The first tests at the Portuguese Research Reactor (RPI) were done with this first batch of microstructured detectors showing satisfactory results for ^{6}LiF converter material (see section 3.6.3), however a new packaging method which avoids empty spaces and increases the packing of the powder inside trenches was desired to achieve higher detection efficiencies.

The solution was found in the Lithium-ion battery manufacturing in-

dustry. Lithium-ion batteries use binders, such as SBR (Styrene Butadiene Rubber) or PVDF (Polyvinylidene Fluoride), to hold the active material particles together and in contact with the current collectors [45]. In our case, PVDF[1] holds the ^{6}LiF particles together and avoids in this way, the empty space inside trenches. For this, an appropriate proportion of NMP[2] (N-Methyl 2-pyrrolidone) solvent was mixed with the ^{6}LiF and PVDF blend to create a paste which improves the filling process. The main advantages of this mixture are: i) the small amount of blinder needed (1-2% in weight) which will not influence efficiency and ii) the solvent will be not present inside the trenches because it evaporates. This approach was suggested by scientists from Institut de Ciencia de Materials de Barcelona (ICMAB), experts in lithium-ion batteries.

To find out the optimal amount of solvent to add in the ^{6}LiF and PVDF mixture, different tests were done with different microliters of NMP, ranging from 20 µl to 100 µl for every 100 mg of total powder. Results showed that 60 µl was the best choice to create the appropriate paste for trench filling because i) lower quantities produced a too dense agglomeration not optimum to enter to trenches and ii) higher quantities are useless in terms of neutron detection efficiency. With this amount of solvent, different mixtures with different percentages in weight of ^{6}LiF and PVDF were also prepared with the aim of reducing as much as possible the amount of PVDF but keeping good packing density without voids inside the trenches. Table 3.5 shows all these tested mixtures.

No substantial differences were observed by SEM images in terms of packing density for the different mixtures, therefore the final decision was to adapt all microstructured sensors with the lowest percentage in weight of PVDF (mixture 4 of Table (3.5)). Figure 3.36 shows SEM images of trenches filled with mixture number 4. These images correspond

[1]PVDF ($C_2H_2F_2$) is a partially fluorinated semi-crystalline polymer with excellent thermo-mechanical and chemical properties. It has demonstrated an ability to withstand irradiation to a dose of 10^7 rads in air or vacuum [46].

[2]NMP is a polar cyclic organic solvent. Characteristic properties of NMP include low viscosity, excellent dissolving power and enhanced demulsifying property.

to the first batch with 25 µm sinusoidal trench width and 150 µm depth. Other tests with sinusoidal trenches of 15 µm width and 270 µm depth also showed good packaging density without voids with the mixture number 4.

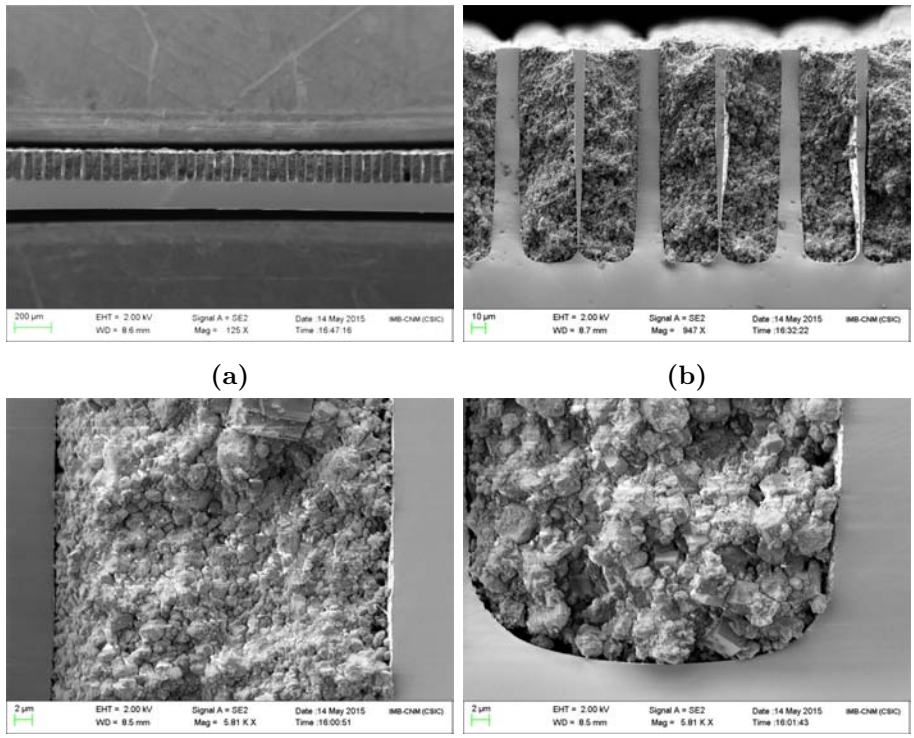

Figure 3.36: SEM images showing a cross section view of the microstructured sensors filled with ^{6}LiF mixture number 4 (2% in weight of binder) - The sensor has 25 µm sinusoidal trench width and 150 µm deep. (a) Full cross-section of sensor. All visible trenches are completely filled except one (which presents a void probably due to the cleaving process). (b) Image showing completely filled trenches with no voids and a high packing fraction. Photographs (c) and (d) show the tightly packed ^{6}LiF and PVDF micropowder.

Table 3.5: Proportions in weight of the mixtures tested for trench filling. In all mixtures the amount of MNP was fixed to be ∼60 µl for every 100 mg of powder.

	Weight percentage of ^{6}LiF	**Weight percentage of PVDF**	**NMP (µl)**
mixture 1	(89.5 ± 0.2)%	(10.5 ± 0.1)%	60.0 ± 0.5
mixture 2	(92.0 ± 0.2)%	(8.0 ± 0.1)%	60.0 ± 0.5
mixture 3	(95.4 ± 0.2)%	(4.6 ± 0.1)%	60.0 ± 0.5
mixture 4	(98.0 ± 0.3)%	(2.0 ± 0.2)%	60.0 ± 0.5

3.5.4 GEANT4 simulations of microstructured sensors

A complete simulation study has been done for both batches of microstructured sensors. The first fabrication batch (sinusoidal and hexagonal perforations with 6, 10, 15 and 25 µm trench width and 150 µm trench depth) filled with ^{10}B or ^{6}LiF was simulated and analyzed in terms of radiation beam direction and converter material density. On the other hand, simulations of the second batch were realized previously to fabrication, so the study was focused on finding out the optimum trench width and depth for a ^{6}LiF filling.

The density of the converter has a direct impact on two parameters: the mean free path (λ) and the range of the neutron capture reaction products emitted inside the converter. In this thesis the filling technique makes use of the powdered material so the real packing densities achieved inside the trenches are lower than the intrinsic particle density of the material. In particular, the particle densities of ^{6}LiF and ^{10}B are 2.54 g/cm^3 and 2.34 g/cm^3 respectively, but the bulk density depends on the compacted state of the crushed powder [47]. This changeable density characteristic may affect the whole efficiency considerably and thus it needs to be taken into account when measured and simulated results are compared. Figure 3.37 illustrates how the thermal neutron mean free path decreases

inversely proportionate to the ^{10}B or ^{6}LiF bulk densities.

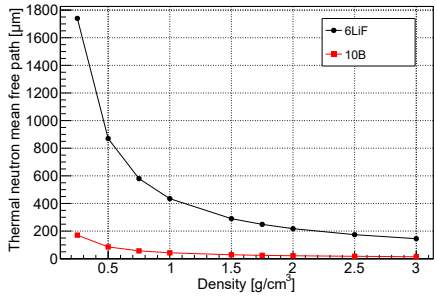

Figure 3.37: Thermal neutron mean free path as a function of ^{10}B or ^{6}LiF density - The mean free path for thermal neutrons drops markedly when the density increases.

Table 3.6 contains the average ranges (estimated with the SRIM software [48]) of the charged particles produced inside both converter materials for different bulk densities. It shows that the ranges of reaction products are doubled when the converter density is halved. The ranges inside silicon are also depicted in the table.

To quantify the goodness of the different prototypes the intrinsic detection efficiency has been established as the key parameter. The following considerations were made in the simulations in order to approximate the characteristics of the simulated design and the manufactured sensors: (i) there is no air between the converter and the SD, (ii) there is a dead layer of 0.5 µm inactive silicon on the front face and on the etched walls of the devices (to account for the effect of the heavily doped p+ diffusion), (iii) the energy cut-off, understood as equivalent to the lower limit of detection (LLD), is fixed as 10 keV. The simulation errors for all cases were $\leq 0.1\%$.

Table 3.6: Range of reaction products inside its respective converter material and inside silicon.

Material	Bulk density (g/cm^3)	Range µm	
		Alpha (1.47 - 1.78) MeV	**^{7}Li (0.84 - 1.01) MeV**
^{10}B	2.5	3.1 - 3.8	1.6 - 1.8
	2.0	3.8 - 4.8	2.0 - 2.2
	1.5	5.1 - 6.3	2.7 - 3.0
	1.0	7.7 - 9.5	4.0 - 4.5
	0.5	15.4 - 19.0	8.0 - 8.9
Silicon	2.32	5.2 - 6.3	2.6 - 2.8
	Bulk density (g/cm^3)	**Alpha (2.05 MeV)**	**^{3}H (2.73 MeV)**
^{6}LiF	2.5	6.1	34.2
	2.0	7.7	42.8
	1.5	10.2	57.1
	1.0	15.3	85.6
	0.5	30.7	8171.0
Silicon	2.32	7.5	44.1

3.5.4.1 Simulations of the first batch

As a first approximation, the neutron capture probability should increase if the volume backfilled with neutron converter rises, i.e. if the trench width or trench depth dimensions are maximized. In contrast, if trench width is too large, the probability of the reaction products reaching the sensitive volume decreases since they lose energy within the converter.

The converter material volume inside the sensor (% cell fraction) increases as the trench width increases (see Table 3.4). Figure 3.38 displays the proportion of neutron capture reactions taking place inside the neutron

converter material for both hexagonal and sinusoidal designs as a function of the micro-channel width when these designs are irradiated by a thermal neutron beam (front-face irradiation direction 3.39a). Figure 3.38 shows that: (i) there are more nuclear reactions inside the ^{10}B converter than within ^{6}LiF due to the higher ^{10}B thermal neutron capture cross-section; (ii) the sinusoidal design yields more nuclear reactions than the hexagonal one since the percentage of converter material inside the unit cell is higher for the former. Note that although more nuclear reactions may take place for larger trench widths, in turn the reaction products could be absorbed by the converter itself and not reach the sensitive silicon volume.

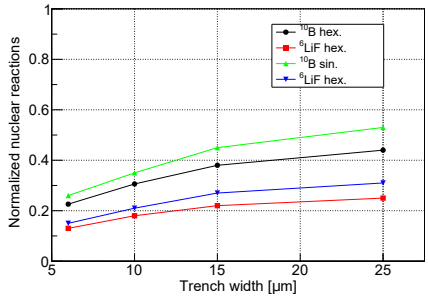

Figure 3.38: Normalized neutron capture reactions taking place inside ^{10}B or ^{6}LiF converter materials for hexagonal (hex) and sinusoidal (sin) designs - Thermal neutrons are perpendicular to the detector front-face surface and the converter density is 2.5 g/cm^3.

The detection efficiency depends also on the neutron path through the sensor. Three main layouts of neutron beam paths are considered in this study: (i) a front-face irradiation (Figure 3.39a), i.e. the detector and beam are in front of each other such that a mono-directional neutron beam points toward the upper-face of the detector; (ii) a spherical neutron source (Figure 3.39b), where the detector in placed inside; and (iii) irradiations under an angle (Figure 3.39c) where the detector is tilted for different angles along the X-axis. Notice that spherical beam irradiation does not exist other than inside a nuclear reactor, where the radiation damage inside

would destroy these detectors, but this beam configuration has been used in this work to compare the intrinsic detection efficiencies for different converter densities.

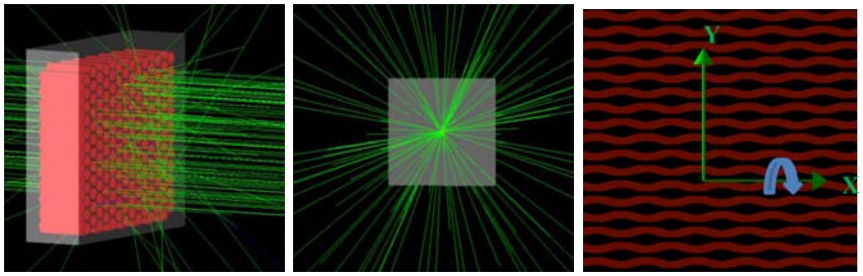

(a) **(b)** **(c)**

Figure 3.39: GEANT4 simulated layouts - (a) Hexagonal microstructured sensor irradiated by a front-face neutron beam. (b) Spherical neutron source (source of 30 cm diameter) around the detector. (c) Sinusoidal microstructure showing the rotation axis for irradiation under an angle.

The effective intrinsic efficiency is defined as:

$$\varepsilon = \frac{R_{det} \cdot A(\theta)}{Flux \cdot A_{\perp}} \tag{3.9}$$

where $A(\theta)$ is the projected detector area as a function of θ and $A_{\perp}$ is the projected detector area for the perpendicular irradiation case [49]. The effective intrinsic efficiency accounts for solid angles and area effects and is normalized to the initial irradiation orientation, the perpendicular case. The effective intrinsic efficiency and area correction factor are important considerations for detectors that are irradiated simultaneously from multiple directions or for detectors that may be turned through various angles during operation.

- *Incident neutron direction dependence*

Figure 3.40 and 3.41 show the effective intrinsic efficiency (Equation 3.9), as a function of the trench width, for the front-face neutron incident beam, for the neutron spherical irradiation, and for one representative

irradiation under an angle (45° along the X axis). The perforations are filled with ^{6}LiF in Figure 3.40 and with ^{10}B in Figure 3.41.

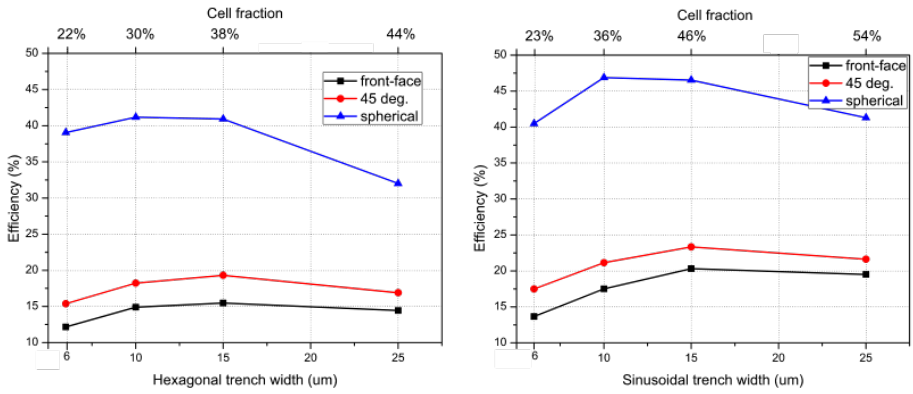

(a) **(b)**

Figure 3.40: Thermal neutron detection efficiency of ^{6}LiF versus the trench width - Efficiency of (a) hexagonal and (b) sinusoidal micro-channels trench width for different irradiation directions. Fixed parameters: ^{6}LiF density (2.5 g/cm^{3}) and trench depth (150 µm).

Figure 3.40 shows that (i) for the front-face irradiation case, the thermal neutron efficiency is the lowest since neutrons hit perpendicularly the detector and a considerable proportion of them do not interact with the converter material along their path; (ii) for the 45° irradiation case, the efficiency increases since the probability of neutron interaction with the converter along their path increases due to the angular effect. The maximum efficiency of 24% is reached for a 15 µm sinusoidal micro-channel width. Note that the hexagonal geometry entails a rotational symmetry which produces no change on efficiency if the 45° rotation is done along the X or Y axis. But the sinusoidal geometry does not have this symmetry and it should be rotated along the X-axis (Figure 3.39c) to increase the detection efficiency; (iii) for the spherical irradiation case, the highest efficiency is reached since most neutrons have the chance to become captured while passing through the converter material. A maximum efficiency of 47% is achieved for a 10 µm wide sinusoidal micro-channel.

In Figure 3.41, due to the low range of reaction products of ^{10}B (see Table 3.6), the maximum value of efficiency is shifted to smaller trench widths than those shown in Figure 3.40. The maximum thermal neutron detection efficiency is reached for a 6 µm trench width for all the irradiation cases; the highest efficiency (27%) is reached with spherical irradiation and for the sinusoidal design. Note also that the efficiencies fall sharply after reaching the maximum value. Only neutron capture reactions taking place close to the boundary between silicon and converter material contribute to the whole efficiency.

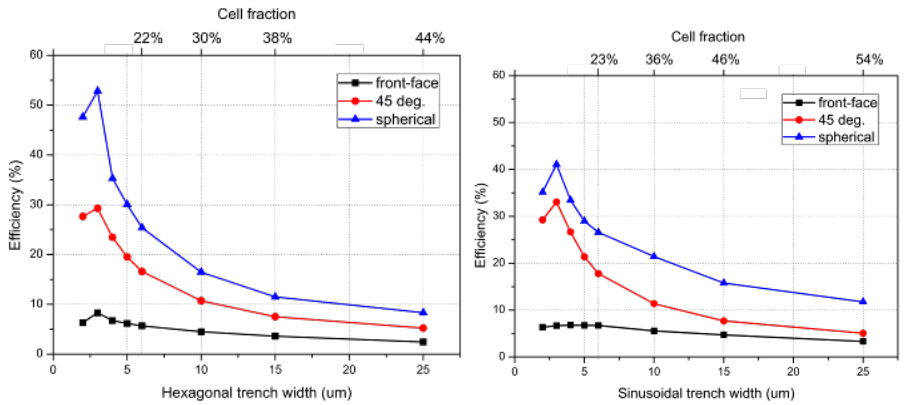

(a) **(b)**

Figure 3.41: Thermal neutron detection efficiency of ^{10}B versus the trench width - Efficiency of (a) hexagonal and (b) sinusoidal micro-channels trench width for different irradiation directions. ^{10}B density (2.5 g/cm^3) and trench depth (150 µm).

Although dimensions lower than 2.5 µm are difficult to obtain by lithography, and the converter filling of trenches smaller than 6 µm width is not viable through hand-packing, trench widths <6 µm have been simulated and included in Figure 3.41 to compare the similar behaviors of structures with ^{6}LiF and ^{10}B.

Figure 3.42 shows the thermal neutron effective intrinsic efficiency for the sinusoidal design for different irradiation angles. The microstructures

are filled with ^{10}B (Figure 3.42a) and ^{6}LiF (Figure 3.42b) neutron converter materials and the neutron beam (1x1cm^2 square homogeneous distribution) is rotated around the detector X-axis from front-face irradiation to 90°.

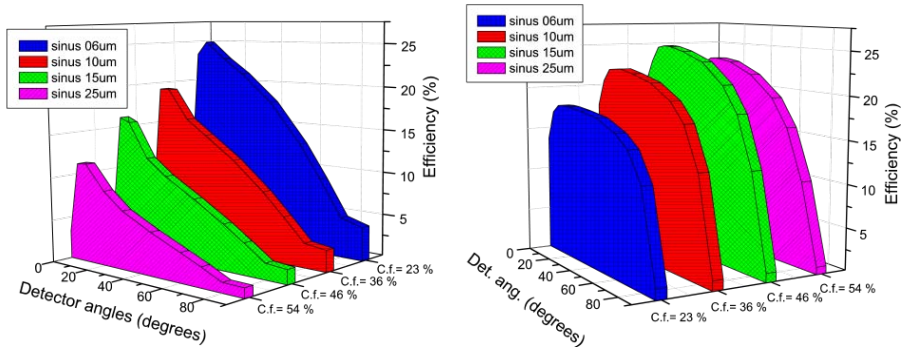

(a) **(b)**

Figure 3.42: Effective intrinsic efficiency for sinusoidal geometries as a function of the irradiation angle - (a) ^{10}B and (b) ^{6}LiF neutron converter materials with a density of 2.5 g/cm^3.

As the incident angle increases, the neutrons pass through progressively more material and have a higher chance of being absorbed. This effect causes a slight increase in the detector efficiency as the angle increases from 0° to 10°. But at larger angles this effect is eventually overcome by the fact that the projected area of the neutron beam to the detector is reduced by a $\cos(\theta)$ factor, being θ the detector rotation angle along X axis. It means that while the detector is rotating, a proportion of neutrons do not hit either converter material or silicon and the other neutron proportion passes through converter and silicon repeatedly until they are captured or escape the detector. Note that the efficiency remains more stable over a wide range of detector angles using ^{6}LiF converter instead of ^{10}B (from 10° to approximately 60°).

- *Density dependence*

Figures 3.43 and 3.44 show the simulated efficiency for thermal neutrons as a function of the ^{6}LiF and ^{10}B converter material density respectively for all fabricated geometries with 150 µm depth and for the spherical irradiation case. Spherical irradiation has been selected to avoid directional dependence of the beam, so the plotted values corresponds to the intrinsic efficiency. Figure 3.43 shows (i) that the maximum efficiency is reached for 2.5 g/cm^3 of ^{6}LiF for all cases since the thermal neutron mean path is shorter when the converter density increases (3.37), and (ii) the highest efficiency of 47% is achieved with a 10 µm sinusoidal micro-channel width. Note that the efficiency gain is lower as the density increases because of the range reduction of the reaction products through the converter material.

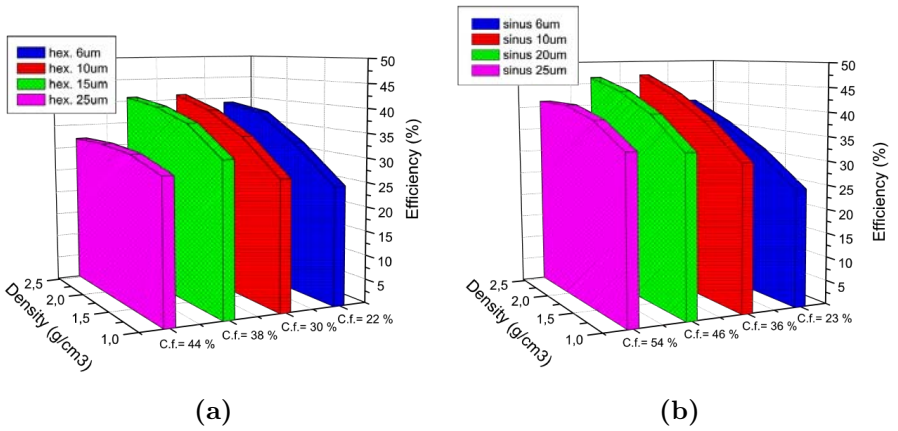

(a) **(b)**

Figure 3.43: Efficiency as a function of the ^{6}LiF density - (a) hexagonal and (b) sinusoidal fabricated geometries.

Figure 3.44 shows (i) that the maximum efficiency is reached for 1.0 g/cm^3 of ^{10}B for all the cases since the detection efficiency improves when the converter density decreases, and (ii) the highest efficiency of 48% is achieved with 150 µm sinusoidal micro-channel width.

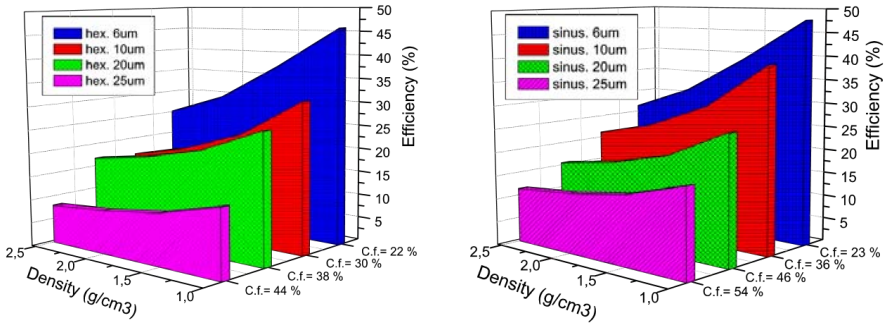

(a) **(b)**

Figure 3.44: Efficiency as a function of the ^{10}B density - (a) hexagonal and (b) sinusoidal fabricated geometries.

The opposite behavior shown in the thermal neutron efficiencies as a function of density for the two converters is mainly due to the differences in range of their reaction products (3.6). As shown previously, the lower is the converter density, the higher is the range of the charged particles, but at the same time there is a lower number of ^{10}B or ^{6}LiF atoms per unit volume. Increasing the density of ^{6}LiF has a positive effect on the efficiency because most reaction products may reach the silicon sensitive volume, but using the ^{10}B converter material an increase of the density means fewer reaction products hitting the sensitive volume due their low range.

- *Pulse height spectra of deposited energy*

The pulse height spectra provide the energy distribution that the reaction products of the neutron capture deposit in the silicon sensitive volume. As already mentioned, these reaction products have to go through the converter and dead layers before reaching the detector silicon sensitive volume, and therefore they lose part of their energy when they go through these layers. The amount of energy deposited in the detector depends on the depth where the neutron capture takes place inside the converter and

the angle under which the reaction product is ejected towards the sensitive volume. For the ^{6}LiF reaction products another dependence may exists because of their high range; if the silicon sensitive volume is not thick enough part of the signal could be lost.

Figure 3.45a and 3.45b show the features of the simulated spectra for hexagonal and sinusoidal geometries and for ^{10}B and ^{6}LiF neutron converter materials.

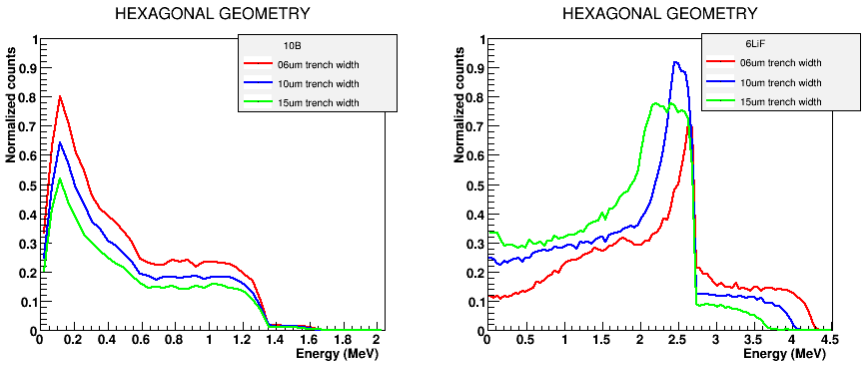

(a)

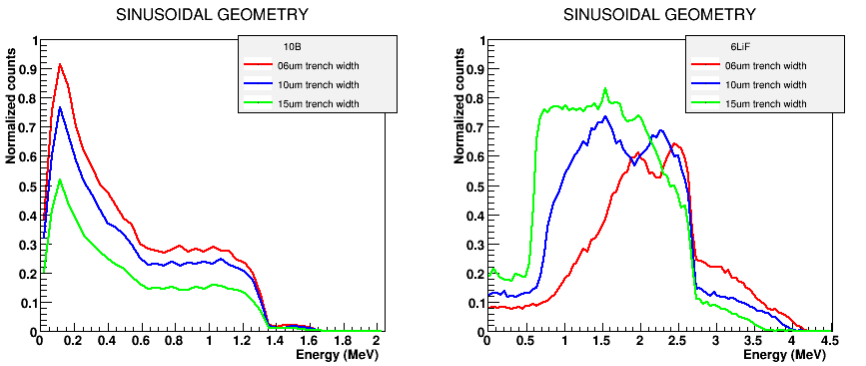

(b)

Figure 3.45: Energy spectra of the neutron capture ^{10}B(n,^{4}He)^{7}Li and ^{6}Li(n,t)^{4}He reaction products - (a) hexagonal and (b) sinusoidal microstructures. In both cases the simulated trench widths are 6, 10 and 15 µm, there is front-face irradiation and the converter material density is 2.5 g/cm^{3}.

The spectral distribution for both hexagonal and sinusoidal designs filled with ^{10}B neutron converter is concentrated in the low energy channels due to the short range of the ^{10}B(n,^{4}He)^{7}Li reactions products. By contrast, the spectral distribution of the designs that use ^{6}LiF converter are shifted to the high energy channels because of the large range of the ^{6}Li(n,t)^{4}He reaction products. In this last case, Figure 3.45 (right) shows that the wider the trench, the broader the alpha-peak to low energy regions.

Figure 3.45 (left) shows two distinguishable slopes whose endings correspond to the ^{10}B(n,^{4}He)^{7}Li reaction product energies, i.e. 1.47 MeV and 0.84 MeV (alpha and lithium particles respectively), minus those energies that these ions lose within the 0.5 µm dead layer thick. Figure 3.45 (right) shows a different behavior for the ^{6}Li(n,t)^{4}He case: the spectra has a pronounced drop at the triton energy (2.72 MeV) region, but the 2.05 MeV alpha particle contribution is not clearly observed since in most cases both particles reach the sensitive volume contributing to the total pulse height distribution at the same time. The difference in the spectra for the hexagonal and sinusoidal geometries is more pronounced in the case of ^{6}LiF due to the longer range of its reaction products, as they are able to interact for a longer distance with what surrounds the production point and deposit a different energy according to the geometry found.

It is important to observe the influence of the 0.5 µm silicon dead layer in the energy deposition of the low energy reaction products of ^{10}B. Figure 3.46 shows the simulated spectra for the sinusoidal geometry with 6 µm trench width with and without the dead layer inside the trenches. Figure 3.46b shows that if there is no dead layer, the peaks that correspond to the 0.84 MeV and 1.47 MeV energies of each reaction products are more pronounced.

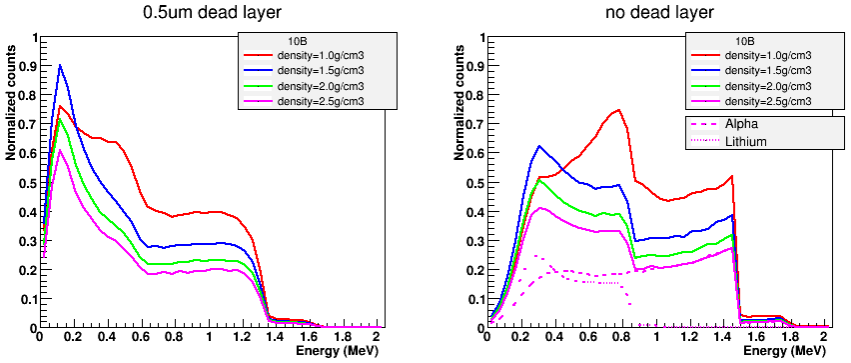

(a) (b)

Figure 3.46: Spectrum of energy deposited by reaction ions in 6 µm geometries filled with ^{10}B - Trenches surrounded by (a) 0.5 µm silicon dead layer and (b) no dead layer surrounding the trenches. Spherical irradiation and converter density of 2.5 g/cm^3.

Figure 3.47 shows the contribution of each of ^{10}B(n,^{4}He)^{7}Li and ^{6}Li(n,t)^{4}He reaction products to the total spectrum. These plots have been obtained running three separate simulations and tracking only one of the reaction products at a time. The total spectrum, where the total energy deposited in the silicon after each neutron capture is recorded, is also shown. Due to the possibility of both reaction products reaching the silicon sensitive volume at the same time (i) counts at higher energy are present in total spectrum and, (ii) the sum of the number of counts of individual spectra is higher than the number of counts in the total spectrum. It should be noticed that due to differences in range of the reaction products between ^{6}LiF and ^{10}B, these two effects are much more predominant in the ^{6}LiF than in ^{10}B converter material.

Finally, it is worth observing that the effect of the Lower Level Discriminator (LLD) in the efficiency of a neutron detector will be more pronounced in the case of detectors based on ^{10}B because a higher number of counts are placed in the low energy range of the spectrum.

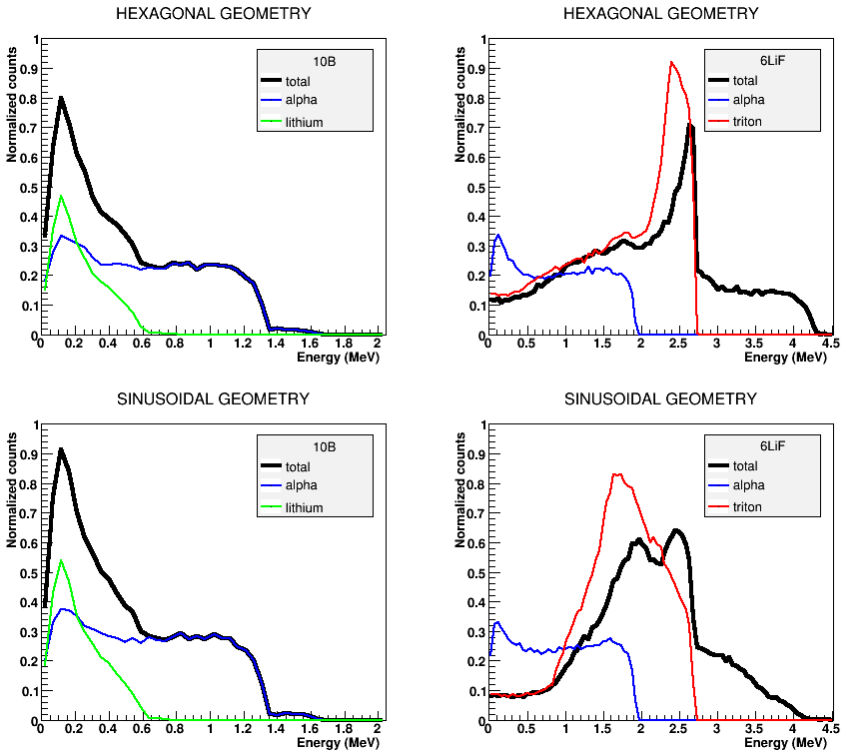

Figure 3.47: Spectrum of energy deposited by reaction ions in 6 µm geometries filled with ^{10}B and ^{6}LiF - Front-face irradiation and converter density of 2.5 g/cm^3.

3.5.4.2 Simulations of the second batch

For the second fabrication batch, the aim of the simulations was to study the optimum perforated pattern and its dimensions to achieve an improvement of the intrinsic thermal neutron detection efficiency. As already mentioned, the simulations were done considering only ^{6}LiF as neutron converter material.

Thanks to the experimental results of the first fabrication batch, the following considerations were the starting point of the simulations: i) sinusoidal perforations, due to their directionality, provide the fastest and

easiest hand-packing filling process, ii) trench widths in the range of 15 µm - 20 µm are the most appropriate dimensions for the hand-packing trench filling technique used in this work, iii) silicon walls narrower than 10 µm, even though they can be successfully fabricated, are not recommended because they can be be broken while applying pressure when filling. Taking into account these points, the modeled detector was composed by connecting two straight patterns, where one was tilted an angle θ respect to the other, to create the sinus-like pattern. Figure 3.48 shows the main sketch of the simulated unit cell with the variables to be optimized. The first straight pattern (represented as blue) was simulated independently as a simple straight trenches and then, using the optimum results, the complete unit cell was simulated with different values of: θ, trench depth and density of converter.

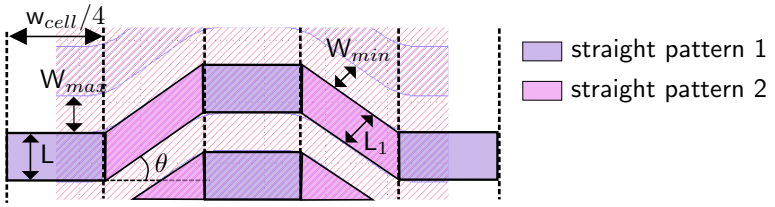

Figure 3.48: Simulation sketch of a complete unit cell - The starting point of the simulation study was: trench width (L) fixed to 20 µm and W_{cell} fixed to 160 µm.

Figure 3.49a shows the efficiency of straight perforations for different values of the silicon wall. The trench with (L) and the ^{6}LiF density were fixed to 20 µm and 2.5 g/cm^3 respectively, however in order to compare results a simulation of a trench width of 15 µm is also depicted. From this figure it can be seen that the efficiency tends to increase as the ratio ($L/(L+W)$) increases, therefore for this simulation the maximum efficiency is achieved for 15 µm of silicon wall. A complete simulation study of straight trenches can be found in [27, 50].

The dimensions L_1 and W_{min} of the second straight pattern were calculated for different tilt angles (θ) considering the optimum dimensions

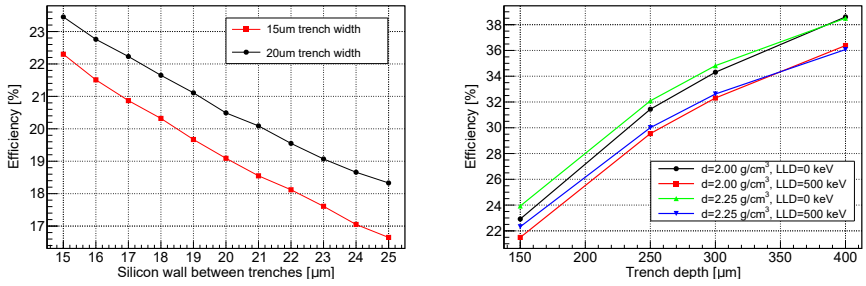

(a) **(b)**

Figure 3.49: (a) Simulated thermal neutron detection efficiency of straight patterns with 15 µm or 20 µm trench width for different values of silicon wall (W_{max}). The converter material density is 2.5 g/cm^3 and the trench depth is 150 µm. (b) Intrinsic thermal neutron detection efficiency of the complete final geometry as a function of trench depth. Two neutron converter densities have been simulated and the efficiency for each case is shown at a threshold value of 0 and 500 keV. In all simulations the unit cell only has been irradiated with a front-face beam.

of the first straight pattern (20 µm trench width and 15 µm of silicon wall). The calculations were made with Equation 3.10 obtained from simple trigonometry:

$$\sin(90° - \theta) = L_1/L = W_{min}/W_{max} \tag{3.10}$$

Table 3.7 summarizes the obtained dimensions for the second straight patterns and its intrinsic efficiency. Notice that smaller angles than 20° have not been studied in order to eliminate directions in which neutrons stream between perforations avoiding the neutron converter material [51] and, higher angles than 45° neither to avoid the creation of sharp edges in the pattern.

The best configuration for the straight pattern number two is a trench width of 14.14 µm and a silicon wall of 10.60 µm. But, as the efficiency does not have a significant change while modifying the tilt angle, the chosen configuration was the 16.38 µm trench width and 12.23 µm silicon wall in

Table 3.7: Simulated thermal neutron detection efficiency of straight patterns with different trench (L_1) and silicon wall (W_{min}) widths - The converter density is 2.5 g/cm^3, the trench depth is 150 µm and the manufactured configuration is depicted in italics.

Straight pattern 1		**Straight pattern 2**			**Efficiency**
L (µm)	**W**$_{max}$ (µm)	**angle** (°)	**L**$_1$ (µm)	**W**$_{min}$ (µm)	
20	15	45	14.14	10.60	25.88 %
		40	15.32	11.49	25.38 %
		35	*16.38*	*12.23*	*25.01* %
		30	17.32	12.99	24.57 %
		25	18.12	13.59	24.21 %
		20	18.79	14.09	23.95 %

order to achieve better mechanical strength. Other reason to select this configuration is that a 12 µm silicon wall width was already successfully manufactured in the first fabrication batch.

A further simulation of the chosen configuration was realized to study the influence of the trench depth. Figure 3.49b shows the intrinsic efficiency as a function of the trench depth for a converter densities of 2.0 g/cm^3 and 2.25 g/cm^3 and for two threshold values of 0 and 500 keV. The efficiency increases as the trench depth becomes higher due to neutrons passing trough more thickness of converter material. This efficiency gain becomes less pronounced as the trench depth increases till reaching a maximum value around 500 µm depth. Deeper trenches will not result in much higher efficiencies and instead they will be unfavorable because of the increased gamma-ray interactions. In figure 3.49b it is also seen that for ^{6}LiF the efficiency increases as the converter density increases.

A final simulation of the selected geometry was performed to get the energy distribution that the reaction products deposit in the silicon sensi-

tive volume. Figure 3.50a shows the total contribution of energy deposit (black line) together with the contributions to the total spectrum of each reaction product (blue and green line). As already explained in previous simulations, counts at higher energy than the most energetic particle are present in the total spectrum due to the possibility of both reaction products reaching the silicon sensitive volume at the same time. The tritium spectrum is the main contribution to the total spectrum because of its high range in ^{6}LiF (34.2 µm), almost in all produced reactions it reaches the silicon sensitive volume.

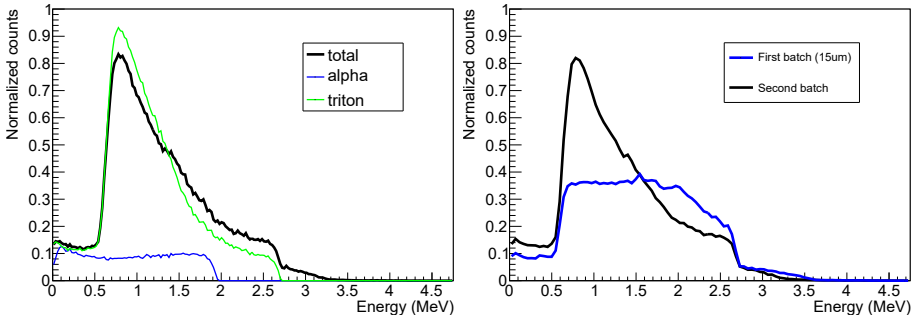

(a) **(b)**

Figure 3.50: Spectrum of energy deposited by reaction products from the ^{6}LiF(n,t)^{4}He reaction - Front-face irradiation and ^{6}LiF density of 2.5 g/cm^{3}. a) Total, alpha and tritium contributions in a second batch sensor with 250 µm depth. b) Comparison spectrum of a first batch sensor (15 µm sinusoidal) and second batch sensor (both of 150 µm depth and filled with ^{6}LiF).

Figure 3.50b shows a comparison between the total energy distribution of a 15 µm sinusoidal sensor of the first fabrication batch and a sensor of the second fabricated batch (both of 150 µm depth). In the first batch distribution slightly more counts are observed from 1.7 MeV to 2.7 MeV due to the thicker sensitive silicon region between trenches, however higher detection efficiency is achieved in the sensors from the second batch because they show a notable increase in counts from 0.5 MeV to 1.7 MeV. This efficiency improvement is produced because, as already said, the sec-

ond design was specifically optimized for ^{6}LiF as converter material while the first batch was based on study of trenches filled with boron-based converter materials [40].

3.6 Experimental validation with neutrons

This section covers the experimental results obtained at the Portuguese Research Reactor (RPI), located at the Instituto Tecnologico e Nuclear (ITN) facilities in Lisbon, with the U3DTHIN and MS detectors covered and filled respectively, with different neutron converter materials. GEANT4 simulations to validate the experimental results are also presented.

3.6.1 The Portuguese Research Reactor (RPI)

The RPI, a 1 MW pool-type reactor (Figure 3.51a) was used to assess the efficiency of neutron detectors with a well-known neutron beam [52, 53]. Two irradiation facilities (Figure 3.51b and 3.51c) are available in the reactor, one delivering a 5 cm diameter well-collimated thermal neutron beam (thermal Maxwellian (0.025 eV)) and the other a 15 cm diameter fast neutron beam (E>1 MeV).

(a) **(b)** **(c)**

Figure 3.51: Images of the Portuguese Research Reactor - (a) Portuguese Research Reactor core operation at 1 MW power, (b) thermal neutron and (c) fast neutron beam area.

Table 3.8 shows the neutron fluxes for both areas as well as the linear dependence of these with the reactor power. The thermal neutron fluxes were obtained in front of the beam shutter using activation foils[1]. In particular, gold foils (bare and cadmium-covered) were used for thermal and epithermal neutron fluxes while indium, nickel and aluminum foils were used to characterize the fast region of the spectrum [54].

Table 3.8: Neutron flux and gamma field in the ITN nuclear reactor

Reactor power (kW)	Flux thermal neutron port ($n/cm^2/s$)	Gamma dose rate thermal neutron port ($\mu Gy/s$)	Flux in fast (E>1 MeV) neutron port ($n/cm^2/s$)
1000	$(5.0 \pm 0.2) \cdot 10^5$	5.6 ± 0.4	$8 \cdot 10^7$
100	$(5.0 \pm 0.2) \cdot 10^4$	$(5.6 \pm 0.4) \cdot 10^{-1}$	$8 \cdot 10^6$
10	5000 ± 200	$(5.6 \pm 0.4) \cdot 10^{-2}$	$8 \cdot 10^5$
1	500 ± 20	$(5.6 \pm 0.4) \cdot 10^{-3}$	$8 \cdot 10^4$
0.1	50 ± 2	$(5.6 \pm 0.4) \cdot 10^{-4}$	$8 \cdot 10^3$

Moreover, additional flux measurements were done at different irradiation positions with an ^{235}U fission counter (Figure 3.52) showing good agreement with foil measurements. The inherent gamma field present in neutron fields has to be also taken into account to fix the LLD setting and to obtain reliable neutron efficiencies (the gamma values were given by the RPI personnel).

[1] Activation is the conversion of a stable isotope into a radionuclide by the absorption of a neutron and is used to produce gamma rays and beta particles, which are proportional to the neutron flux.

(a) (b)

Figure 3.52: Thermal neutron flux measurements with an ^{235}U fission counter - Measurements (a) at the beam exit and (b) 18 cm away of the beam exit. The filling gas is argon at 1 atmosphere and the amount of ^{235}U is 0.23 mg).

3.6.2 U3DTHIN detectors

The U3DTHIN sensors fabricated at IMB-CNM were tested in both irradiation facilities of the Portuguese Research Reactor. For thermal neutron tests the sensors were covered with boron-based converter materials while for the fast neutron beam a polyethylene sheet was used.

3.6.2.1 Thermal neutron tests

U3DTHIN detectors covered with boron-based converter materials (2.7 µm of $^{10}B_4C$ or BE10 screen) were tested in the thermal neutron irradiation facility at the RPI. Figure 3.53 displays the experimental setup in the RPI nuclear reactor: the aluminum box (Faraday cage to reduce the noise level contribution and to keep the detectors in the dark) containing the detectors was located just in front of the beam shutter with the coated side of the sensor facing the incoming beam. The data acquisition system was placed at 3 meters, outside the biological shielding. Then a set of measurements with different conditions was carried out.

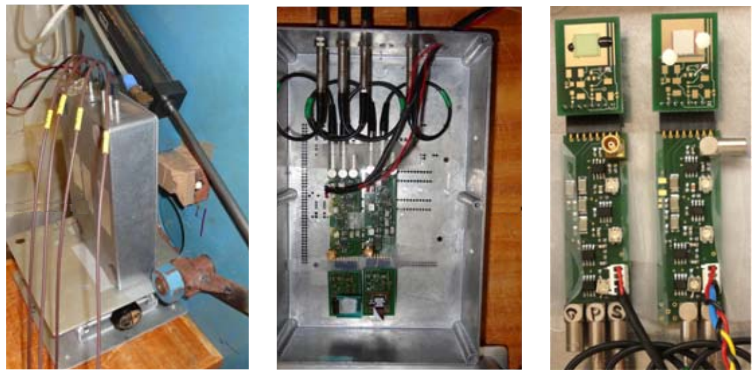

Figure 3.53: Experimental setup in the Portuguese Research Reactor - (a) Setup placed in front of the thermal neutron beam shutter, with the detectors in the center of the beam. (b) Aluminum box containing a U3DTHIN detector with $^{10}B_4C$ converter coating (adapted detector), a U3DTHIN without converter coating (bare detector), and their respective front-end readout electronics. (c) Image of the bare and covered U3DTHIN detectors connected to their printed circuit boards (PCB)

It is also important to remark that the leakage current of the sensors was registered at the beginning and end of each measurement, and that this current did not increase during the 10 min acquisitions. This is an important parameter to ensure the stability of the detector response in operation for long periods of time.

Two detectors were always tested at the same time: one U3DTHIN detector with a converter layer (adapted detector) and another one, identical to the first, without any converter (bare detector). The difference in counts between them should be due to the charged particles produced by the capture of neutrons within the converter. The bare detector is also used to measure the photon and other background contributions.

Prior to the thermal neutron beam tests, noise level measurements were realized in the experimental area for all detectors under study to select the less noisy ones. In a semiconductor radiation detector there is always an electronic noise caused by several external causes, such as pick-up noise

from the omnipresent electromagnetic radiation or noise from the digital part of the electronics, and the internal sensor noise that depends on the capacitance and the current. Figure 3.54a shows the counts registered by the bare and the $^{10}B_4C$ U3DTHIN detectors biased at 30 V in the absence of the thermal neutron beam.

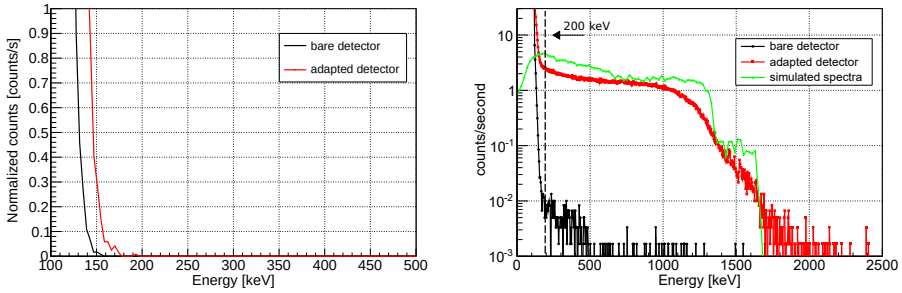

(a) **(b)**

Figure 3.54: (a) Response spectrum of U3DTHIN detectors in the absence of radiation. Counts are due to the electronic noise. (b) Energy calibrated spectra of the bare and $^{10}B_4C$ neutron detectors at 30 V bias voltage irradiated with the thermal neutron beam. The simulated spectra of the U3DTHIN detector coated with a 2.75 µm B_4C layer (d=2.25 µm) is also depicted (the simulated counts/second have been normalized to the results obtained in the experimental test).

All tested sensors had a noise level in the range of 150 -200 keV. However, this noise might be higher in other environments so the neutron test results will be given also in therms of different low level discrimination (LLD) settings. The LLD can also be tuned beyond the noise level to discard low energy counts from the gamma radiation background. One has to take into account that the detection efficiency decreases for increasing LLD as real radiation signals below the LLD are discarded as noise. The energy calibration of all spectra was performed through a test capacitor as explained in Appendix C.

Figure 3.54b shows the first measurements carried out at a reactor power of 90 kW with the $^{10}B_4C$ adapted and bare detectors. The ther-

mal neutron flux at this power was $(4.5\pm0.2)\cdot10^4$ n/cm^2/s. Since the amount of deposited energy in the detector sensitive volume (space charge region) depends on the depth where the capture reaction takes place in the converter, the pulse height distribution is a continuous spectrum. The spectrum endpoint of the adapted detector is located at an energy of approximately 1700 keV that corresponds to the maximum energy of the reaction products of the (n+^{10}B) reaction, 1780 keV, minus the energy lost in the entrance window. The simulated spectrum normalized to the experimental results is also depicted to illustrate its components. The two abrupt drops of counts per second in the simulated spectra, around 1350 keV and 1650 keV, correspond to the final range of the alpha particles. The main differences from experimental and simulated spectra come from: i) absence of noise in the simulation (counts below 200 keV), ii) absence of metal lines and desuniformities within the conversion layer in the simulations and iii) in the simulation setup, only alpha and lithium particles are considered to deposit energy in the silicon detector then, no counts more energetic than the ones produced by alpha particles are observed.

The background counts in the bare detector of Figure 3.54b, approximately two orders of magnitude lower than the neutron counts in the adapted detector, come mainly from the reactor gamma field but they may also come from: i) the natural γ-ray background, ii) photons produced from (n,γ) reactions in the materials around the experimental area, iii) energy deposited in the silicon volume by n-Si nuclear interactions. From the measurement, the gamma/neutron count rate is 1/920 for a LLD setting of 200 keV, or a photon response of (0.8 ± 0.1) counts/μGy. These values are calculated in the worst case assumption where all counts come from the reactor gamma field and not from these other contributions. As previously said, the insensitivity to gamma radiation is essential for good neutron detectors as the neutron radiation is typically accompanied by a gamma emission.

The dependency of the count rate in the adapted and bare detectors with the LLD setting is shown in Figure 3.55a where it can be seen that the

background count rate decreases more rapidly with increasing LLD than the neutron rate due to the fact that the background counts are mainly on the low energy part of the spectrum. For LLD values higher than 500 keV the background contribution is practically eliminated as can be seen in Figure 3.54b and further LLD increments only reduce the neutron detection efficiency but do not improve the signal/background ratio.

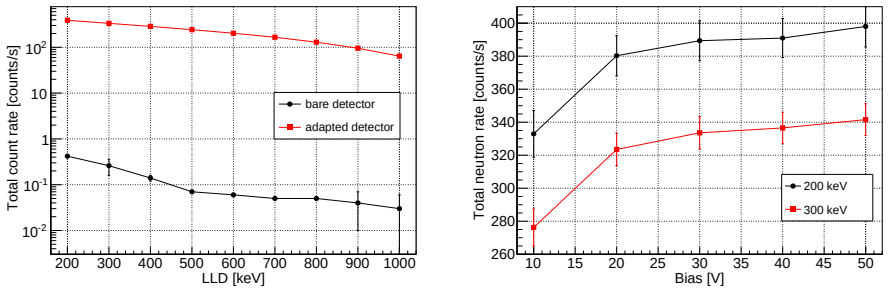

(a) **(b)**

Figure 3.55: (a) Total count rate of the U3DTHIN detectors. The bare and $^{10}B_4C$ adapted detectors at V_{bias} =30 V. (b) Thermal neutron count rate as a function of the detector operating voltage and LLD. The total neutron count rate is defined as the counts in the adapted detector minus the counts in the bare detector

From the capacitance versus voltage measures (Fig 3.19b) a fully depleted U3DTHIN sensor is achieved at 30 V but, to study the influence of the bias voltage in the neutron count rate, a series of data acquisitions were performed for different bias voltages at the same reactor power (90 kW). As shown in 3.55b, the neutron detection rate increases in the bias range 10-30 V and is stable for voltages >30 V. This results confirms that at low voltages, the presence of the partially depleted layer at the Si surface (due to negative charge located at the Si/SiO_2 interface (section 3.4.2)) does not allow the complete collection of the low-range reaction products from the nuclear reaction and reduces the efficiency. Another representation of this figure is shown in Figure 3.56b where the neutron rate has been

replaced by the thermal neutron detection intrinsic efficiency.

The intrinsic thermal neutron detection efficiency of the sensor calculated with Equation 3.8 with $R_{det} = R_{adapted} - R_{bare}$ is plotted in Figure 3.56. The error is calculated assuming a ±20 keV error in the energy calibration of the spectra and a 5% error in the determination of the radiation fluence.

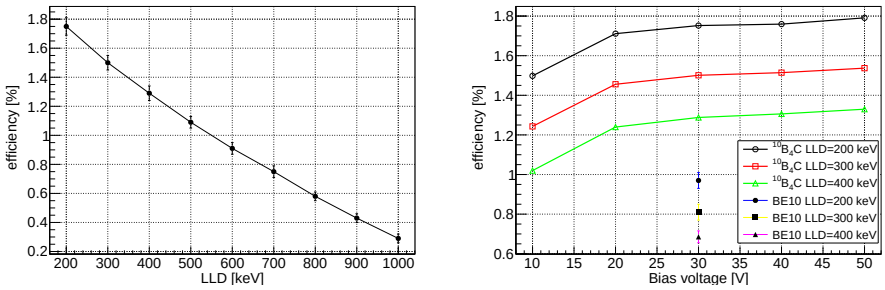

(a) **(b)**

Figure 3.56: (a) Thermal neutron detection intrinsic efficiency of the $^{10}B_4C$ coated U3DTHIN as a function of the LLD and with V_{bias}=30 V. (b) Thermal neutron detection intrinsic efficiency of the $^{10}B_4C$ and the BE10 coated U3DTHIN as a function of bias voltage (only 30 V bias voltage measurements were realized for the U3DTHIN covered by the BE10 screen).

Figure 3.56a shows the neutron detection efficiency behavior of the $^{10}B_4C$ coated U3DTHIN while the LLD value is increased. As already mentioned, this efficiency reduction is due to more neutron counts rejected as noise while increasing the LLD from 200 keV to 1000 keV. The measured intrinsic efficiency of the ultra-thin 3D detector with 2.7 µm $^{10}B_4C$ is (1.75 ± 0.06)% for a bias voltage of 30 V and LLD=200 keV. This efficiency result is consistent with the maximum simulated value of 2.81% (Figure 3.21b) with the difference coming from: i) slight differences of the deposited $^{10}B_4C$ converter thickness through the sensor surface (see Figure 3.23), ii) probable lower density of the $^{10}B_4C$ coating with respect to the values used in the simulations and iii) entrance windows >400 nm

in places.

Figure 3.56b compares the efficiency of the U3DTHIN sensors covered with the $^{10}B_4C$ or with the BE10 screen converter materials for a 30 V bias voltage. For a LLD=200 keV the efficiency of the BE10 screen is only $(0.94 \pm 0.04)\%$, approximately half of the efficiency reached with the $^{10}B_4C$ converter layer. This is because the BE10 screen is not optimized for maximum efficiency neutron detection; the converter layer is 40 µm thick so, due to low range of reaction products in the $^{10}B_4C$/glue mixture (see Figure 3.57a) only reactions taking place close to the Si/converter interface (in the last 10 µm from the interface) contribute to the efficiency. Moreover, as the BE10 screen is not glued to the sensor, an air gap could exist between them contributing as an extra dead layer although care was taken to avoid this problem.

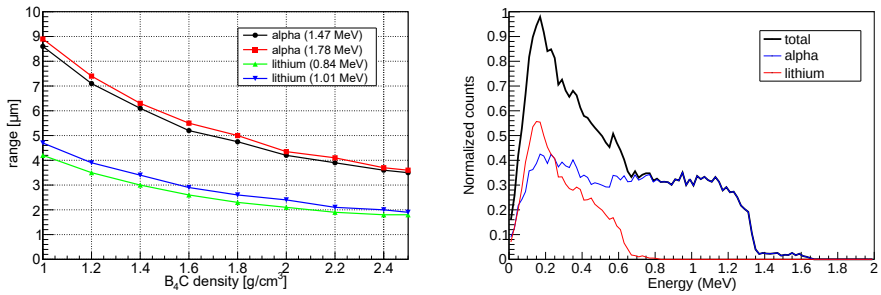

(a) **(b)**

Figure 3.57: (a) Range in B_4C of alpha particles and lithiums which are products of neutron capture on ^{10}B. Curves are calculated for different densities of B_4C. (b) Simulated spectrum of energy deposited by reaction ions in the U3DTHIN covered with a 2.75 µm layer of B_4C (density=2.25 g/cm^3).

Figure 3.57b shows the contribution of each reaction product to the total simulated spectrum. It can be seen that the lithium particles only contribute to the first part of the spectrum, due to their low energy and range, while the alpha particles contribute to the whole range and completely define the ending of the spectrum. These plots have been obtained

running two separate simulations and tracking only one of the reaction products at a time. The total spectrum, where the total energy deposited in the silicon after each neutron capture is recorded, is also shown.

To verify that the previous results, realized with 90 kW reactor power, were not affected by pile-up and to find the maximum count rate supported by the detection system, different data acquisitions were performed at varying reactor powers (Figure 3.58). All these measurements were done with the $^{10}B_4C$ coated U3DTHIN sensor biased at 30 V.

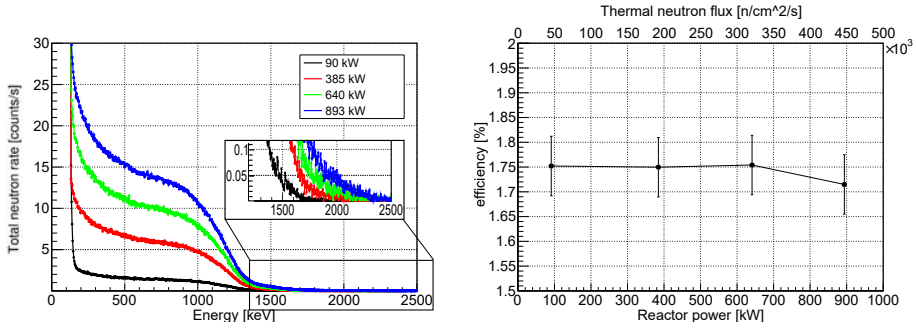

(a) **(b)**

Figure 3.58: (a) Energy calibrated spectra and (b) thermal neutron detection intrinsic efficiency for different values of reactor power. Measurement done with the $^{10}B_4C$ coated U3DTHIN sensor biased at 30 V.

Figure 3.58 shows the spectra and the efficiency obtained for different reactor powers. The response of the detection system is lineal, i.e. the total neutron rate increases linearly with the reactor power and there is not a decrease in the calculated efficiency due to signal saturation at least up to a power 640 kW, corresponding to an incident thermal neutron rate of $3.2 \cdot 10^5 n/cm^2/s$ or a neutron count rate of (270 ± 86) counts per second. At a reactor power of 893 kW there is a small counts loss of only 2%, within the experimental error, that could be attributed to signal pile-up in the detector readout. This light pile-up effect is also observed in the zoomed part of Figure 3.58a where few counts located at higher energy than 1780 keV are present.

3.6.2.2 Fast neutron tests

The U3DTHIN fast neutron detector (sensor with a polyethylene sheet (Figure 3.24b)) was located in the fast neutron port of the RPI in order to obtain the detection efficiency for fast neutrons (E>1 MeV). The fast neutron spectrum delivered in the irradiation point was in the interval of 1 MeV - 10 MeV approximately [52]. Geant4 simulations were also realized for this irradiation setup. The simulated incident neutron fluence spectrum was obtained from [52] and the polyethylene (C_2H_4) sheet was simulated with a density of 0.94 g/cm^3. All measurement were done at at 30 V reverse bias.

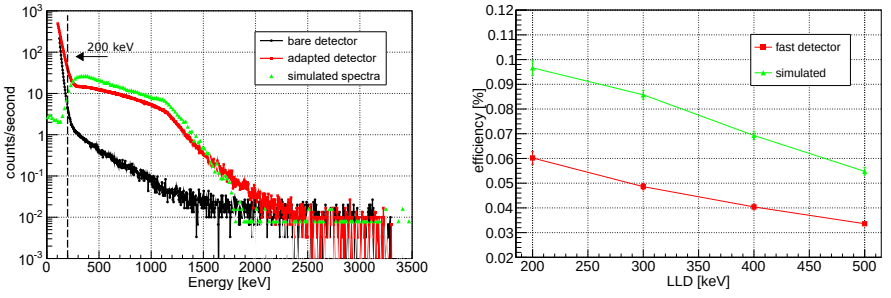

(a) **(b)**

Figure 3.59: (a) Response spectra to the fast neutron beam of the fast neutron and reference detectors biased at 30 V for a reactor power of 100 kW. The simulated curve has been normalized to the experimental results. (b) Fast neutron detection efficiency as a function of the LLD.

Figure 3.59a shows the fast neutron and reference detector responses measured for a reactor power of 100 kW. The normalized simulated curve is also depicted in the figure. The count rate in the bare detector is higher that the obtained in the thermal port due to the higher gamma field in the fast neutron port and due to the contribution of neutron interactions with the silicon nuclei, relevant at high neutron energies. Furthermore in fast neutron tests there are counts in a wider range of energies because the protons ejected from the polyethylene can have any energy up to the

maximum incident neutron energy.

Experimental and simulation results exhibit good agreement between 200 keV and 1750 keV. Differences below 200 keV are due to noise contributions not present in simulations and above 1750 keV due to gamma interactions with silicon which have not taken into account into the simulation setup. The response of a bare detector against the neutron spectrum was also simulated showing an interaction probability of fast neutrons with the silicon nuclei of only $4.28 \cdot 10^{-4}$% for the 20 µm silicon thick sensor.

Figure 3.59b shows the dependence of the efficiency on the LLD setting for both experimental and simulated cases. The experimental efficiency has been calculated using Equation 3.8 and considering a total neutron flux of $8 \cdot 10^6$ n/cm^2/s. For an LLD=200 keV, the obtained efficiency is $(6.0 \pm 0.3) \cdot 10^{-2}$ %. This result is consistent with the simulated efficiency achieved, $(9.66 \pm 0.03) \cdot 10^{-2}$ %, with the differences caused mainly by the simulated neutron spectrum, which is slightly different from the real one[1].

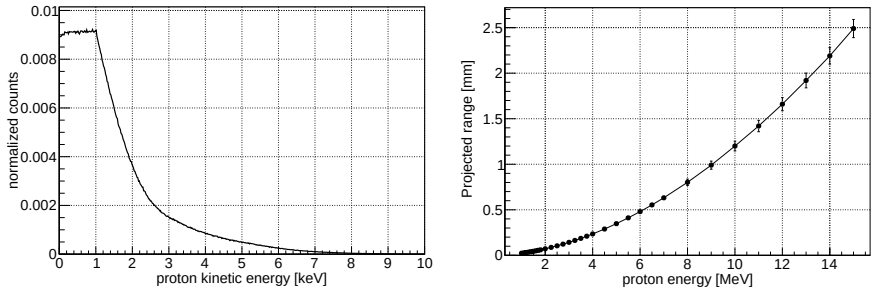

Figure 3.60: (a) Kinetic energy distribution of the recoil protons created inside the 3 mm thick polyethylene layer. (b) Projected range of protons into polyethylene.

Figure 3.60a shows the GEANT4 simulated results of the kinetic energy distribution of the recoil protons inside the polyethylene. From that

[1]The simulated neutron spectrum, obtained from reference [52], is calculated at a different point from where the U3DTHIN measurements were done.

simulation it was calculated that only ∼5.5% of the total incident neutrons hitting the 3 mm thick polyethylene layer created a recoil proton. Figure 3.60b shows, for the energy range of the recoil protons, their projected range inside the polyethylene. One of the main reasons for the low efficiency value achieved can be deduced from these results: most protons are created with a kinetic energy in the range 0 - 1 MeV and, accordingly to Figure 3.60b, their range in the polyethylene is in the order of 20 µm. This low range makes most of the protons not able to reach the silicon sensitive volume.

3.6.3 Microstructured detectors

Microstructured detectors from the first fabrication batch and filled with ^{10}B and ^{6}LiF were tested in the thermal neutron irradiation facility at the RPI.

Figure 3.61 shows the noise measurements for four microstructured detectors of the first fabrication batch. All tested sensors, independently of the trench width or the etched pattern, had a noise level in the range of 450 - 500 keV.

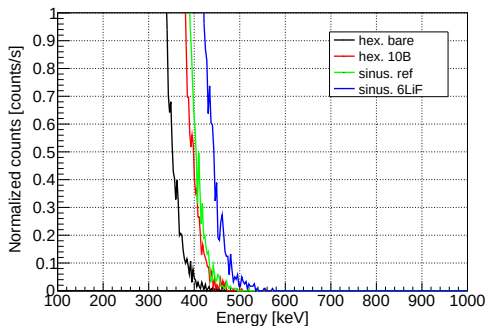

Figure 3.61: Response spectrum of MS detectors in the absence of radiation - counts are due to the electronic noise) with detectors biased at 3 V.

Due to these noise level values the radiation tests were mainly focused

on microstructured detectors filled with ^{6}LiF instead of ^{10}B because, as seen in the simulated energy spectrum of Figure 3.45, most counts of ^{10}B filled detectors are located in the low energy region (<600 keV). Therefore, with an LLD of 450 keV (LLD value for microstructured detectors) nearly all counts will be lost as noise and a low efficiency value will be achieved. Simulations of ^{10}B filled microstructured detectors (15 µm trench width) with an LLD value of 450 keV show efficiencies of only 0.98% for a converter density of 2.5 g/cm^3 and 1.64% for 1.5 g/cm^3.

For microstructured sensors filled with ^{6}LiF, thermal neutron tests at different irradiation angles were performed to study the angular dependence of the intrinsic detection efficiency. The setup of these measurements is shown in Figure 3.62. The sensors were placed 18 cm away from the beam exit in all cases and then were rotated about the azimuthal axis from 0° through 180° in 45° increments.

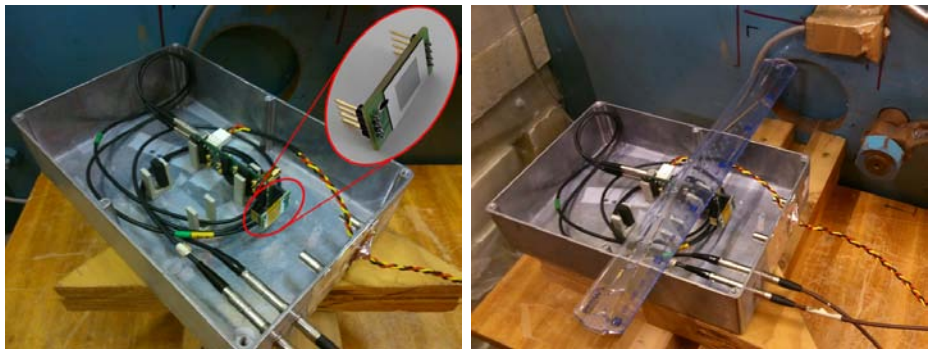

(a) **(b)**

Figure 3.62: Experimental setup in the Portuguese Research Reactor for irradiation at different angles - All measurements were done with detectors placed 18 cm away from the beam exit. (a) Back 45° and (b) 90°. The printed circuit board (PCB) with a mounted sensor is also depicted in figure (a).

Figure 3.63a shows the response of a ^{6}LiF-based sinusoidal detector with 25 µm microstructures to the thermal neutron beam, at a reactor power of 100 kW and 3 V bias voltage, for different irradiation angles.

The shape of these distributions does not depend on the irradiation angle because all spectra are created from the same reaction products (2.05 MeV alpha and 2.72 MeV triton particles). Due to the sensor design and the range of the ^{6}LiF reaction products, valleys in the spectra are observed around 600 keV, allowing the LLD to be set at high values without eliminating many of the neutron counts.

Counts more energetic than 2.72 MeV (the maximum energy of ^{3}H) are registered in Figure 3.63a because for a single event, both particles can reach and leave energy in the silicon sensitive volume (contrary to planar configuration). In fact, counts up to an energy of 4.7 MeV, the Q value of the reaction, are also registered meaning that in some events both particles leave almost all their energy. The cut-off energies near 2.05 MeV and 2.72 MeV are also observed in the spectra.

According to Figure 3.22 the highest efficiency should be reached when detectors are irradiated from back-side but, results from 3.63a show that total counts from the front-side almost double the number of counts from back-side irradiation, and counts from 45° front-side are ∼2.5 times the number of counts from 45° back-side irradiation. These efficiency drops for back-side irradiation are caused by the composition of the PCB [55]: fiberglass, which is the main component of the PCB, contains boron oxide and when neutrons pass through the board there is a percentage of them that are absorbed. Therefore, the flux of neutrons reaching the sensor from back-side irradiation is lower than from front-face irradiation. The ratio difference between front- and back-side and between 45° front- and 45° back-side are due to differences on the path of neutrons through the PCB. In the backside case neutrons cross the 1.57 mm thickness of the PCB while in the 45 °C backside case, neutrons cross $\sqrt{2} \cdot 1.57$ mm because of the 45° tilt.

Figure 3.63b shows the simulated efficiencies of 15 µm and 25 µm sinusoidal and hexagonal trench width as a function of ^{6}LiF density for an LLD=480 keV and with back-side irradiation (for a better comparison with experimental results the sinusoidal 25 µm trench width curve is shown

thicker). In the simulation neither the converter layer in the surface of the sensor nor the PCB[1] were attached, so front- and back-side irradiation results are approximately the same. As already shown in section 3.5.3, for ^{6}LiF converter material the efficiency increases as the density increases and, in the case of the 25 µm sinusoidal trench this efficiency ranges from 9.45% for a density of 0.75 g/cm^3 to 17.92% for a density of 2.50 g/cm^3. The maximum intrinsic detection efficiency of 8.6±0.4 obtained experimentally (see Table 3.9) is in agreement with the simulation results for low converter densities (∼0.75 g/cm^3) According to SEM images (see Figure 3.35), the low achieved value of efficiency is more due to voids between converter material than to a constant density of 0.75 g/cm^3.

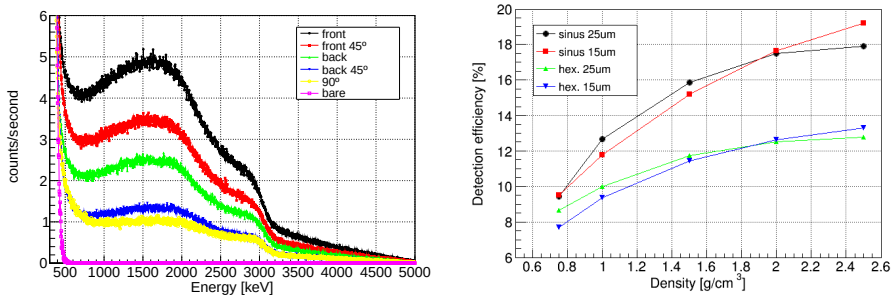

(a) **(b)**

Figure 3.63: (a) Energy calibrated spectra of a microstructured detector with 25 µm sinusoidal trenches for different irradiation angles. The response of the bare detector is also shown in the plot. The reactor power was 100 kW and the sensor was biased at 3 V. (b) Simulated thermal neutron detection efficiencies for normal incidence as a function of ^{6}LiF density and for an LLD=450 keV.

Table 3.9 shows the intrinsic and the effective intrinsic thermal neutron detection efficiencies for all irradiation angles calculated for an LLD=480 keV. Intrinsic efficiency is calculated with Equation 3.8 and the effective intrinsic efficiency with Equation 3.9.

[1] In the simulation program the percentage of each component of the PCB is required and no precise data of that were found on the literature.

From Table 3.9 note that the intrinsic efficiency increases as the detector is rotated from normal incidence to 90°; but, when corrected by $\cos(\theta)$, the effective intrinsic efficiency decreases as the detector is rotated from normal to 90°. Because the detector area is decreasing as the detector is rotated from normal incidence, the overall effect is to reduce the count rate and, hence, the effective intrinsic efficiency of the detector is reduced.

Table 3.9: Intrinsic (ε) and effective intrinsic (ε_e) thermal neutron detection efficiencies for each irradiation angle. Notice that due to the definition of ε_e, efficiencies of back and front irradiation are equal. The standard deviation was calculated assuming a $\pm$ 20 keV error in the energy calibration of the spectra, a 5 % in the determination of the radiation fluence an a $\pm$ 5° in the detector alignment.

Irradiation angle	ε (%)	ε_e (%)
front	8.6 $\pm$ 0.4	8.6 $\pm$ 0.4
front 45°	8.7 $\pm$ 0.8	4.3 $\pm$ 0.3
back	4.5 $\pm$ 0.3	4.5 $\pm$ 0.3
back 45°	3.5 $\pm$ 0.5	1.7 $\pm$ 0.1
90°	70 $\pm$ 50	(6 $\pm$ 5)$\cdot 10^{-2}$

3.7 Neutron imaging detector

Neutron imaging is a non-destructive technique which represents a valuable complement to conventional X-ray technology. The information obtained is complementary since neutrons interact with the atomic nuclei and X-ray with the electron cloud of the target. Due to these different interaction mechanisms neutrons are able to image light elements, penetrate heavy materials and distinguish between different isotopes of the same material.

Research reactors and accelerator-based spallation neutron sources can provide intense neutron beams, required for efficient and practical neutron

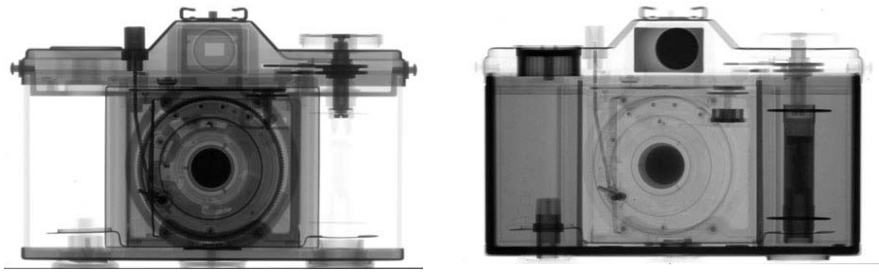

(a) (b)

Figure 3.64: Radiography of a camera by (a) X-rays and (b) neutrons - While X-rays are attenuated more effectively by heavier materials like metals, neutrons make it possible to image some light materials such as hydrogenous substances with high contrast: in the X-ray image, the metal parts of the photo apparatus are seen clearly, while the neutron radiography shows details of the plastic parts (like the film reel). Image from Paul Scherrer Institute (PSI).

imaging. Such beams have been successfully used during the last two decades in many applications like fuel cell research, study of objects from cultural heritage, etc [56]. The extension of applications into new domains using neutron imaging depends very much on the performance of the beam lines and on the new position sensitive neutron detectors.

3.7.1 Pixel silicon sensor

A pixel silicon sensor for thermal neutron imaging has been fully fabricated at the IMB-CNM Institute's clean room. The technology employed to manufacture this pixel silicon detector is based in the well known planar technology so the fabrication steps will not be explained in this thesis.

The sensor is based on the Medipix 2 geometry [57] with 256 x 256 active pixels of 55 µm providing an active area of 2 cm^2. The device was fabricated on an n-type high-resistivity wafer of 200 µm thickness in order to reduce the sensitivity to gamma radiation. The fabrication process was tuned so that the entrance window of the detector (on the back-side) is

as thin as possible (0.4 µm) to drastically reduce the self-absorption of the products from the nuclear reaction. Figure 3.65 sketches the cross section of the device after the bump bonding process but without the neutron converter layer that would be placed at the ohmic n^+ contact of the sensor.

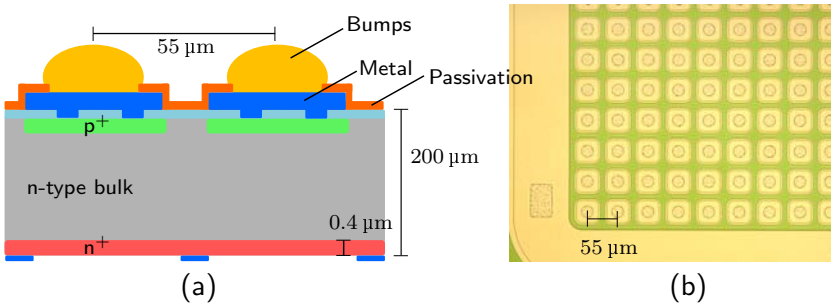

Figure 3.65: Pixel silicon sensor - (a) Sketch of the sensor (not to scale) and (b) optical microscope top view image. The converter layer is not shown in the sketch, but this would be deposited over the detector back-side.

The sensor readout is done via the XRI-UNO Medipix-2 based camera developed by X-Ray Imatek [58]. The XRI Software suite included allows to switch between the three different operations modes of pixels, calibrate the unit and select the image format acquisition. Technical specifications like 13-bit dynamic range and frame rate up to 500 fps makes XRI-UNO camera suitable for neutron imaging.

Figure 3.66 shows a picture of a manufactured wafer with 18 pixel silicon sensors. To adapt the pixel silicon sensor for neutron imaging, converter materials based on boron-10, such as natural and enriched boron, were selected because the high cross sections of the ^{10}B isotope and because of the low range of the reaction products, would provide better spatial resolution than ^{6}Li.

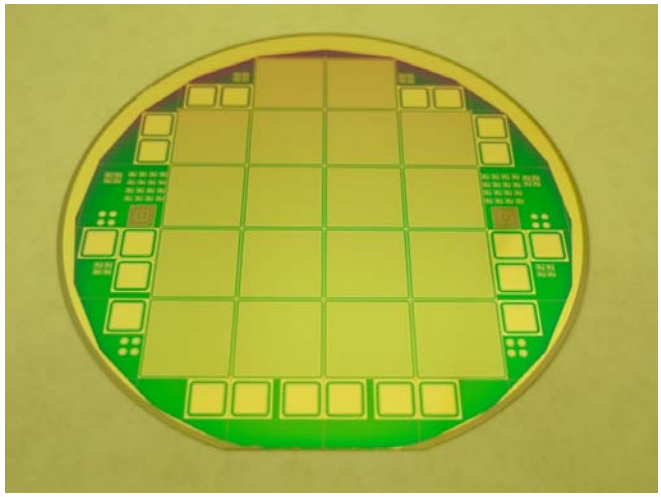

Figure 3.66: Photograph of manufactured wafer with the pixel silicon sensors - 18 sensors were fabricated in each wafer.

3.7.2 Test in nuclear reactor

Thermal neutron irradiations were performed at the nuclear reactor of the Instituto Tecnolgico e Nuclear (ITN) in Lisbon. The thermal neutron flux was $(5.1 \pm 0.2) \cdot 10^5$ n/cm^2/s for 1 MW reactor power and the gamma dose rate at the same position was 5.6 ± 0.4 μGy/s (Table 3.8).

Due to schedule issues neither natural nor enriched boron coated devices were tested in the nuclear reactor but, as a proof of concept, the BE10 screen by Kodak (see section 3.4.3.2) was used instead as the converter material. The BE10 screen was stuck onto the back-side of the sensor with care of not creating an air layer between them.

The experimental setup was composed by a lead block (located and the beam exit to reduce the contribution of gamma-rays reaching the sensor) followed by the object to be imaged and the sensor connected to the XRI-UNO Medipix-2 based camera. Both object and silicon sensor were carefully placed in a plane perpendicular to the neutron beam direction (see Figures 3.67a and 3.68a).

All images were taken at 80 V bias voltage[1] because, as the converter layer is placed on the back-side, a fully depleted sensor is needed to collect all the energy deposited by the charged particles of the neutron reactions. First images were taken with bare detectors (without the BE10 screen) to get the flat field images of the radiation environment.

Figure 3.67b and figure 3.68b show the 600 seconds acquisition time raw images obtained with the pixel neutron detector with the BE10 screen of Kodak. The image size is 14.1 mm x 14.1 mm and the calibration bar has been normalized to the highest pixel count number.

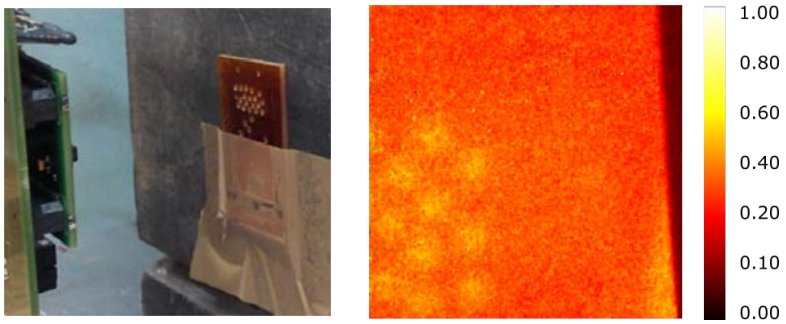

Figure 3.67: (a) Imaging setup. (b) Thermal neutron image of a perforated printed circuit board (PCB).

In Figure 3.67 the object to be imaged is a printed circuit board (PCB) with holes of 1.2 mm diameter. As seen in section 3.6.3, thermal neutrons are absorbed by the boron and plastic components of the PCB and therefore regions where the holes are located are observed with a higher number of counts. According to the number of counts in the image, the thermal neutron attenuation caused by the 1.5 mm thick PCB is ≈70%, in agreement with the front/back ratio seen with the MS sensors (Table 3.9). Figure 3.68 shows the image obtained when a light emitting diode (LED) is placed between the thermal neutron beam and the sensor. As the LED

[1]From the doping levels of the p^+ and the n-type bulk regions, it is calculated that a bias voltage of 80 V is suitable to completely deplete the 200 µm wafer.

has a plastic cover, a fraction of thermal neutrons interact with it and do not reach the silicon sensor. In this case, the attenuation can be approximated to 80%. There is a visible dark region with almost no counts in one side of both images because the neutron converter material does not fully cover the 14.1 mm x 14.1 mm active area of the detector (BE10 screen was not perfectly placed to cover the whole area of the sensor). The few counts in this region are attributed to gamma interactions with the 200 µm silicon sensor thickness.

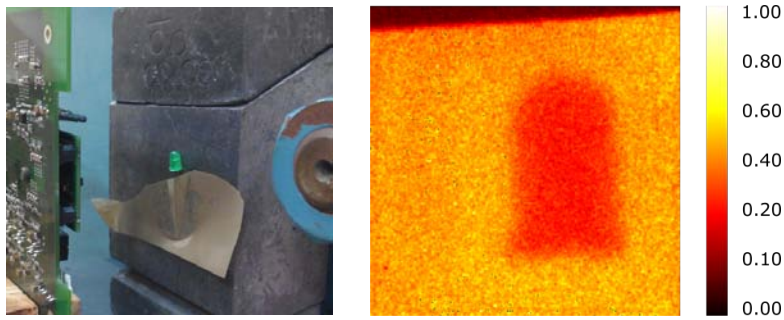

Figure 3.68: (a) Imaging setup. (b) Thermal neutron image of a light-emitting diode.

The 600 second exposure time to achieve Figures 3.67b and 3.68b is enough to visualize the shape of the image however, to get better contrast and resolution a longer exposure time is needed. The resolution is mainly associated to the pitch value of the sensor, however the isotropic emission of the ^{10}B(n,α)^{7}Li reaction products, their range and the silicon thickness are factors that contribute to reduce the resolution.

Results shown in this section demonstrate the viability of the pixel sensor fabricated at CNM coupled to the XRI-UNO readout electronics to obtain images from a thermal neutron beam irradiation. Next steps will consist in the deposition of an optimized boron converter layer to reduce the long exposure times to obtain better resolution.

Bibliography

[1] Glenn F. Knoll. **Radiation Detection and Measurement**, 2010. 45

[2] J.R.D. Copley and T.J. Udovic. **Neutron time-of-flight spectroscopy**, 1993. 46

[3] A N Caruso. **The physics of solid-state neutron detector**. **443201**. 47, 54

[4] Richard T. Kouzes, James H. Ely, and Mitchell L. Woodring. **Neutron detection alternatives to 3He for national security applications**. *Nuclear Instruments and Methods in Physics Research, Section A: Accelerators, Spectrometers, Detectors and Associated Equipment*, **623**(3):1035–1045, 2010. 47

[5] Richard T. Kouzes, James H. Ely, Luke E. Erikson, Warnick J. Kernan, Azaree T. Lintereur, Edward R. Siciliano, David C. Stromswold, and Mitchell L. Woodring. **Alternative Neutron Detection Testing Summary**. Technical report, Pacific Northwest National Laboratory (PNNL), Richland, WA (United States), apr 2010. 47

[6] D. Reilly, N. Ensslin, H. Jr. Smith, and S. Kreiner. **Passive nondestructive assay of nuclear materials**. 1991. 47, 50, 54

[7] Andy Coghlan. **Huge newfound deposit of helium will keep MRI scanners running**, 2016. 50

[8] L.J. Wittenberg, E.N. Camerson, G.L. Kulcinski, S.H. Ott, J.F. Santarius, G.I. Sviatoslavsky, I.N. Sviatoslavsky, and H.E. Thompson. **A review of 3He resources and acquisition for use as fusion fuel**. *Fusion Technology*, **21**(4):2230–2253, 1992. 50

[9] R.V. Babcock, R.E. Davis, S.L. Ruby, K.H. Sun, and E.D. Wolley. **Coated semiconductor is tiny neutron detector**. *Nucleonics*, **17**:116–122, 1959. 56

[10] Douglas S Mcgregor, Raymond T Klann, Holly K Gersch, and Jeffrey D Sanders. **Designs for Thin-Film-Coated Semiconductor Thermal Neutron Detectors**. pages 1–5, 2001. 56

[11] T Slavicek, M Kralik, D Krapohl, S Petersson, S Pospisil, and Thungstrom G. **A thermal neutron detector based on planar silicon sensor with TiB2 coating**. **01053**, 2012. 56

[12] Zhehui Wang and C. L. Morris. **Multi-layer boron thin-film detectors for neutrons**. In *Nuclear Instruments and Methods in Physics Research, Section A: Accelerators, Spectrometers, Detectors and Associated Equipment*, **652**, pages 323–325, 2011. 56

[13] Carina Höglund, Jens Birch, Ken Andersen, Thierry Bigault, Jean-Claude Buffet, Jonathan Correa, Patrick van Esch, Bruno Guerard, Richard Hall-Wilton, Jens Jensen, Anton Khaplanov, Francesco Piscitelli, Christian Vettier, Wilhelmus Vollenberg, and Lars Hultman. **B4C thin films for neutron detection**. *Journal of Applied Physics*, **111**(10):104908, 2012. 56, 70

[14] John W. Murphy, George R. Kunnen, Israel Mejia, Manuel A. Quevedo-Lopez, David Allee, and Bruce Gnade. **Optimizing diode thickness for thin-film solid state thermal neutron detectors**. *Applied Physics Letters*, **101**(14), 2012. 56

[15] Massimo Barbagallo, Luigi Cosentino, Vittorio Forcina, Carmelo Marchetta, Alfio Pappalardo, Paolo Peerani, Carlotta Scirè, Sergio Scirè, Maria Schillaci, Stefano Vaccaro, Gianfranco Vecchio, and Paolo Finocchiaro. **Thermal neutron detection using a silicon pad detector and LiF removable converters.** *The Review of scientific instruments*, **84**(3):033503, 2013. 56

[16] D.S. McGregor, M.D. Hammig, Y.-H. Yang, H.K. Gersch, and R.T. Klann. **Design considerations for thin film coated semiconductor thermal neutron detectors-I: basics regarding alpha particle emitting neutron reactive films**. *Nuclear Instruments and Methods in Physics Research Section A: Accelerators, Spectrometers, Detectors and Associated Equipment*, **500**(1-3):272–308, 2003. 56, 57

[17] Douglas S. McGregor, Raymond T. Klann, Jeffrey D. Sanders, John T. Lindsay, Kurt J. Linden, Holly K. Gersch, P. M. De Lurgio, Charles L.

Fink, and Elsa Ariesanti. **Recent results from thin-film-coated semiconductor neutron detectors**. *International Symposium on Optical Science and Technology*, **4784**(785):164–182, 2003. 57

[18] R. Muminov and L. Tsvang. **High-efficiency semiconductor thermal-neutron detectors**. *Sovietic Atomic Energy*, **62**:316–319, 1987. 57

[19] D. McGregor, R.T. Klann, H.K. Gersch, E. Ariesanti, J.D. Sanders, and B. Vanderelzen. **New surface morphology for low stress thin-film-coated thermal neutron detectors**. *IEEE Transactions on Nuclear Science*, **49**(4):1999–2004, 2002. 58

[20] R J Nikolic, A M Conway, R Radev, Q Shao, L Voss, T F Wang, J R Brewer, C L Cheung, L Fabris, C L Britton, and M N Ericson. **Nine element Si-based pillar structured thermal neutron detector**, 2010. 58

[21] R J Nikolic, Q Shao, L F Voss, A M Conway, R Radev, T F Wang, M Dar, N Deo, C L Cheung, L Fabris, C L Britton, and M N Ericson. **Si pillar structured thermal neutron detectors: fabrication challenges and performance expectations**, 2011. 58

[22] R Dahal, K C Huang, J Clinton, N LiCausi, J.-Q. Lu, Y Danon, and I Bhat. **Self-powered micro-structured solid state neutron detector with very low leakage current and high efficiency**. *Applied Physics Letters*, **100**(24), 2012. 58

[23] R Mendicino, M Boscardin, S Carturan, G Dalla Betta, and M Dalla Palma. **Nuclear Instruments and Methods in Physics Research A Characterization of 3D and planar Si diodes with different neutron converter materials**. *Nuclear Inst. and Methods in Physics Research, A*, pages 1–6, 2015. 58

[24] Justin Dingley, Yaron Danon, Nicholas Licausi, Jian-qiang Lu, Ishwara B Bhat, and Nuclear Engineering. **Optimization of a novel solid-state self powered**. *International Conference on Mathematics, Computational Methods & Reactor Physics*, 2009. 58

[25] R J Nikolic, Chin Li Cheung, C E Reinhardt, and T F Wang. **Roadmap for High Efficiency Solid-State Neutron Detectors**. 2005. 58, 82

[26] Ryan G. Fronk, Steven L. Bellinger, Luke C. Henson, Taylor R. Ochs, Colten T. Smith, J. Kenneth Shultis, and Douglas S. McGregor. **Dual-sided microstructured semiconductor neutron detectors (DSMSNDs)**.

Nuclear Instruments and Methods in Physics Research Section A: Accelerators, Spectrometers, Detectors and Associated Equipment, pages 1–6, 2015. 58

[27] Douglas S. McGregor, Steven L. Bellinger, and J. Kenneth Shultis. **Present status of microstructured semiconductor neutron detectors**. *Journal of Crystal Growth*, **379**:99–110, 2013. 58, 82, 101

[28] Q. Shao, L. F. Voss, a. M. Conway, R. J. Nikolic, M. a. Dar, and C. L. Cheung. **High aspect ratio composite structures with 48.5% thermal neutron detection efficiency**. *Applied Physics Letters*, **102**(6):063505, 2013. 58

[29] Steven L Bellinger, Ryan G Fronk, Luke C Henson, Taylor R Ochs, Timothy J Sobering, and Douglas S Mcgregor. **Microstructured Semiconductor Neutron Detector (MSND) -based Helium-3 Replacement Technology**. (August 2015):2–5, 2014. 58

[30] S L Bellinger, R G Fronk, W. J. McNeil, T J Sobering, and D. S. McGregor. **Improved high efficiency stacked microstructured neutron detectors backfilled with nanoparticle 6LiF**. *IEEE Transactions on Nuclear Science*, **59**(1 PART 2):167–173, 2012. 58

[31] Helmuth Spieler. *Semiconductor Detector Systems*. Oxford University Press, 2007. 60

[32] J P Balbuena, G Pellegrini, C Fleta, F García, C Guardiola, M Lozano, D Quirion, and M Ullán. **Study of Surface Effects in the Operation of 3D Microstrip Detectors with Ultra-thin Silicon Substrates**. **3**:940–943, 2012. 68

[33] A Lousa, J Esteve, S Muhl, and E Martinez. **BCN thin films near the B4C composition deposited by radio frequency magnetron sputtering**. *Diamond and Related Materials*, **9**(36):502–505, 2000. 69

[34] E Pascual, E Martinez, J Esteve, and A Lousa. **Boron carbide thin films deposited by tuned-substrate RF magnetron sputtering**. *Diamond and Related Materials*, **8**(25):402–405, 1999. 69

[35] E Martinez, A Lousa, and J U Esteve. **Micromechanical and microtribological properties of BCN thin films near the B4C composition deposited by r.f. magnetron sputtering**. pages 1892–1896, 2001. 69

[36] Leyre Martínez de Olcoz Sainz. *Caracterización física y funcional de recubrimientos en capa fina depositados por PVD para aplicaciones avanzadas*. PhD thesis, 2014. 69

[37] A Lousa and S Gimeno. **Ion assisted deposition of thin films by substrate tuned radio frequency magnetron sputtering**. *Journal of Vacuum Science and Technology A*, **15**(1), 1997. 69

[38] A Lousa, E Martinez, J Esteve, and E Pascual. **Effect of ion bombardment on the properties of B4C thin films deposited by RF sputtering**. *Thin Solid Films*, **355356**:210–213, 1999. 70

[39] **Dosirad Company. http://www.dosirad.fr/fr**. 73

[40] C Guardiola, C Fleta, K Amgarou, and M Lozano. **Monte Carlo simulations of a microstructured silicon detector with high efficiency for thermal neutrons**. *Journal of Instrumentation*, **7**(06):T06003, 2012. 75, 83, 105

[41] **http://www.sigmaaldrich.com/spain.html**. 81

[42] Kuan-Chih Huang, Rajendra Dahal, Nicolas Licausi, James J Lu, and New York. **Boron filling of high aspect ratio holes by chemical vapor deposition for solid-state neutron detector applications**. **30**(5):1–6, 2012. 82

[43] Consuelo Guardiola Salmer. *Novel silicon sensors for neutron detection*. PhD thesis, 2012. 82

[44] C GUARDIOLA, M Lozano, C FLETA, G Pellegrini, and D QUIRION. **Detector liquido-semiconductor de neutrones**, 2014. 82

[45] Viacheslav Barsykov and Kiev National. **The Influence of Polymer Binders on the Performance of Cathodes for Lithium-Ion Batteries**. **21**(i):67–71, 2016. 85

[46] D.J. Hamman and C.L. Hanks. **Radiation effects desing handbook**. Technical report, NASA, United States, 1971. 85

[47] Ashish Jain, S Anthonysamy, K Ananthasivan, R Ranganathan, Vinit Mittal, S V Narasimhan, and P R Vasudeva Rao. **Characterization of electrodeposited elemental boron**. *Materials Characterization*, **59**(7):890–900, 2008. 87

[48] James F. Ziegler, M. D. Ziegler, and J. P. Biersack. **SRIM - The stopping and range of ions in matter (2010)**. *Nuclear Instruments and Methods in Physics Research, Section B: Beam Interactions with Materials and Atoms*, **268**(11-12):1818–1823, 2010. 88

[49] Douglas S McGregor and J Kenneth Shultis. **Reporting detection efficiency for semiconductor neutron detectors: A need for a standard**. *Nuclear Instruments and Methods in Physics Research Section A: Accelerators, Spectrometers, Detectors and Associated Equipment*, **632**(1):167–174, 2011. 91

[50] J.K. Shultis and D.S. McGregor. **Design and performance considerations for perforated semiconductor thermal-neutron detectors**. *Nuclear Instruments and Methods in Physics Research Section A: Accelerators, Spectrometers, Detectors and Associated Equipment*, **606**(3):608–636, 2009. 101

[51] C.J. Solomon, J.K. Shultis, and D.S. McGregor. **Reduced efficiency variation in perforated neutron detectors with sinusoidal trench design**. *Nuclear Instruments and Methods in Physics Research Section A: Accelerators, Spectrometers, Detectors and Associated Equipment*, **618**(1-3):260–265, 2010. 102

[52] J G Marques, M Sousa, J P Santos, and A C Fernandes. **Characterization of the fast neutron irradiation facility of the Portuguese Research Reactor after core conversion**. *Applied Radiation and Isotopes*, **69**(8):1128–1130, 2011. 105, 115, 116

[53] A C Fernandes and J G Marques. **Thermoluminescence dosimetry of a thermal neutron field and comparison with Monte Carlo calculations**. 2004. 105

[54] A C Fernandes, J P Santos, J G Marques, A Kling, A R Ramos, and N P Barradas. **Validation of the Monte Carlo model supporting core conversion of the Portuguese Research Reactor (RPI) for neutron fluence rate determinations**. *Annals of Nuclear Energy*, **37**(9):1139–1145, 2010. 106

[55] Clyde F Coombs. *Printed circuits handbook*. McGraw-Hill Education; 6 edition, 2007. 119

[56] Eberhard H. Lehmann and Werner Wagner. **Neutron imaging at PSI: a promising tool in materials science and technology**. *Applied Physics A*, **99**(3):627–634, 2010. 122

[57] X Llopart, M Campbell, D San Segundo, E Pernigotti, and R Dinapoli. **Medipix2, a 64k pixel read out chip with 55 mu;m square elements working in single photon counting mode**. In *Nuclear Science Symposium Conference Record, 2001 IEEE*, **3**, pages 1484–1488 vol.3, nov 2001. 122

[58] **X-Ray Imatek**. 123

Part III

Microdosimetry

4

Silicon sensors for microdosimetry

This chapter introduces the concept of hadron therapy and describes the basic concepts related to the microdosimetry field as well as the main microdosimetry quantities. Also, the fabrication and the experimental validation at the irradiation facilities of: Grand Accélérateur National d'Ions Lourds (GANIL) and Centro Nacional de Aceleradores (CNA) of the two silicon-based microdosimeters fabricated at the IMB-CNM clean room are described.

4.1 Hadron therapy

Hadron therapy is an innovative high-precision cancer radiotherapy[1] modality based on hadrons such as protons or heavier ions, e.g. carbon, oxygen, etc. Hadron therapy achieves very high dose conformity around the target, allowing a better protection of the organs at risk which is particularly critical for certain types of radioresistan tumours, such as hypoxic tumors, for those localized near organs at risk or sensitive structures (e.g. the spinal cord), and for pediatric cancers [1].

In 1946, accelerator pioneer Robert Wilson laid the foundation for hadron therapy with his article about the therapeutic interest of protons for treating cancer [2] and, in 1950s the first clinical use of protons took place at the University of California Lawrence Berkeley Laboratory[2]. Since then, more than 100,000 patients have been treated worldwide with this therapy (approximately 85% with protons and approximately 15% with heavier ions, mainly carbon [3]). At present, 57 proton and 10 carbon ion therapy facilities are in operation worldwide [4], however cancer treatment still presents a real challenge and it is the second highest cause of death in developed countries. According to estimates from the Agency for Research on Cancer (IARC) [5], in 2012 approximately 14 million new cancer patient were diagnosed and 8.2 million cancer deaths were registered worldwide and by 2030 this number is expected to grow to 21.7 million new cancers. The clinical interest in hadron therapy as a promising alternative to state-of-the-art X-ray external beam therapy has therefore risen significantly within the last decade [6, 7] (from about 3000 patients treated in 2005 to about 15000 patients in 2014 [3]).

Hadrons are more advantageous with respect to conventional radiotherapy mainly due to: (a) the physical depth-dose distribution delivered

[1] Radiotherapy (RT) refers to the medical use of ionizing radiation to treat malignant tissues. The radiation may be delivered by a machine outside the body (external-beam radiation therapy), or it may come from radioactive material placed in the body near cancer cells (internal radiation therapy, also called brachytherapy).

[2] Hadron therapy with heavy ions started in the 1970 in Berkeley.

by them has a small dose in the entrance in tissue, but depositing a larger amount at the end of their ranges (Bragg peak) with a sharp fall-off at the distal edge (see Figure 4.1); (b) their tracks generate a dense ionization which is able to induce multiple single or double strand breaks (SSB or DSB) in the cell DNA that may lead to non-reparable cellular damages. This property is accounted for in terms of the relative biological effectiveness (RBE), which is defined as the ratio between the dose required to achieve a given biological effect with conventional RT (typically with 250 keV X-rays) and that to achieve the same effect with a hadron beam considered.

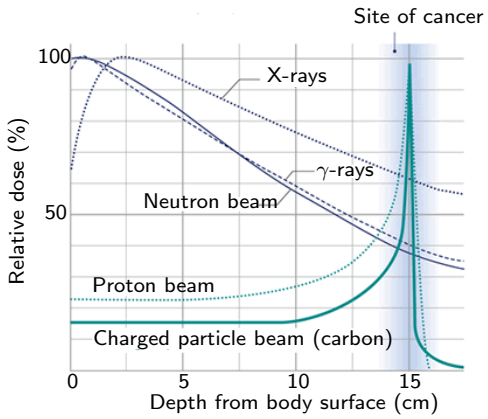

Figure 4.1: Distribution of depth versus dose for various types of radiation in tissue - Figure adapted from National Institute of Radiological Sciences (NIRS) [8].

Figure 4.1 shows the dose distribution at different depths of tissue for various types of radiation. In X-rays or γ-rays beams there is an increase of dose deposit in the first few centimeters, and after that the dose drops essentially according to an exponential law. However, for charged particles almost all the dose is deposited in the final millimeters of their path. Charged particles deliver a low dose at the body's surface (when their velocity is high), and only shortly before the maximal penetration depth there is a steep increase of the dose deposition and a sharp drop of the dose

after. The very narrow and localized peak is known as the Bragg peak and by proper selection of the ion energy, the position in depth of the Bragg peak can be adjusted with high precision, in order to concentrate the higher absorbed dose to the tumor location.

Since the Bragg peak for particles of a given energy is too narrow to treat tumour volumes of typical dimensions of a few cm size, beams of different energies can be superimposed to produce a spread-out Bragg peak[1] (SOBP) and extend in this way the uniform dose region in depth. The Bragg curve characteristics clearly indicate that hadron therapy can provide excellent dose distributions in patients, even compared with the most advanced X-ray methods, such as intensity-modulated radiation therapy (IMRT) [9] (see Figure 4.2).

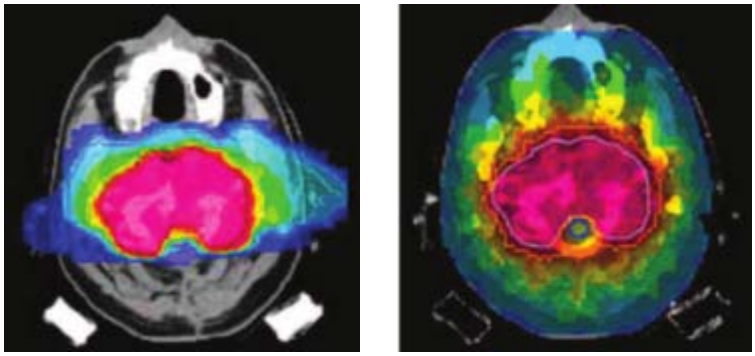

(a) **(b)**

Figure 4.2: Comparison of treatment plans for a large target volume in the base of the skull - (a) Plan for carbon ions (two fields). (b) Plan for IMRT (nine fields). Clearly, use of carbon ions would result in a substantial reduction in the integral dose to the normal tissue and the sparing of critical structures. Figure adapted from [10].

Compared with protons, heavy ions offer higher peak-to-entrance dose ratio, small angular scattering[2] and increased biological damage per unit of

[1] The SOBP can be also produced by using variable thickness absorbers in the beam.

[2] For example, the increase of the beam spot width is only 1 mm for carbon ions in 20 cm penetration depth compared to about 6 mm for protons.

absorber [11]. These characteristics have made carbon therapy a technique increasingly used for treating some radioresistant tumors. The biggest disadvantage of heavy ions is, however the ion fragmentation process along their penetration path in the patient tissues [12, 13]. This process must be taken into account for the evaluation of the biological effects because: i) leads to an attenuation of the primary beam flux, ii) creates lower Z fragments with increasing penetration depth and iii) contributes to spread out the dose longitudinally and transversally in the surrounding healthy tissues.

4.2 Microdosimetry

Microdosimetry is formally defined as the systematic study and quantification of the *spatial* and *temporal* distributions of the absorbed energy in irradiated microscopic sites [14]. It is a extremely valuable knowledge in fields like radiobiology or radiation therapy where determining the distributions of energy deposition inside biological tissues is crucial to determine their survival fraction.

Microdosimetry can be also defined as the area of dosimetry that studies the fluctuations of energy deposition in microscopic volumes. These fluctuations are depicted in Figure 4.3 where the domains of microdosimetry and dosimetry are distinguished.

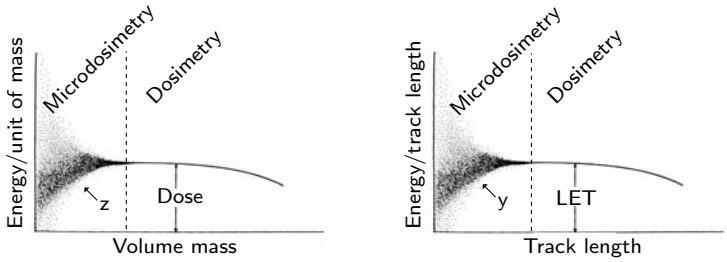

Figure 4.3: Schematic plot showing the domains of microdosimetry and dosimetry - The main quantities used in microdosimetry with their respective random fluctuations, as well as dose and LET, are depicted in the figure. Pictures adapted from [15].

Dose and LET are macroscopic averages of the energy deposited and lost per length unit respectively by the incident radiation in macroscopic volumes, however due to the statistical fluctuations involved in the energy deposition events in a finite micron-sized volume, these magnitudes do not provide a good description of what is likely to happen and new stochastic quantities need to be defined (section 4.2.1). Moreover, the effects of radiation -in particular biological effects- depend not only on these macroscopic averages, but are largely determined by the microscopic pattern in which a given amount of energy is deposited in the medium. Therefore, to quantify the radiobiological damage, it is necessary to evaluate stochastic physical parameters such as the lineal energy (y), which is the micrometer parameter related to a macroscopic LET.

The dose administered in hadron therapy is usually evaluated in terms of the photon-isoeffective dose, calculated as the product of the absorbed dose to water and the relative biological effectiveness (RBE) [16]. The RBE depends on the type of hadron and LET (loss of energy per unit distance along the path), among other parameters, and its concept was introduced to cope with the inadequacy of the sole dose concept and to compare the biological effects of various types of irradiations. For example, from Figure 4.4 it is seen that to cause a cell survival fraction of 50%, doses of about 0.4 Gy and 2.5 Gy are required for 11 MeV/u carbon ions and 250 keV X-rays respectively (these curves can vary for different cell line types).

The aim of microdosimetry is the understanding of these differences in radiation effects and to estimate the RBE of a given radiation type and energy from physical microdosimetric measurements. However, the scope of this thesis is not to predict RBE values since it is a complex parameter which not uniquely depends on the type of radiation, but also depends on the type of tissue involved among other biological parameters [16]. In this chapter microdosimetric spectra will be collected using the silicon-based microdosimeters fabricated at the IMB-CNM and the main microdosimetric quantities will be calculated.

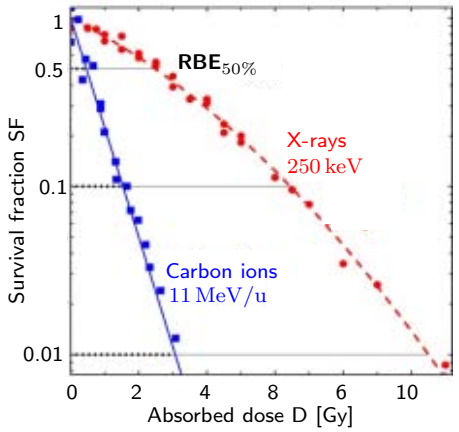

Figure 4.4: The RBE concept illustrated from the cell survival curves - Image obtained from [17].

4.2.1 Microdosimetric quantities

The foundations of microdosimetry started less than 50 years ago from the study and development of measurable quantities that could provide information about the radiation quality (i.e. type of particles and their energy spectra) and could give indicators of the biological effects for a type of radiation. The formal definitions of the principal microdosimetric quantities are given by the International Commission on Radiation Units and Measurements [18] and are briefly explained in this section.

Prior to the description of microdosimetric quantities, it is important to define the energy deposit and the energy imparted. The energy deposit, ε_i, is the energy deposited in a single interaction, i:

$$\varepsilon_i = T_{in} - T_{out} + Q_{\Delta m} \tag{4.1}$$

T_{in} is the kinetic energy of the incident ionizing particle, T_{out} is the sum of the kinetic energies of all particles leaving the transfer point and $Q_{\Delta m}$ is the change of rest mass energy of the atom and all particles involved in the interaction ($Q_{\Delta m} < 0$: decrease of rest mass; $Q_{\Delta m} > 0$: increase of rest mass).

The energy imparted, ε, to the matter in a volume is:

$$\varepsilon = \sum_i \varepsilon_i \tag{4.2}$$

where the summation is performed over all energy deposits, ε_i, in that volume. ε, as well as specific and linear energy, are stochastic quantities[1].

The principal quantities used in microdosimetry are the *specific energy* y and the *lineal energy* z. These quantities describe the energy deposition events in microscopic structures.

The specific energy z:

$$z = \frac{\varepsilon}{m} \tag{4.3}$$

is defined as the radio of the imparted energy by ionizing radiation to a given volume of mass m. The unit is the Gy and is the stochastic analog of the absorbed dose D (see Figure 4.3). The absorbed dose is the limit of the mean specific energy as the mass of the volume approaches to zero.

The lineal energy y:

$$y = \frac{\varepsilon_1}{\bar{l}} \tag{4.4}$$

is defined as the quotient of energy imparted to the matter in a volume of interest by a single energy-deposition event. The usual units are keV/um. The lineal energy y is the stochastic analog to the LET quantity (see Figure 4.3). LET is an average over a large number of primary interactions and cannot describe energy deposition in a small volume where the mean number of interactions is of the order of one or less.

According to Cauchy's theorem, the mean chord length $\bar{l}$ in a convex volume under μ-randomness (in which the body is exposed to a uniform, isotropic field of straight infinite lines) is given by: $\bar{l} = 4V/A$ where A is the surface area of the volume V. For a spherical and a right cylinder cavity, $\bar{l}$ is:

$$\bar{l} = \frac{2}{3} \cdot d \tag{4.5}$$

[1]In brief, stochastic quantities are quantities which are subject to random fluctuations. The expectation value of a stochastic quantity is a non-stochastic quantity. Its value may be estimated as the average of observed values of the associated stochastic quantity.

where d corresponds to the diameter of the sensitive volume. A summary of the mean chord length for various shapes can be found in [19].

Since lineal energy is a stochastic quantity, it is useful to consider its distribution function. The value of the distribution function, $F(y)$, is the probability that the lineal energy is equal to or less than y. The probability density (also called the lineal energy distribution), $f(y)$ is the derivative of F(y) with respect to y:

$$f(y) = \frac{dF(y)}{dy} \tag{4.6}$$

The lineal energy distribution is independent of the absorbed dose or dose rate. The expectation value of the lineal energy distribution, also called the frequency weighted mean lineal energy, is given by:

$$\bar{y}_F = \int_0^\infty y\, f(y)\, dy \tag{4.7}$$

$\bar{y}_F$ is a non-stochastic quantity.

If $D(y)$ is the fraction of absorbed dose delivered with lineal energy less than or equal to y, the dose probability density, $d(y)$, of y is the derivative of $D(y)$ with respect to y:

$$d(y) = \frac{dD(y)}{dy} \tag{4.8}$$

This distribution is also independent of the absorbed dose or dose rate. The expectation value of $d(y)$ is the dose weighted mean lineal energy and is given by:

$$\bar{y}_D = \int_0^\infty y\, d(y)\, dy \tag{4.9}$$

$\bar{y}_D$ is also a non-stochastic quantity. The relationship between $d(y)$ and $f(y)$ is:

$$d(y) = \frac{y}{\bar{y}_F} f(y) \tag{4.10}$$

So the dose weighted mean lineal energy may also be expressed as:

$$\bar{y}_D = \frac{1}{\bar{y}_F} \int_0^\infty y^2\, f(y)\, dy \tag{4.11}$$

Similarly, probability distributions $f(z)$ and average quantities ($\bar{z}_F$, $\bar{z}_D$) are also defined for z.

The usual representation of the microdosimetric spectra is displayed in a semi-logarithmic representation, $y\,d(y)$ vs. $log\,y$ because it provides a useful way to compare spectra of different types of radiation. In this semi-log representation the area under the curve between two y-values is proportional to the fraction of dose delivered by events with lineal energies in this range.

The measured $f(y)$ and $d(y)$ distributions of the lineal energy provide information about the radiation quality and can be useful to estimate the relative biological effectiveness for a particular radiation beam. The RBE is also defined as:

$$RBE = \int y\,d(y)\,r(y)\,d[log(y)] \tag{4.12}$$

where $r(y)$ is an empirical biological weighting function.

4.2.2 State of the art in microdosimeters

Microdosimetric measurements are performed with different types of detectors, the most common ones being the gas-filled Tissue Equivalent Proportional Counters (TEPCs) and solid-state detectors. To investigate microdosimetric spectra, each one has its advantages and limitations regarding tissue-equivalence, small device sizes and construction challenges [18]. Table 4.1 shows a comparison of the typical parameters of TEPC and silicon microdosimeters.

It is important to mention that the microdosimeters described in this work do not differentiate when the ionizations are produced from the primary or from secondary particles because they integrate the number of ionizations occurring inside the sensitive volume. The information about track structure is obtained with nanodosimetry measurements [20] but this will not be treated in this work.

Table 4.1: Comparison of TEPC to silicon microdosimeter. i) Energy deposited and preamplifier noise dependence however, the silicon microdosimeter has potentially better energy resolution. ii) Assuming 2.5 cm spherical TEPC capable of detecting single ionizations and 1 µm^3 cubic silicon microdosimeter with ultra low preamplifier noise [19].

Parameter	**TEPC**	**Silicon microdosimeter**
Energy resolution[i]	Moderate	Moderate
Low energy sensitivity[ii]	Excellent, y_{min}=0.05 keV/µm	Moderate, y_{min}=0.4 keV/µm,
Sensitive volume definition	Good	Moderate
Wall effect	Poor	Excellent
Tissue equivalence	Good	Moderate
Spatial resolution	Poor	Excellent
Model cell array	No	Yes
Cost	High	Low
Portability	Moderate	Excellent

4.2.2.1 TEPC

Tissue equivalent proportional counters are the most common instruments used for the measurement of microdosimetric spectra. TEPC consist of hollow spheres or cylinders that simulate tissue volumes of micrometric size and density of 1 g/cm^3 by means of a tissue-equivalent gas at low pressure. The gas is enclosed in a cavity surrounded by cathode walls and including a central anode wire. The TEPC are based on the requirement that the energy released by charged particles is identical in both tissue and gas volumes for equivalent trajectories.

In TEPC the detector wall and gas filling are chosen with a similar composition to tissue-like material. The detector wall is usually fabricated

with conductive plastic (A-150 plastic developed by Shonka et al. [21]), whose composition is very close to the standard muscular tissue. The most frequently used tissue-equivalent gas mixtures in microdosimetry are methane-based and propane-based gasses [18].

The pulse amplitude derived from a given energy deposition event varies according to the gas amplification factor, determined by the voltage difference between the cathode and the anode. This must be chosen in order to work in the region of true proportionality, where the collected charge is proportional to the number of original ion pairs created by the incident radiation (see section 3.3.1).

Typically TEPCs have a 2.5 cm diameter sensitive volume filled with propane gas at 2266 Pa, which is equivalent to a 1 µm diameter tissue equivalent spherical sensitive volume [22].

The main drawback of TEPCs are the so called *wall-effects* which cause perturbations in the energy deposition and distortions on the experimental microdosimetric distributions [18]. Wall effects may occur due to the scattering effect of the primary and secondary particles caused by the difference in density between the cavity and the surrounding wall. This density difference can alter the pattern of energy deposition from that in a homogenous medium since the spatial distribution of delta-rays produced in a volume of material is directly related to density of the material.

Other drawbacks of TEPCs are high voltage operation, macroscopic size, and the fact that they can only mimic a single, isolated cell equivalent volume. Nevertheless, this type of detector has found wide applications in applied dosimetry [23, 24]. In fact, proportional counters simulating micrometer tissue volumes have served as the primary active dosimeters in space for nearly two decades due to their ability for monitoring the complex radiation environments in space shuttles or in the International Space Station [25].

A more superior device operating under similar principles of TEPC is the miniaturized TEPC [26], which has a much smaller volume than conventional TEPCs. Clinical hadron beams have high particle fluence

rates of at least 10^6 particles/(cm^2·s) and, under these conditions standard TEPCs of about 1 cm suffer pile-up effects which distort the microdosimetric spectra because of their large sensitive volume. Miniaturized TEPCs cope with these high intensity beams and facilitate microdosimetry measurements with higher spatial resolution.

(a)

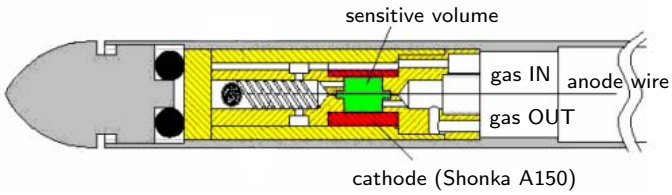

(b)

Figure 4.5: (a) First TEPC developed by Rossi and Rosenzweig (1955) [27] to simulate the measurements of energy deposition in volumes of tissue with dimensions similar to the nucleus of a mammalian cell. (b) Sketch of the mini TEPC build at Legnaro National Laboratories [26]. In green the cylindrical sensitive volume of 0.9 mm both in height and diameter. The red part is the cathode and the yellow part is the insulating plastic. It is inserted in a titanium sleeve of 2.7 mm diameter and 20 cm length.

4.2.2.2 Solid state microdosimeters

Silicon microdosimeters have been under investigation for the past ten years as a possible alternative to TEPCs for microdosimetric measurements in medical physics and radiation protection [28].

Silicon detectors can provide sensitive volumes that correspond to realistic microscopic sizes of the biological components of interest such as the cell or cell nucleus. No contributions of wall effects are present in the measured spectra and, moreover silicon-based detectors are compact and can be transportable.

The main drawback of silicon microdosimeters is the non-tissue equivalence, therefore these devices require a tissue equivalent conversion factor to simulate the energy deposited in tissue. Bradley and co-authors proposed a response correction of silicon microdosimeters in Boron Neutron Capture Therapy (BNCT) and in the proton and neutron radiation fields component of space environment [19, 29, 30]. For these applications they showed that, assuming identical secondary charged particle spectra, a simple geometrical scaling factor of linear dimension is adequate to convert experimentally obtained microdosimetric energy deposition spectra in silicon to equivalent microdosimetric energy deposition spectra in water. This scaling factor was obtained through GEANT4 simulations by comparisons of the range-energy relationships in silicon and tissue for the particles under study. However, obtaining the tissue equivalent conversion factor in different applications is not within the scope of this thesis and no GEANT4 simulations will be presented regarding it.

4.3 SOI microdosimeters from IMB-CNM

Two generations of solid state silicon microdosimeters, manufactured in the clean room of the IMB-CNM Radiation Detector Group, have been developed as a method of measuring energy depositions in a micron sized sensitive volumes. The first generation is the already presented *U3DTHIN* sensor (see section 3.4) and the second generation, manufactured specif-

ically for microdosimetry measurements, is known as *3D Cylindrical microdosimeter*. It is important to mention that this second generation of solid state silicon microdosimeters was manufactured on the basis of the results of the U3DTHIN sensors and on the IMB-CNM's technology.

4.3.1 U3DTHIN as microdosimeters

The ultra-thin 3D sensors were originally developed for plasma diagnostics and neutron detection (see section 3.6.2) but, due to their thin (cell-like) and well defined active volume, they have been also investigated and tested to perform microdosimetric measurements. The fabrication process as well as the electrical characterization of the U3DTHIN sensors are explained in section 3.4.

4.3.2 3D Cylindrical microdosimeter

The 3D Cylindrical microdosimeter is formed by a matrix of independent unit cells (microsensors) with well-defined micrometric cylindrical shape and with a volume similar to those of cellular structures [31].

To provide a visual comparison of dimensions of the microsensors and cells, a HeLa[1] cell culture was growth in the surface of the sensor. Next, the cells were fixed, dehydrated and dried to perform SEM images. Figure 4.6 shows top view SEM images of one microsensor next to a cell. Both microsensor and cell dimensions are in the range of few tens of micrometers.

Each micron-sized cylindrical unit cell consists of an implanted p^+ electrode, that acts as junction electrode, surrounded by a concentric three-dimensional n^+ electrode in the shape of a hollow cylinder as ohmic contact.

[1]HeLa cell is a cell type in an immortal cell line used in scientific research. The line was derived from cervical cancer cells taken on 1951 from Henrietta Lacks. The cell line was found to be remarkably durable and prolific which warrants its extensive use in scientific research.

Three main types of detector structures were fabricated: pad (pixel-array detector), strip and pixel detectors. In each configuration, all n^+ electrodes are connected together with metal lines to an n^+ contact on one side of the sensor. In the pad configuration (the simplest one) all p^+ electrodes are also connected together to an p^+ contact on the opposing side of the sensor. In the strip configuration, consecutive p-type electrodes are lined up, resulting in a strip of connected microsensors in a row. In the pixel configuration each p-electrode is connected to individual pads allowing to read separately each unit cell.

All microsensors are arranged in an square array (most of them in an array of 10 x 10 unit cells). A mask set was designed for the fabrication of the microdosimeters and, in order to investigate a great number of unit cell distribution and sizes, the mask included devices with different internal diameters of 9, 10, 15, 20 and 25 µm, and different separation between p-electrodes (pitch) of 25, 50, 100 and 200 µm.

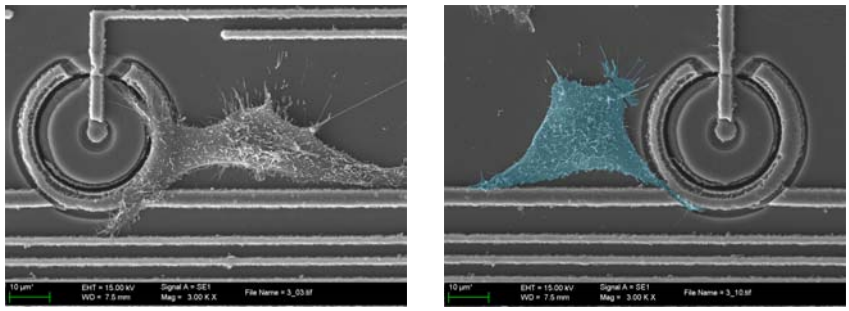

(a) **(b)**

Figure 4.6: Scanning electron microscope images of a HeLa cell grown next to a microsensor - The microsensor has 15 µm diameter and the image is only for size comparison (on the right picture the HeLa cell has been colorized in blue with an image manipulation program).

4.3.2.1 Fabrication process

The 3D Cylindrical microdosimeters were fabricated on three types of 4-inch silicon-on-insulator (SOI) wafers supplied by Icemos Technology Ltd. The active thickness of each type of SOI wafer is 6, 10 and 20 µm. The device silicon is <100>, n-type doped with phosphorus and with a nominal resistivity >3 kΩ cm. The buried oxide and the support silicon thicknesses are 1 µm and 300 µm respectively for all wafers. The whole fabrication process consists of 122 steps and the main ones[1] are briefly explained in the following paragraphs:

1. The processing started with a wafer cleaning and with the growth of a 0.4 µm field oxide on both wafer sides. Then, the first politolithography process (mask level I (P-diff)) to define the p-type electrodes was performed followed by the etching of the 0.4 µm exposed SiO_2. These steps are represented in Figure 4.7.

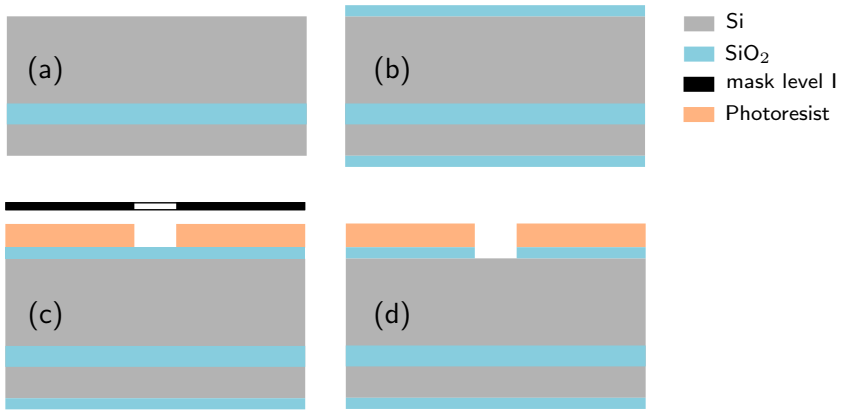

Figure 4.7: (a) SOI wafer and (b) wet oxidation process. (c) Photolitography process and (d) SiO_2 etching.

[1]Several cleaning processes are performed during the fabrication run but they will not be detailed in this section. Most of them, as well as more detailed processes descriptions, are explained in the fabrication of 3DTHIN (section 3.4.1)

2. An ion beam boron implantation was then performed to create the p^+ electrodes of 4 µm diameter. This implantation was done through a very thin SiO_2 layer (365 Å) growth previously on the silicon surface to prevent the channeling of boron ions in silicon. Next, a 0.4 µm SiO_2 layer was grown to protect the p^+ contact from the following steps, and then the second photolithography process (mask level II (Holes-n)) was realized to define the cylindrical annulus of 3 µm width (Figure 4.8).

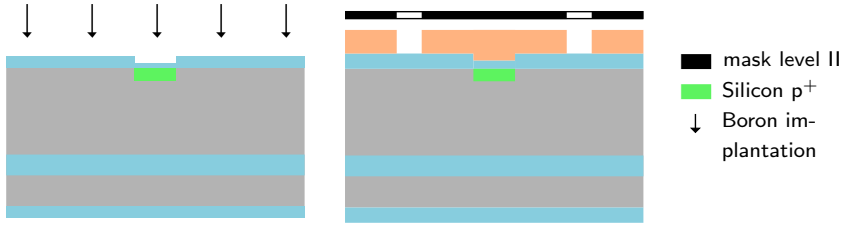

Figure 4.8: Boron implantation of the p^+ electrodes and photolithography process to define the the cylindrical annuli.

3. The next step is the etching of the exposed SiO_2 and the Deep Reactive Ion Etching (DRIE) of the silicon. Depending on the thickness of the SOI wafer the DRIE process will etch 6, 10 or 20 µm of silicon. See Figure 4.9

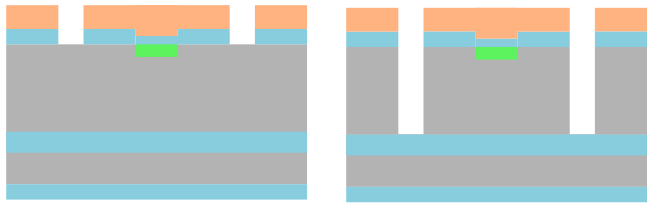

Figure 4.9: SiO_2 etching and DRIE to create the cylindrical annulus.

4. A 500 nm polysilicon deposition process was then realized to partially fill the etched cylindrical annulus. Next, this polysilicon was doped n^+ with phosphorous atoms from a gas source ($POCl_3$) to form the

ohmic contact. Phosphorous atoms in contact with the deposited polysilicon create a PSG (phosphosilicate glass) layer which acts as a source of donor impurities and create the n-doped region. Then, the PSG layer was etched away from both sides of the wafer (Figure 4.10).

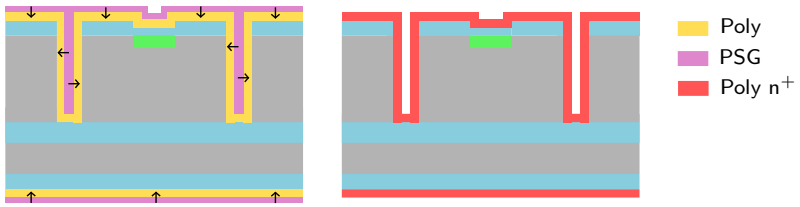

Figure 4.10: Polysilicon deposition and $POCl_3$ doping.

5. The next step was a photolitography process (mask level III (poly-n)) to keep the n^+ polysilicon above the cylindrical annulus and to etch away the rest from other parts of the microsensor. Then the photoresist was removed and the n^+ polysilicon layer on the bottom surface of the sensor was etched (Figure 4.11).

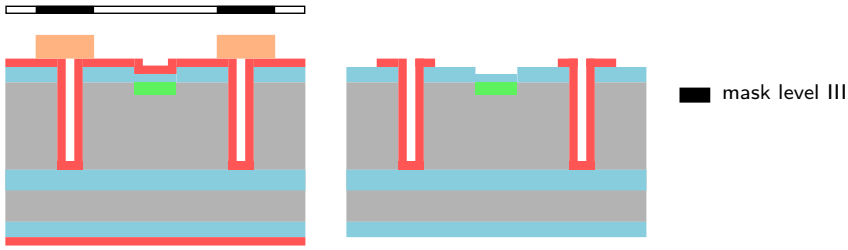

Figure 4.11: Photolithography process to define the n^+ polysilicon regions and etch away the rest.

6. A TEOS-based oxide layer was deposited to fill the trenches and create and adequate insulating layer over the n-doped polysilicon. This is a crucial step as the metal strip contacting the p-electrode crosses over the trench and an incomplete fill could result in an open line or a short-circuit between electrodes. Next a photolithography

process through the mask level IV (window) was performed to open contacts between the doped regions and the metal (that will be deposited later) and then, the unprotected SiO_2 was etched and the photoresist was removed (Figure 4.12).

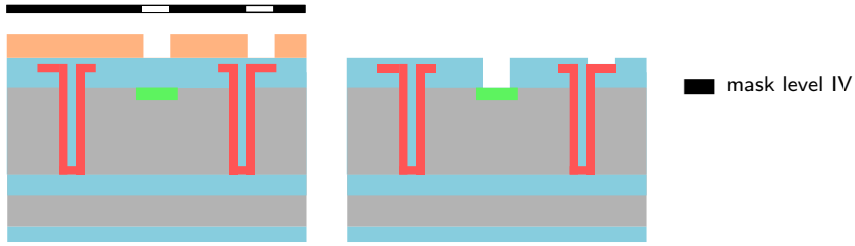

Figure 4.12: SiO_2 growth followed by a photolithography process to create electrical contacts.

7. The next step was to deposit a 0.7 µm metal layer (Al/Cu) to create the electrical contact for each of the unit cells. The metal was first deposited over the whole wafer and then a photolitography process (mask level V (metal)) was performed to protect the desired metal regions. Next, the non-protected metal was etched away. A passivation layer (SiO_2/Si_3N_4) of 0.2 µm was deposited to protect the sensors from external exposure such as humidity and scratches. See Figure 4.13.

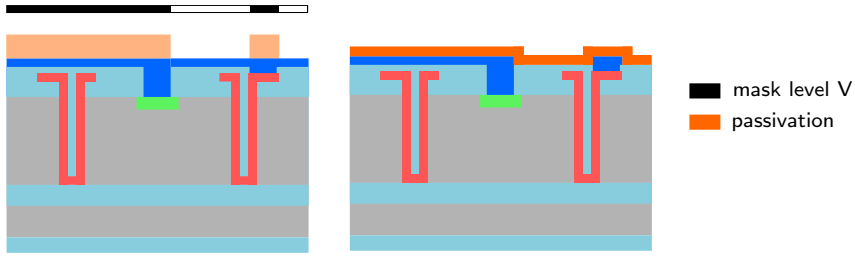

Figure 4.13: Metal and passivation layer depositions. The right sketch shows the final device with the 300 µm silicon support etched away.

8. Finally, the passivation over both n^+ and p^+ contact pads located on both sides of the sensor was selectively etched after the last photolitography step (mask level VI (passivation)) for the signal output. The backside of the wafer can be selectively etched to remove the support silicon below the active areas to avoid contribution of backscattered particles to the charge collection[1]. See Figure 4.14

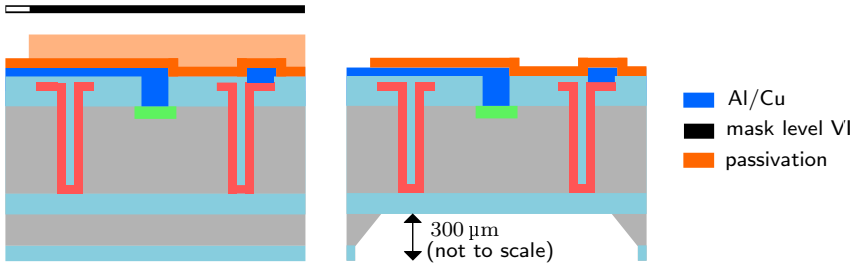

Figure 4.14: Metal and passivation layer depositions. The right sketch shows the final device with the 300 µm silicon support etched away.

Figure 4.15 shows a correlated sketch of the top and cross-section views of the microsensor unit cell. The main common dimensions of all fabricated microsensors are depicted in the figure. The active volume is defined by the thickness of the active silicon layer and by the *diameter* of the cylindrical annulus (diameters of 9, 10, 15, 20 and 25 µm have been manufactured). However, it is important to mention that in the fabricated devices the final diameter of the active silicon will be reduced: in an ideal device the active region is defined in the sides by the internal diameter of the annulus trench, but in practice the limit is given by the depth of the n^+ diffusion because this highly doped region has low collection efficiency and cannot be considered as completely active volume. This effect is shown in Figure 4.16a where the truly sensitive volume is indicated with a white cylinder in the figure (section 4.4.1.4 explains the method used in this thesis to obtain the value of the active diameter). It is also worth

[1]Backside removal is not a requisite for the proper function of the sensor and some tests have been performed with the silicon support.

mentioning that the sensor thickness is not the initial SOI active silicon thickness since in each oxidation step of the fabrication process, a percentage of active silicon (40% of the total oxide thickness grown) is consumed. As it has been measured by SEM images, the sensor thickness results to be 5.4 µm instead of 6 µm.

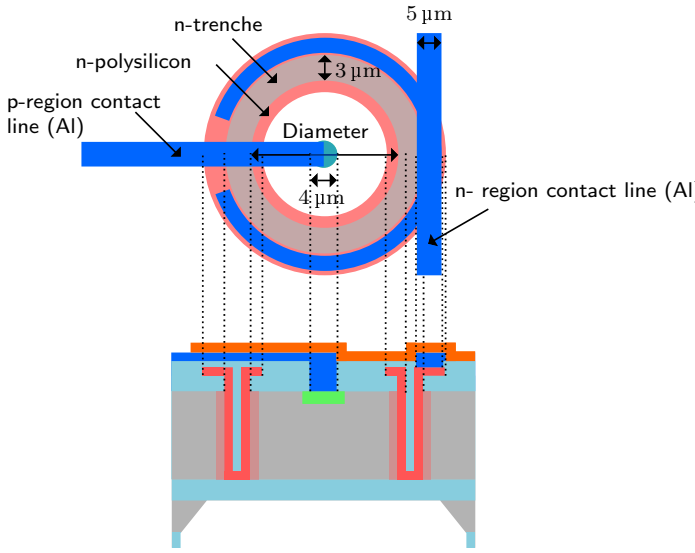

Figure 4.15: Desing of the 3D Cylindrical microdosimeter and schematic cross-section showing the different layers

Figure 4.16b shows a SEM image of four unit cells corresponding to an array of 200 µm pitch. The metal lines that connect the electrodes to the contacts in the periphery are also distinguishable. Figure 4.16c shows a picture of a 6 µm SOI wafer with the backside etched away. The backside etched regions are observed in red due to the transmission of the light through the silicon membranes.

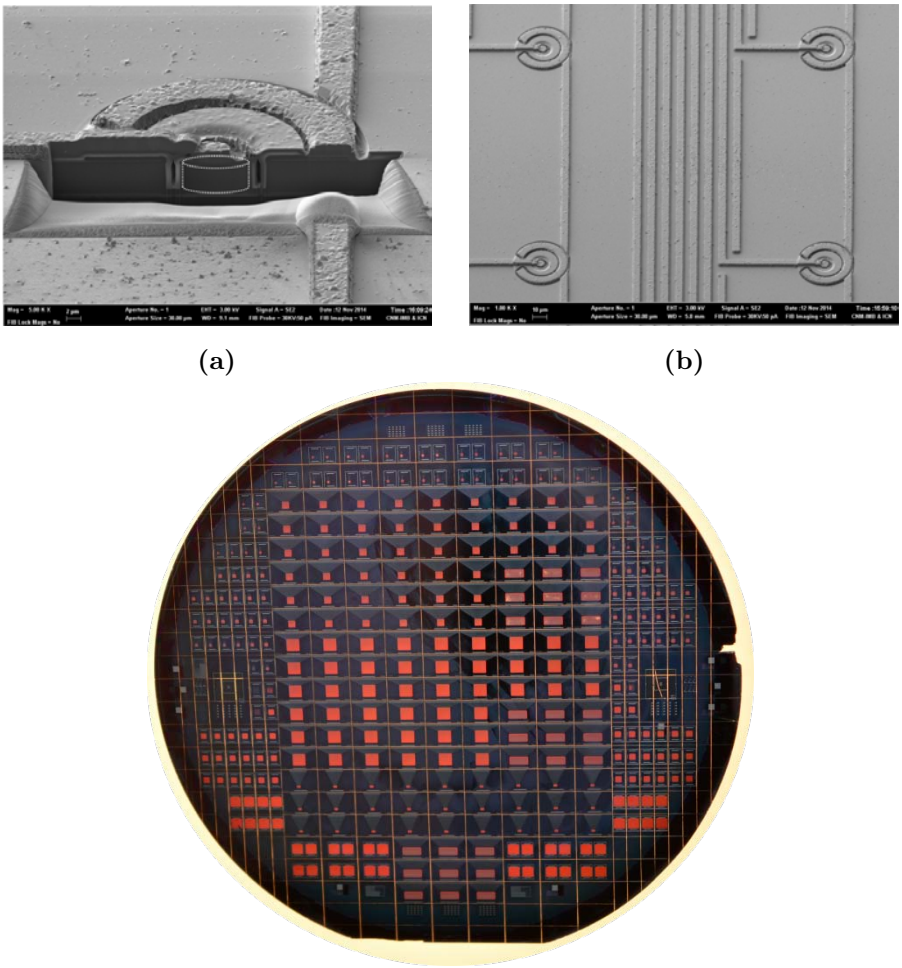

Figure 4.16: (a) SEM image of the section of one manufactured microsensor with 15 µm diameter, 200 µm pitch and 6 µm thickness obtained with a focused ion beam. The sensitive volume is marked with a white cylinder. This image has been obtained by milling the device with a focused ion beam (FIB) of gallium. (b) SEM image of the top-view of a microdosimeter (showing 4 of the 121 microsensors) with the same dimensions as the shown in Figure 4.16a. (c) Photograph of a manufactured 6 µm SOI wafer with the 3D Cylindrical microdosimeters. The 300 µm silicon support of each microdosimeter has been etched away so the 6 µm silicon membranes appear translucent.

4.3.2.2 Electrical characterization

The electrical characterization of all wafers was performed as in explained in Appendix A. The devices were tested on wafer at a controlled room temperature of 20 °C and with an N_2 flow to reduce humidity. Figure 4.17a shows the results for some individual microsensor unit cells with 20 µm diameter. The devices show good diode characteristics with breakdown voltages higher than 60 V and reverse currents of about 100 pA. The likely source of this high leakage current is the presence of defects created by the deep etching in the edge of the annulus trench, although it does not affect the functionality of the devices as particle sensors.

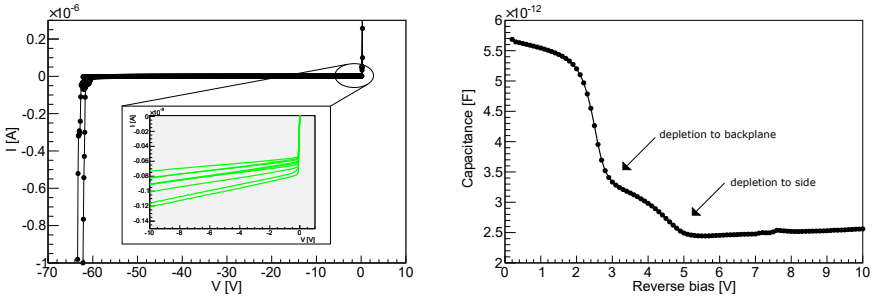

(a) **(b)**

Figure 4.17: Characterization of the 3D Cylindrical microdosimeters - (a) I-V of a single 20 µm cell and (b) C-V curves of a 11x11 array.

The capacitance-voltage characteristics were measured for some pad-type microdosimeters (arrays of $11x11$ unit cells with a common contact) as the capacitance of a unit microsensor is too low to measure accurately. Figure 4.17b shows the CV curve of an array of microsensors with 20 µm diameter. Two different depletion stages can be deduced from the plot: the first one, at about 3 V, representing the depleted volume reaching the backplane and the second one, at about 5 V, representing the depletion region reaching the lateral n-contact. Beyond 5 V the capacitance remains constant which indicates that the depleted volume is not further increased by increasing the bias voltage. The capacitance of a single microsensor in

full depletion is around 25 fF.

4.4 Experimental validation

The core of the experimental validation with the SOI microdosimetrers from IMB-CNM are the tests performed at the irradiation facilities of: Grand Accélérateur National d'Ions Lourds (GANIL) in Caen (France) and Centro Nacional de Aceleradores (CNA) in Sevilla (Spain). At CNA a charge collection efficiency study was performed with the 3D Cylindrical microdosimeter and at GANIL the U3DTHIN were tested with a carbon ion beam.

4.4.1 IBIC measurements

The 3D Cylindrical microdosimeter were taken to the Centro Nacional de Aceleradores (CNA [32]) in Sevilla and they were characterized with the IBIC (Ion Beam Induced Charge) technique [33]. In an IBIC test a MeV ion beam is scanned normally over the surface of the sensor, creating a high density of electron hole pairs in the semiconductor, and the signal corresponding to each (x,y) position is recorded event by event in a file. Hence, IBIC is an excellent technique for investigating the charge collection over all regions of a sensor.

4.4.1.1 Setup

The IBIC measurements were carried out at the microbeam line of the 3 MV Tandem accelerator of the CNA. Figure 4.18 shows the experimental setup at CNA and Table 4.2 summarizes the main characteristics of the particles from the IBIC experiment. The particles used were 1 MeV protons and 2 and 5 MeV He^{2+} ions. The ranges of these particles within silicon shown in the table have been calculated with GEANT4 Monte Carlo Toolkit [34]. The beam size for each particle was determined from the map of the Cu/(Ka) X-ray signal produced when ions are scanned

across a calibrated Cu grid. The beam delivered at the microbeam line was elliptical and the dimensions of Table 4.2 correspond to the FWHM. The particle flux at the detector was controlled with a set of four micrometric slits and it was kept below 500 Hz to avoid creating damage during the analysis.

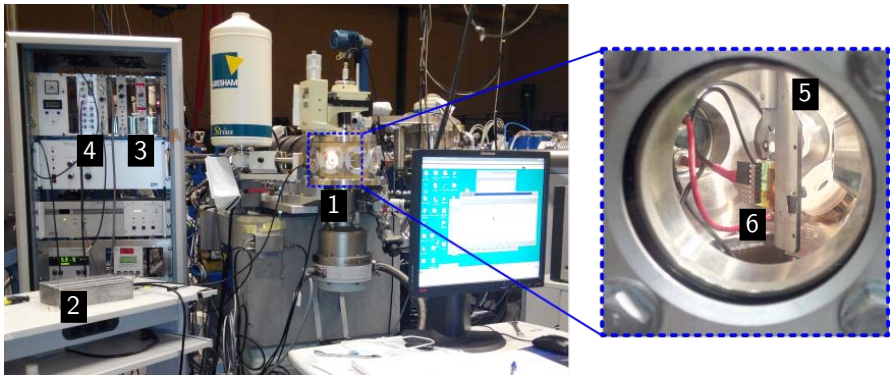

Figure 4.18: Setup at CNA at the microbeam line of the 3 MV **Tandem accelerator** - (1) Vacuum chamber with the detector, (2) Aluminum box containing the electronics, (3) Power supply for detector biasing, (4) Oxford Microbeam DAQ system (which enables to acquisition of energy spectra maps), (5) Proton beam exit and (6) Electronic board where the 3D Cylindrical microdosimeter was mounted.

Table 4.2: Characteristics of the ions used in the IBIC experiment.

Ion	Energy (MeV)	Beam size $x - y$ (µm)	Range in Si (µm)
He^2+	5.0	10 - 10	24.5±1.0
He^2+	2.0	5.9 - 5.8	7.3±0.3
H^+	1.0	4.2 - 3.5	16.6±0.8

The 3D cylindrical microdosimeter tested was a pad-type sensor (all unit cells connected to a single readout channel) with an array of 10x10 microsensors with 100 µm pitch, 20 µm diameter and manufactured on a 6 µm

SOI wafer[1]. It was placed inside a vacuum chamber during the irradiation. In all measurements the lower level discriminator of the multi-channel analyzer had to be set relatively high, above 400 keV, due to the noisy environment of the experimental area. In optimum conditions a minimum detectable energy of 12 keV has been achieved with these microdosimeters [35].

4.4.1.2 GEANT4 simulation

Previous to the charge collection efficiency measurements, and in order to verify the results, a complete simulation study of the 3D cylindrical microdosimeter was performed with the GEANT4 Monte Carlo Toolkit (version 10.1.0). The simulation code considered that all the energy deposited in the cylindrical silicon volume is collected and measured. This is not entirely accurate because there are some low efficiency areas from which the entire deposited charge in silicon is not collected, but the primary objective of the simulation was to determine how the energy is deposited in the detector in the ideal case. The simulated device, with the same thickness and layout as the fabricated detector, is shown in Figure 4.19.

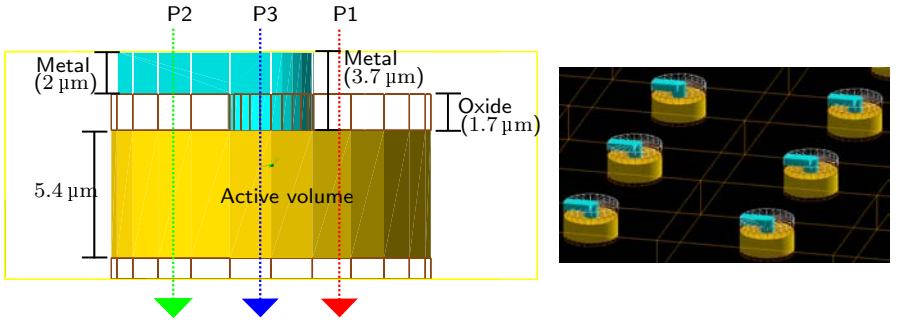

Figure 4.19: 3D cylindrical microdosimeter simulated with the GEANT4 Monte Carlo Toolkit - Left: Unit cell showing the layer composition and their thickness. Right: Part of the 10x10 microsensors array with 100 µm pitch.

[1]From Figure 4.16a a final silicon thickness of 5.4 µm can be deduced.

Figure 4.19 also shows the most probable three trajectories (particles P1, P2 and P3) of ions while passing through the sensor[1]. Due to the sensor structure, ions can travel, before reaching the silicon sensitive volume, through: (i) 1.7 µm oxide layer (P1), (ii) 2.0 µm metal layer plus 1.7 µm oxide layer (P2) or through (iii) 3.7 µm metal layer (P3). Figures 4.20, 4.21 and 4.22 show the simulated energy deposited spectra in silicon depending on the ion path for 2 MeV He^{+2}, 5 MeV He^{+2} and 1 MeV H^{+} respectively (to perform these simulations a point-like source starting at different positions was used). On the right of each figure a detailed table showing the values of the peak energy deposited[2] in each layer is also presented. A total of 1 x 10^6 events were simulated for each irradiation case, so the area under each curve is equal in all spectra.

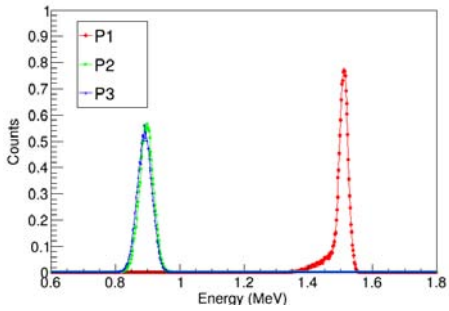

Track	$E_{deposited}$ (MeV)			
	Si (5.4 µm)	SiO_2 (1.7 µm)	Al/Cu (2.0 µm)	Al/Cu (3.7 µm)
P1	1.51±0.01	0.49±0.01	–	–
P2	0.90±0.02	0.54±0.01	0.56±0.01	–
P3	0.89±0.02	–	–	1.11±0.02

Figure 4.20: Simulated spectra of the energy deposited in the silicon sensitive volume for 2 MeV **He^{+2} particles** - The table on the right shows the energy deposited in each layer for each particle path (P1, P2 and P3).

For 2 MeV He^{2+} there is a considerable reduction on the energy deposited in the silicon when the ions pass through Al/SiO_2 or Aluminium

[1]Due to previous interactions ions can be scattered and follow different trajectories. These trajectories are taken into account in the simulations but a detailed study of each one has not been performed.

[2]The peak energy and the error are estimated as the mean and the standard deviation, respectively, of the Gaussian fit of the simulated spectra.

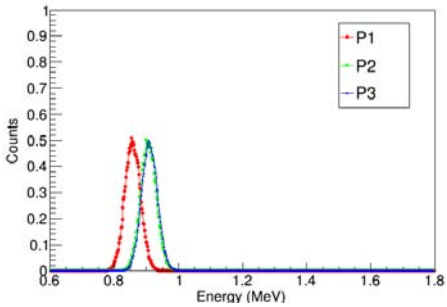

Track	$E_{deposited}$ (MeV)			
	Si (5.4 µm)	SiO_2 (1.7 µm)	Al/Cu (2.0 µm)	Al/Cu (3.7 µm)
P1	0.86±0.02	0.26±0.01	–	–
P2	0.91±0.02	0.28±0.01	0.33±0.01	–
P3	0.91±0.02	–	–	0.63±0.02

Figure 4.21: Simulated spectra of the energy deposited in the silicon sensitive volume for 5 MeV **He^{+2} particles** - The table on the right shows the energy deposited in each layer for each particle path (P1, P2 and P3).

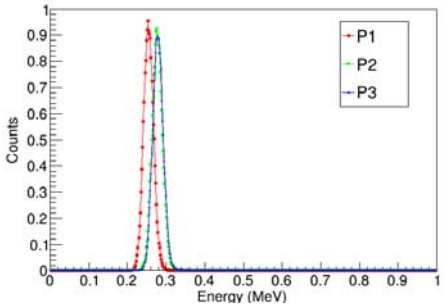

Track	$E_{deposited}$ (MeV)			
	Si (5.4 µm)	SiO_2 (1.7 µm)	Al/Cu (2.0 µm)	Al/Cu (3.7 µm)
P1	0.25±0.01	0.08±0.01	–	–
P2	0.28±0.01	0.08±0.01	0.09±0.01	–
P3	0.28±0.02	–	–	0.18±0.01

Figure 4.22: Simulated spectra of the energy deposited in the silicon sensitive volume for 1 MeV **H^{+} particles** - The table on the right shows the energy deposited in each layer for each particle path (P1, P2 and P3).

layers (P2 and P3 tracks). This reduction of approximately 600 keV is due to the low energy and thus high LET of the ions. With an energy of 2 MeV, all ions (independently of the taken path) will be stopped in the 5.4 µm of silicon, so as the ions that will pass through metal layers will lose more energy than the ones passing only through SiO_2, the energy

deposited in silicon for the non-metal path is higher. For the 5 MeV He^{2+} particles the effect is the contrary, i.e. the energy deposited in silicon for the non-metal path is lower because the particles will not be stopped inside the silicon. As in the 2 MeV case, particles that go through metal paths (P2 and P3) lose more energy in these layers than those that enter through the SiO_2 window only, therefore they enter to silicon with higher dE/dx. This implies that particles P2 and P3 deposit higher energy than particle P1 along their trajectory inside silicon. 1 MeV proton particles will also pass through the entire device so the effect is the same as the 5 MeV He^{2+} particles.

It is also important to notice that, due to the thin thicknesses of the entrance layers, the energy loss by particles in the 1.7 µm SiO_2 plus 2.0 µm Al/Cu is almost equal to the energy loss in the 3.7 µm Al/Cu. This is why in all plots of Figure 4.20, 4.21 and 4.22 the spectra of $P2$ and $P3$ tracks are almost equal.

4.4.1.3 Charge collection efficiency

The experimental results presented in this section are obtained by scanning a region of 40 x 40 μm^2 centered in one unit cell. To compare, the GEANT4 simulation setup was composed by an uniform circular beam of 20 µm diameter centered on the sensor and parallel to its surface. This simulated beam, with equal diameter as the tested unit cell, was then composed by 85% of P1 particles, 11% of P2 particles and 4% of P3 particles.

The energy spectra of the 5 MeV He^{2+} ions obtained with the detector at different bias voltages is shown in Figure 4.23a. For the 0 V bias voltage, charge collection is not complete and the energy measured is lower than the expected for a sensor thickness of 5.4 µm, in agreement with the C-V measurements (Figure 4.17b). At 3 and 5 V the spectra are identical and consistent with the simulated spectra which indicates that maximum collection efficiency has been achieved. The calculated energy deposited in the full energy peak for 3 and 5 V is (900 ± 50) keV while the simulated one is (870 ± 30) keV.

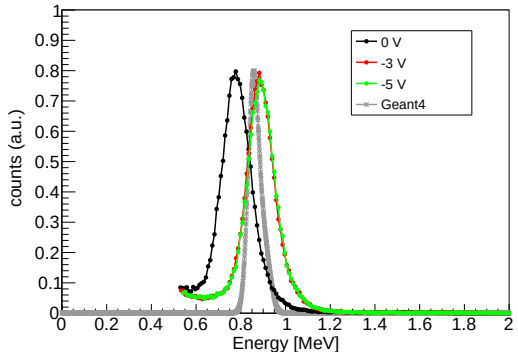

(a)

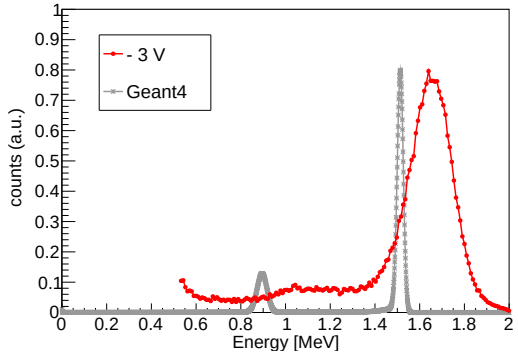

(b)

Figure 4.23: Energy spectra simulated with Geant4 and measured for - (a) 5 MeV alphas and 0, 3 and 5 V bias; (b) 2 MeV alphas and 3 V bias. Both energy spectra have been obtained scanning a region of 40 x 40 μm^2 centered in one unit cell.

Figure 4.23b shows the spectrum obtained with the 2 MeV He^{2+} ions. The two observable peaks, also predicted by Geant4 simulations, correspond to energy deposited by particles that pass through different layers. The primary peak corresponds to the alpha particles that enter the silicon through the SiO_2 layer ($P1$ from Figure 4.19) and the small peak at lower energies corresponds to the alphas that enter through the Al/SiO_2 layers and lose most of their energy before reaching the silicon ($P2$ and

$P3$ from Figure 4.19). The ratio between peak heights is equal to the ratio between areas with/without metal in the device. The experimental energy deposited in the full energy peak for 3 V is (1.6 ± 0.1) MeV while the simulated one is (1.51 ± 0.01) MeV. There is therefore a shift of the measured spectrum towards higher energies compared to the Geant4 spectrum that can be explained by an error in the energy calibration of the detector.

The low energy tails in the experimental spectra can be attributed to charge recombination in the p^+ and n^+ regions. The broadening of the peaks compared to the simulated ones is attributed to the noise within the detector and instrumentation that is not implemented in the simulation.

4.4.1.4 Effective area

The effective area of a unit cell was estimated from the event frequency map obtained with the 1 MeV proton beam. Figure 4.24 shows the map for a scan of 40 x 40 μm^2 over a single unit cell of 20 µm diameter biased at 3 V. The energy deposited by protons in the device, 0.266 keV according to Geant4 simulations, is below the noise threshold so, in order to differentiate clearly the signal from the noise, the measurement was done in pile-up conditions and the map shows events in the energy region of 0.40 to 0.60 MeV. An area of 20 µm x 20 µm is shown in the figure to mark the size and position of the microsensor.

From this map the count profiles across the microsensor in X and Y were extracted and they are shown in Figure 4.25a. The value of the effective diameter of the microdosimeter can be calculated assuming that the sensor response can be approximated by a rectangular function and the ion beam by a Gaussian function with a standard deviation of 2 µm. The convolution of these two functions should reproduce the response of the sensor. As can be seen in Figure 4.25b, the count profiles fit well with the convoluted function if the convolution is done with a rectangular function of 15 µm. The loss of 2.5 µm in each side is due to the undepleted, highly doped region near the n^+ cylindrical electrode. The expected signal

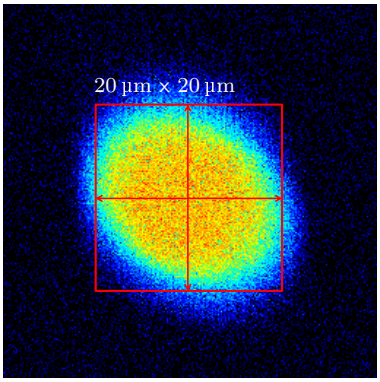

Figure 4.24: Count map obtained by a single sensitive volume biased at −3 V with the 1 MeV proton beam in pile-up mode - The IBIC scan region was 40 x 40 µm^2.

reduction in the center of the microdosimeter is not observed in Figure 4.25a due to the large size of the proton beam in relation to the diameter of the contact. Therefore, to obtain higher precision on the effective area and on the signal characteristics, a more accurate study of the sensor response should be performed with a better focused beam.

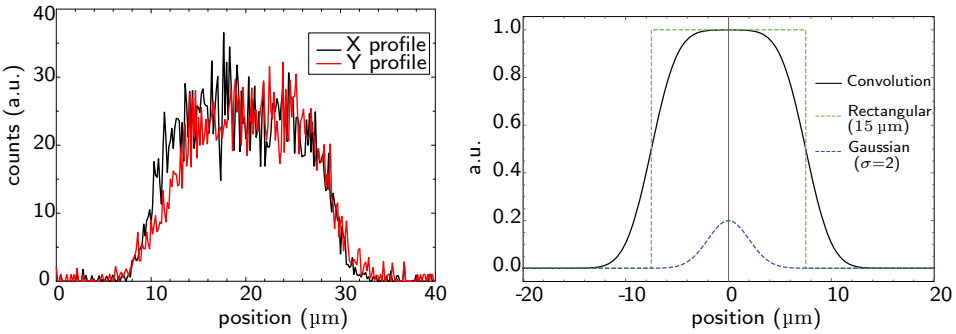

(a) **(b)**

Figure 4.25: (a) Count profiles in X and Y across an area of 40 x 40 µm centered in single microsensor. (b) Convolution of a 15 µm wide rectangular function and a σ Gaussian function.

4.4.1.5 Efficiency map

Figure 4.26 shows the event frequency map of the 10 x 10 unit cells sensor. Figure 4.26a has been taken with 5 MeV alpha particles at 5 V in the full energy peak of the spectra, in the range 0.70 to 1.30 MeV (see Figure 4.23a). Figure 4.26b was obtained with 1 MeV protons at 3 V in pile-up conditions with an energy range of 0.200 to 0.270 MeV. The high energy range values for the proton frequency map have been selected to remove the background counts due to the pile-up conditions. The scale in the map goes from zero to the maximum number of counts for the 5 minutes acquisition time. From these figures it is concluded that all unit cells are active and well defined. Moreover, no counts are located outside the sensitive regions of the microsensors meaning that they act as independent active sites. The image taken with protons shows better resolution due to the lower beam dimensions and higher number of interactions in the 5 minutes acquisition.

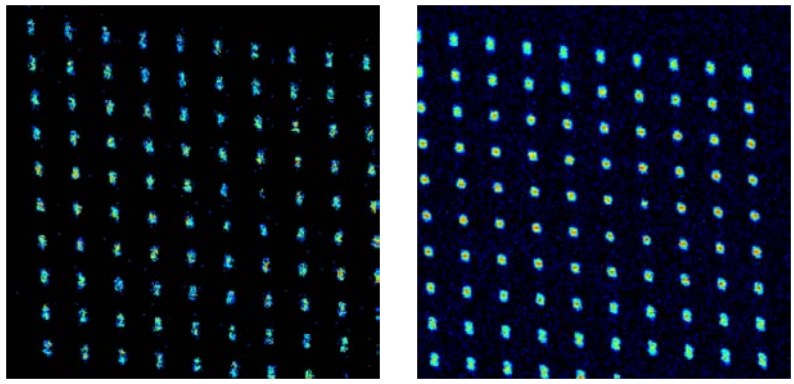

(a) **(b)**

Figure 4.26: Pixel map of 10 x 10 unit cells sensor (2 mm x 2 mm) **for** - (a) 5 MeV alpha particles with the sensor at 5 V in the full region (0.70 to 1.30 MeV). (b) 1 MeV proton particles with the sensor at 3 V in the region of 0.200 to 0.270 MeV.

Summarizing, the IBIC measurements performed at Centro Nacional

de Aceleradores (CNA [32]) in Sevilla have shown that the 3D cylindrical microdosimeters fabricated at the CNM-IMB clean room: i) are fully functional; ii) confine completely the active volume; iii) achieve full collection efficiency in the active area of the microsensor at voltages as low as 3 V and iv) undergo a 2.5 µm effective radius reduction due to the highly doped regions near the cylindrical electrode.

4.4.2 Measurements with carbon ions

The ultra-thin 3D sensors (U3DTHIN) (see section 3.4) were taken to the GANIL cyclotron facility (Caen, France) to perform measurements of microdosimetric spectra at several depths in Lucite in the central axis of a ^{12}C beam with an energy of 94.98 MeV per nucleon[1]. GEANT4 simulations were also performed to compared the obtained experimental data.

4.4.2.1 Setup

The experimental setup at GANIL was composed of a motorized remote controlled Lucite wedge system and the U3DTHIN silicon detector located in a plane perpendicular to the carbon ion beam direction (Figure 4.27). The wedge system, formed by two equal 10° angle wedges made of 1.186 g/cm^3 Lucite, provided a continuous variable thickness from 3 mm up to 30 mm with an uncertainty around 30 µm.

The ^{12}C 94.98 A MeV per nucleon beam was produced at the GANIL cyclotron facility and delivered at the G4 experimental area with primary beam relative energy resolution better than 0.5%. To provide a uniform irradiation of the detector active area, the beam profile was tuned by the cyclotron staff to have an approximate FWHM of 7 mm at the beam pipe exit window. The average fluence rate at the detector was 2.4x10^4 particles/s cm^2.

[1] On the test-beam dates, the fabrication of the 3D Cylindrical microdosimeter was still in process so no measurements were performed with them.

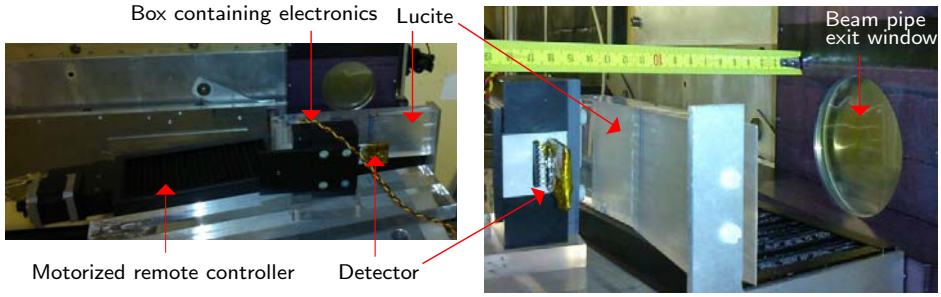

Figure 4.27: Two photographs of the experimental setup at the G4 experimental area of GANIL cyclotron facility - The U3DTHIN silicon detector was placed 16 cm away from the beam pipe exit window and the electronics was covered with aluminum to isolate it from background noise.

After noise measurements in the G4 experimental area with the ultra-thin 3D sensors, the lower level discriminator of the multichannel analyzer was set, in all measurements, approximately to 200 keV. For each depth of Lucite, a 200 s spectrum was acquired.

The tested U3DTHIN detectors had 10 µm active thickness, the supporting wafer was not removed and no biasing was applied. At 0 V bias voltage there is already a depleted cylindrical region surrounding the p^+ columns due to the built-in voltage of the p-n junction.

4.4.2.2 GEANT4 simulation

The Geant4 Monte Carlo Toolkit (version 10.1.0) has been used to perform detailed simulations of the experimental setup. The composition and properties of all the simulated materials, such as Lucite, were taken from the Geant4 National Institute of Standards and Technology (NIST) [36] database. A total of 10^5 primary events were simulated for each thickness of Lucite and the distributions of the energy deposited inside the 10 µm U3DTHIN silicon detector were obtained and stored.

Figure 4.28 shows the simulated Bragg curve of 94.98 A MeV carbon

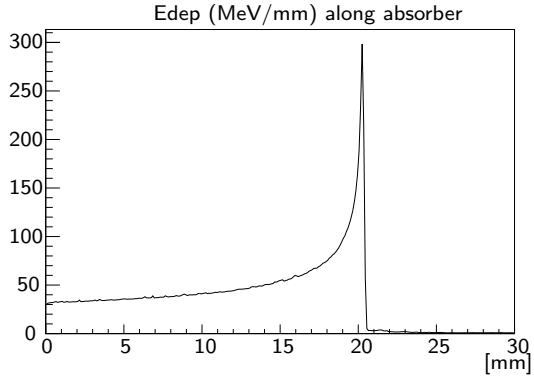

Figure 4.28: Total energy deposit (E_{dep}) by ^{12}C ions with an energy of 94.98 A MeV along 30 mm of Lucite.

ions along 30 mm Lucite (no silicon is present in this setup). This simulation is used to get an approximate value of the total energy deposited by ^{12}C ions along their trajectory inside Lucite and, from it is also deduced that the expected longitudinal range of 94.98 A MeV carbon ions in Lucite is (20.35±0.2) mm. The tail observed after the peak is due to the fragmentation processes where lower Z fragments with increasing penetration depth are created [13]. To calculate the energy imparted in the U3DTHIN detector, at several depths of Lucite, a new simulated setup including the 10 µm silicon sensor was built with the results shown in the following section.

4.4.2.3 Results

During the experiment the distributions of energy deposition in the silicon detector for several thicknesses of Lucite were measured. After data acquisition, the microdosimetric quantity lineal energy, y, (Equation 4.4) was calculated assuming that the energy imparted ε is proportional to the silicon detector signal and that the mean chord length $\bar{l}$ is approximately equal to the detector thickness for frontal irradiation. This assumption was checked through the evaluation of the track length in the 10 µm sensitive layer with GEANT4 up to the Bragg peak with deviations smaller

than 1%.

Figure 4.29 shows the simulated and calculated lineal energy y for different thicknesses of Lucite. The most probable values of the lineal energy distributions were used to build the plot. The experimental error bars took into account both the standard deviation of the Gaussian fit and the energy calibration error (see appendix C). Experimental and simulated results exhibit an excellent agreement for all points up to 19.875 mm depth in Lucite.

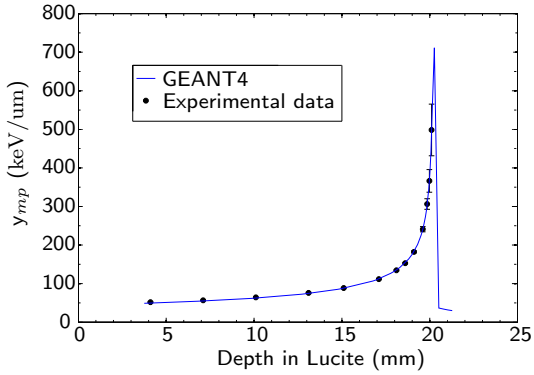

Figure 4.29: Comparison of the most probable lineal energy experimental (circles) values in the silicon detector with the GEANT4 prediction (solid line).

The maximum experimental point depicted in Figure 4.29 corresponds to 19.875 mm of Lucite because the energy distributions corresponding to higher depths do not show enough statistics to obtain a valid most probable value. Moreover, these distributions close to the Bragg peak distributions are hard to compare with GEANT4 simulations because small changes in the effective mean ionization potential, energy and range straggling and primary ionization fluctuations affect these distributions dramatically. Low statistics are obtained at these depths because most ions are stopped inside the Lucite and only few events impart energy in the silicon sensitive volume. These events are consequence of range straggling and collisions of secondary particles.

The microdosimetric distributions $f(y)$ and $y\,d(y)$ respectively, obtained from GEANT4 and experimental data for depths 4.125, 7.125, 10.125, 13.125, 15.125, 17.125, 18.125, 19.125, 19.625 and 19.875 mm are shown in Figures 4.30 and 4.31. It is important to mention that although in Figure 4.29 the agreement observed between data and simulation is excellent, the microdosimetric experimental distributions are distinguishable from the Monte Carlo ones.

In Figure 4.30 it is easy to appreciate that the experimental distributions for $f(y)$ exhibit lower peak values, and therefore higher spread of signals, than the GEANT4 simulated ones. These differences can be attributed to: i) several features of the real detectors, such as the metal lines are not simulated; ii) slight variations of the energy of the ^{12}C ions from the beam pipe exit window (in the simulations the energy was fixed to 94.98 A MeV); iii) presence of incomplete charge collection regions close to the p^+ electrode; iv) pile-up events with double pulse height in the silicon detector and and iv) noise contributions.

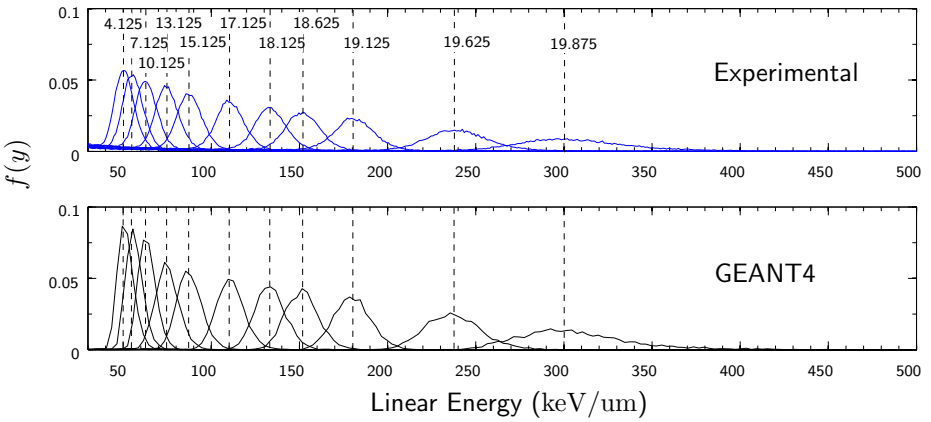

Figure 4.30: Probability distributions $f(y)$ in silicon from experimental data and GEANT4 at different depths in Lucite. Dashed lines are drawn to help in the intercomparison.

From the set of microdosimetric distributions in Figure 4.31, the dose

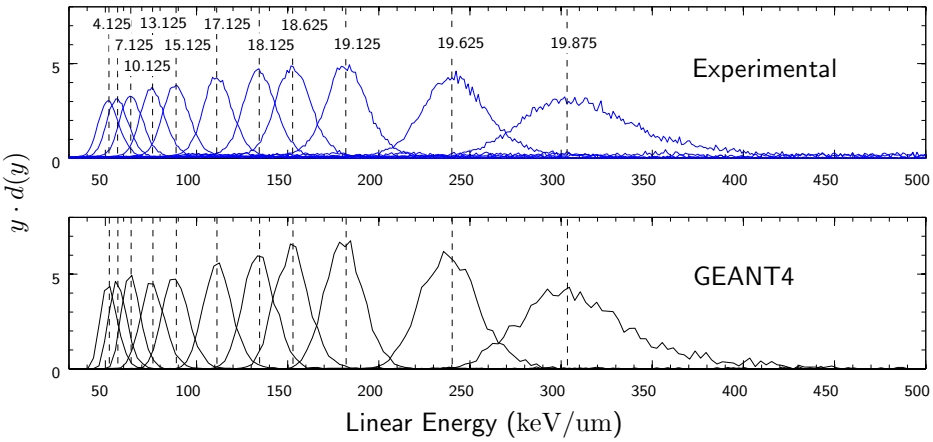

Figure 4.31: Microdosimetric distributions $yd(y)$ in silicon from experimental data and GEANT4 at different depths in Lucite. Dashed lines are drawn to help in the intercomparison.

averaged lineal energy $\bar{y}_D$ can be computed to obtain a good comparison of the different simulations and measurements. Is it important to understand that when energy-loss straggling and delta-ray escape from the studied volume are not very relevant, the $\bar{y}_D$ value is very close to dose averaged LET [37]. Of course this statement implies that the ionizing particle range is significantly higher than the scoring region i.e, the region where the charge is collected. The agreement between the experimental data and GEANT4 shown in Figure 4.32 is better than 5% up to the Bragg-peak. The differences observed correspond to the small shape variations of the microdosimetric distributions both from Monte Carlo and data (Figure 4.30). The presence of few counts for very large y values was also a source of uncertainty for the evaluation of $\bar{y}_D$.

A complete comparison of the experimental results with GEANT4 and FLUKA Monte Carlo code can be found in [38].

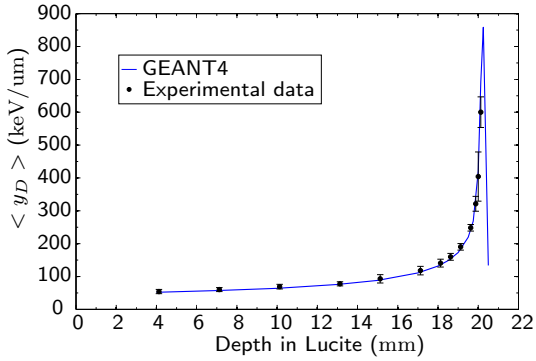

Figure 4.32: Dose averaged lineal energy computed from GEANT4 and experimental data.

Bibliography

[1] Dieter Schardt. *Hadrontherapy*, pages 55–86. Springer International Publishing, Cham, 2016. 136

[2] Robert R. Wilson. **Radiological Use of Fast Protons**. *Radiology*, **47**(6), 1946. 136

[3] **Particle Therapy Co-Operative Group PTCOG. [Updated June 2014]**. 136

[4] **Particle Therapy Co-Operative Group PTCOG. [Updated May 2016]**. 136

[5] **Agency for Research on Cancer (IARC). World cancer report 2014**. 136

[6] C Timlin and B Jones. **Proton and Charged Particle Radiotherapy**. *The British Journal of Radiology*, **83**(985):87, jan 2010. 136

[7] Marco Durante and Jay S Loeffler. **Charged particles in radiation oncology**. *Nat Rev Clin Oncol*, **7**(1):37–43, jan 2010. 136

[8] **National Institute of Radiological Sciences (NIRS). Research Center for Charged Particle Therapy**. 137

[9] Thomas E Goffman and Eli Glatstein. **Intensity-Modulated Radiation Therapy**. *Radiation Research*, **158**(1):115–117, jul 2002. 138

[10] M. Durante and J. S. Loeffler. **Charged particles in radiation oncology.** *Nature reviews. Clinical oncology*, **7**(1):37–43, 2010. 138

[11] Uli Weber and Gerhard Kraft. **Comparison of carbon ions versus protons.** *Cancer journal (Sudbury, Mass.)*, **15**(4):325–332, 2009. 139

[12] D Schardt, I Schall, H Geissel, H Irnich, G Kraft, A Magel, M F Mohar, G Münzenberg, F Nickel, C Scheidenberger, W Schwab, and L Sihver. **Proceedings of the Meetings F2.6 and F2.7 of COSPAR Scientific Commission F which was held during the Thirtieth COSPAR Scientific Assembly Nuclear fragmentation of high-energy heavy-ion beams in water**. *Advances in Space Research*, **17**(2):87–94, 1996. 139

[13] B. Braunn, M. Labalme, G. Ban, M. Chevallier, J. Colin, D. Cussol, D. Dauvergne, J. M. Fontbonne, F. Haas, A. Guertin, D. Lebhertz, F. Le Foulher, C. Pautard, C. Ray, M. Rousseau, M. D. Salsac, L. Stuttge, E. Testa, and M. Testa. **Nuclear reaction measurements of 95 MeV/u 12C interactions on PMMA for hadrontherapy**. *Nuclear Instruments and Methods in Physics Research, Section B: Beam Interactions with Materials and Atoms*, **269**(22):2676–2684, 2011. 139, 171

[14] Harald H. Rossi and Marco Zaider. *Microdosimetry and Its Applications*. Springer, 1996. 139

[15] Tomas Kron, Joerg Lehmann, and Peter B Greer. **Dosimetry of ionising radiation in modern radiation oncology**. *Physics in Medicine and Biology*, **61**(14):R167, 2016. 139

[16] IAEA and ICRU. **Relative Biological Effectiveness in Ion Beam Therapy**. *IAEA Technical Reports*, (461):1–165, 2008. 140

[17] W K Weyrather and G Kraft. **RBE of carbon ions: Experimental data and the strategy of RBE calculation for treatment planning**. *Radiotherapy and Oncology*, **73**:S161 – S169, 2004. 141

[18] **Microdosimetry. ICRU report 36**. 1983. 141, 144, 146

[19] P. D. Bradley. *The development of a novel silicon microdosimeter for high LET radiation therapy*. PhD thesis, 2000. 143, 145, 148

[20] V Conte Nardo, P Colautti, B Grosswendt, D Moro, and L De. **Track structure of light ions: experiments and simulations**. *New Journal of Physics*, **14**(9):93010, 2012. 144

[21] R.F . Shonka, J. E. Rose, and G. Failla. **Conducting plastic equivalent to tissue, air and polystyrene**. In *Second Unitaed Nations International Conference on Peaceful Uses of Atomic Energy*, page 160, New York, 1958. 146

[22] D Srdoc. **Experimental technique of measurement of microscopic energy distribution in irradiated matter using Rossi counters.** *Radiation research*, **43**(2):302–319, aug 1970. 146

[23] L Lindborg, J E Kyllonen, P Beck, J F Bottollier-Depois, S Gerdung, R E Grillmaier, and U Schrewe. **The use of TEPC for reference dosimetry.** *Radiation protection dosimetry*, **86**(4):285–288, 1999. 146

[24] J Burmeister, C Kota, R L Maughan, A J Waker, K Riley, and L Wielopolski. **Application of TEPC microdosimetry to boron neutron capture therapy.** *Radiation protection dosimetry*, **99**(1-4):351–352, 2002. 146

[25] D Perez-Nunez and L A Braby. **Replacement tissue-equivalent proportional counter for the International Space Station.** *Radiation protection dosimetry*, **143**(2-4):394–397, feb 2011. 146

[26] L De Nardo, V Cesari, G Dona, G Magrin, P Colautti, V Conte, and G Tornielli. **Mini-TEPCs for radiation therapy.** *Radiation protection dosimetry*, **108**(4):345–352, 2004. 146, 147

[27] H H Rossi and W Rosenzweig. **A device for the measurement of dose as a function of specific ionization.** *Radiology*, **64**(3):404–411, mar 1955. 147

[28] P. D. Bradley, a. B. Rosenfeld, and M. Zaider. **Solid state microdosimetry**. *Nuclear Instruments and Methods in Physics Research, Section B: Beam Interactions with Materials and Atoms*, **184**:135–157, 2001. 148

[29] S. Guatelli, M. I. Reinhard, B. Mascialino, D. A. Prokopovich, A. S. Dzurak, M. Zaider, and A. B. Rosenfeld. **Tissue equivalence correction in silicon microdosimetry for protons characteristic of the LEO space environment**. *IEEE Transactions on Nuclear Science*, **55**(6):3407–3413, 2008. 148

[30] Linh T Tran, Student Member, Susanna Guatelli, Dale a Prokopovich, Marco Petasecca, Michael L F Lerch, Mark I Reinhard, James F Ziegler, Marco Zaider, Anatoly B Rosenfeld, and Senior Member. **A Novel Silicon Microdosimeter Using 3D Sensitive Volumes : Modeling the Response in Neutron Fields Typical of Aviation**. **61**(4):1552–1557, 2014. 148

[31] C. Guardiola, D. Quirion, G. Pellegrini, C. Fleta, S. Esteban, M. a. Cortés-Giraldo, F. Gómez, T. Solberg, a. Carabe, and M. Lozano. **Silicon-based three-dimensional microstructures for radiation dosimetry in hadrontherapy**. *Applied Physics Letters*, **107**(2):023505, 2015. 149

[32] **Centro Nacional de Aceleradores. http://acdc.sav.us.es/cna/**. 159, 169

[33] M B H Breese, E Vittone, G Vizkelethy, and P J Sellin. **A review of ion beam induced charge microscopy**. *Nuclear Instruments and Methods in Physics Research Section B: Beam Interactions with Materials and Atoms*, **264**(2):345–360, 2007. 159

[34] S Agostinelli, J Allison, and K Amako. **Geant4-a simulation toolkit**. *Nuclear Instruments and Methods in Physics Research A*, **506**:250–303, 2003. 159

[35] C Guardiola, D Quirion, G Pellegrini, C Fleta, S Esteban, M A Cortés-Giraldo, F Gómez, T Solberg, A Carabe, and M Lozano. **Silicon-based three-dimensional microstructures for radiation dosimetry in hadrontherapy**. *Applied Physics Letters*, **107**(2), 2015. 161

[36] **NIST. Physical reference data website**. 170

[37] A M Kellerer. **Fundamentals of microdosimetry**. In K R Kase, B E Bjärngard, and F H Attix, editors, *The Dosimetry of Ionizing Radiation*, pages 77–162. Academic Press, 1985. 174

[38] F Gomez, C Fleta, S Esteban, D Quirion, G Pellegrini, M Lozano, Y Prezado, M Dos Santos, C Guardiola, G Montarou, J Prieto-Pena, and Juan Pardo-Montero. **Measurement of carbon ion microdosimetric distributions with ultrathin 3D silicon diodes.** *Physics in medicine and biology*, **61**(11):4036–4047, jun 2016. 174

Part IV

General Conclusions

5

Conclusions and Future Work

5.1 Conclusions

The work developed in this thesis is divided in two sections; one dedicated to sensors for neutron detection and the other dedicated to sensors for microdosimetric measurements. In both sections the simulations, design, fabrication, characterization and experimental validation of the fabricated sensors at the IMB-CNM clean room are covered.

The silicon sensors from the first section are the ultra-thin 3D and the microstructured sensors, which are covered and filled respectively with a

converter material to detect neutrons. The sensors from the second section are again the ultra-thin 3D and the 3D cylindrical microdosimeter.

Chapter 2 describes the basic working principle of Monte Carlo methods of radiation transport and explains the general properties of the GEANT4 simulation package. GEANT4 was used during all the stages of this thesis and in order to achieve higher level of accuracy the production cut value for the tracking of secondary particles was set to 0.1 µm in all cases. To accurately simulate the thermal neutron detectors the employed physics list was the QGSP_BERT_HP which includes the G4NeutronHPElastic, the
G4NeutronHPInelastic and the G4NeutronHPCapture high precision models. Moreover, all cross-section data for low energy neutron interactions (thermal to 20 MeV) were taken from ENDF/B-VI library. To simulate the experiments performed with the silicon microdosimeters the QGSP_BIC physics list, with the G4EmLivermorePhysics to manage the electromagnetic processes, was used. This physics list was specifically created to address simulations for which high level of accuracy is required, as it is the case in medical applications.

Chapter 3 overviews the fabrication process, the electrical characterization and the experimental validation of the ultra-thin 3D and the microstructured sensors. For the U3DTHIN detectors, the boron carbide 99% enriched in ^{10}B ($^{10}B_4C$) and the BE10 screen converter materials were used to detect thermal neutrons from the Portuguese Research Reactor (RPI). Moreover, sensor were also adapted for fast neutron detection using a polyethylene sheet placed on their front surface. For an LLD value of 200 keV and a bias voltage of 30 V, the measured intrinsic efficiency was 1.75% and 0.94% for the 2.7 µm $^{10}B_4C$ and the BE10 screen respectively. For the same LLD value, experimental tests realized at the fast neutron port with the U3DTHIN with the polyethylene sheet showed an efficiency of 0.06%. The obtained results, in good agreement with GEANT4 simulations, demonstrate the feasibility of using the U3DTHIN sensors for thermal neutron detection with a high γ-ray rejection. Due to the thin

active silicon thickness, the U3DTHIN sensor can be useful for mixed γ-n radiation environments, like in radiotherapy rooms where active detectors can not be easily used due to the complex characteristics of the mixed γ-n field.

For the microstructured sensors, a new compound found in the Lithium-ion battery manufacturing industry was used to fill the sensor trenches. According to SEM images, this compound showed good packaging density without voids inside the trenches. Microstructured sensors filled with boron-10 were not tested in the RPI due to high noise levels in the reactor area ($\approx$450 keV) and the measurements were focused on ^{6}LiF filled sensors. Thermal neutron tests of the first fabricated batch at different irradiation angles were performed and the maximum efficiency for a detector of 25 µm trench width biased at 3 V was 8.6% for front-side irradiation. Measurements at different angles showed the angular dependency of the efficiency and the effect of the PCB, that contains boron oxide, and when neutrons pass through it there are a percentage of neutrons that are absorbed. The microstructured sensors are more cost - effective than helium-3 based neutron detectors and have several different applications like medical imaging and homeland security (e.g., border screening).

Chapter 4 presents the fabrication, simulation and charge collection characteristics of the 3D cylindrical microdosimeters fabricated at the IMB-CNM clean room. Charge collection measurements showed that: i) a 3 V bias voltage completely deplete the detector and maximum collection efficiency is achieved; ii) the sensitive diameter of each unit cell is reduced 5 µm due to the undepleted, highly doped region near the n^{+} cylindrical electrode and iii) all unit cells of the microdosimeter are active and well defined i.e., no counts are located outside the sensitive volumes. Moreover, this chapter also shows the measurements of the microdosimetric distributions of a carbon ion beam performed with the U3DTHIN detectors. Even though the U3DTHIN detectors were originally designed for plasma diagnostic and neutron detection, they have been also investigated and tested as solid state microdosimeters due to their thin and well defined active

volume. The experimental results of the microdosimetric lineal energy spectra $y\,d(y)$ compared to those obtained with GEANT4 show excellent agreement for the most probable lineal energy values as a function of depth and, considering the dose averaged lineal energy, the agreement is better than 4%. The silicon-based microdosimeters presented in this thesis can be used to determine the microdosimetric properties and the dose distributions along ion beams. Moreover, using the pixel configuration of the 3D cylindrical microdosimeters a dose distribution in the perpendicular plane of the beam can be obtained and used to minimize the normal tissue irradiation around the cancer volume.

5.2 Ongoing and future work

There are several important issues, emerged during the last period of this thesis, that have to be covered in the near future to continue the research lines of both neutron detection and microdosimetric measurements. In this section, this required future work will be explained separately for each kind of detector.

The fabrication technology of the ultra-thin 3D silicon sensors is well established and no improvements are necessary, however due to the relatively low neutron efficiency obtained with a single sensor, experiments with multiple stacked sensors could be also performed if high efficiency is required.

For the microstructured sensors, the ongoing work is related with the development of a semi-automatized filling method to apply on whole wafers. Up to now, the sensors are filled individually with the handpacking method and care is required when applying the pressure for not damaging the silicon walls. An improved filling method should be developed to fill all sensor of the manufactured wafer by applying a constant pressure in each one with no damage risk, a key requirement for future mass-production. Concerning the experimental test of the ^{6}LiF filled microsensors, irradiation in a neutron beam should be also performed to study the angular

dependance of the designed pattern.

Effort has been also made in the development of a new readout electronics to reduce the electronic noise. Two new designs has been recently assembled by the IMB-CNM radiation group and noise measurements with different sensors are under process. These two new electronics keep the old design but incorporate Cremat and Amptek amplifier modules respectively to achieve a better amplification stage with improved signal-to-noise ratio.

The ultra-thin 3D sensors working as solid state microdosimeters have been tested successfully in a carbon ion beam however, new measurements with no silicon support below the active area of the U3DTHIN should be done. The etching process to remove the silicon support has been already performed in the IMB-CNM clean room and measurement with these sensors would let a comparison to study the contribution of backscattered particles to the charge collection.

For the 3D cylindrical microdosimeters the main aspect to be covered is the utilization of a data acquisition system for the parallel readout of each unit cell of the sensor. In this thesis, the presented experimental results have been obtained using the pad configuration of the 3D cylindrical microdosimeters, where only one output signal was obtained for all unit cells. However, to read and to obtain an energy deposit spectrum of each unit cell, a more sophisticated readout system able to handle many channels is required. First test have already been done with a data acquisition board (MADDAQ) [1] based on the VATAGP7, a 128-channel charge sensitive amplifier. Despite the fact that the obtained results are promising, further work is required to implement this electronics to the pixel structure of the 3D cylindrical microdosimeters.

Finally, in a near future a new fabrication of 3D cylindrical microdosimeters will be manufactured and some work needs to be done to improve their design based on the results obtained with this research. Moreover, the fabrication process needs to be optimized, with respect to the first fabrication batch, to avoid the problems that arose due to its

innovative design and its micrometric dimensions.

Bibliography

[1] V Stankova, C Lacasta, G Llosá, V Linhart, V Cindro, B Grošičar, M Mikuž, A Studen, D Žontar, D Burdette, E Chesi, E Cochran, K Honscheid, H Kagan, P Weilhammer, N H Clinthorne, S Huh, and C Solaz. **An FPGA based DAQ system for the readout of Madeira PET probe**, 2010. 187

Appendix A

Electrical characterization

To ensure the correct performance and electrical response of the fabricated devices, the detectors are electrically tested with current - voltage and capacitance - voltage measurements. The measurements of current - voltage give information of the leakage current[1] and the breakdown voltage of the detectors while the capacitance - voltage curves give the value of the full depletion voltage, the detector capacitance and the effective doping profile of the detector.

The electrical characterization of the detectors was performed in the IMB-CNM laboratory shown in Figure A.1. The current - voltage characterization were made with a Cascade probe station biasing the detectors with a 2410 Keithley power supply at a controlled temperature of 20 °C and with an N_2 flow to reduce humidity. The capacitance voltage measurements were made with an Agilent 4284A LCR Meter in R-C parallel mode using a signal with a frequency of 10 kHz and an oscillation voltage of 500 mV.

To obtain the I-V and C-V characteristics of the fabricated devices, the reverse bias configuration was used. Therefore a voltage scan from 0 to negative voltage values was realized with the p-type region connected to

[1] Leakage current depends on the bias voltage and the temperature and limits the smallest signal pulse that can be taken as detector output.

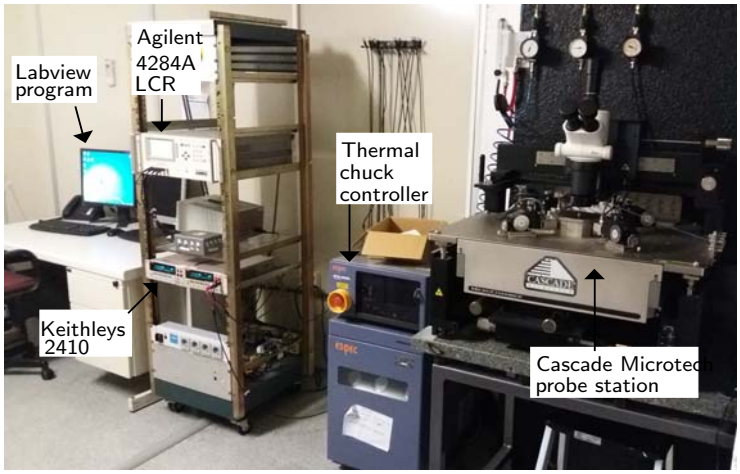

Figure A.1: IMB-CNM characterization lab used for the electrical characterization - The set-up consists of: a probe station (Cascade Microtech model), a Thermal chuck, two power supplies (Keithley 2410) (one is used for the central diode and the other for the guard ring if needed), an Agilent 4284 LCR Meter and a PC with the TCL program.

the negative terminal of the Keithley and the n-type region to the positive (ground) terminal.

Appendix B

Readout electronics

When an quantum of ionizing radiation goes through the sensor, it creates $e^{-}h^{+}$ pairs that, when collected in the electrodes, induce a small electrical current pulse that must be amplified correctly. This is done by a combination of preamplifier, shaper and amplifier electronics.

Figure B.1 shows a sketch of the main components of a readout electronics where: i) the sensor converts the energy deposited by a particle to an electrical signal; ii) the preamplifier, configured as an integrator, converts the narrow current pulse in a voltage pulse large enough to be treated and adapted with the minimum noise level possible; iii) the subsequent CR high-pass filter introduces the desired decay time and the RC low-pass filter limits the bandwidth and sets the rise time. These two filters attenuate the signal at high and low frequencies where there is no useful information, improving the signal-to-noise ratio.

During the process of signal adaptation and shaping, the signal is attenuated so it is necessary to incorporate an amplifier stage. This stage is designed so that the amplitude of the output pulse of the system is proportional to the energy deposited by the incident particles in the detector.

Figure B.2 shows the designed readout system for the IMB-CNM sensors. It consists of a portable readout electronics that integrates the function of preamplifier, amplifier and pulse shaping in only one electronic

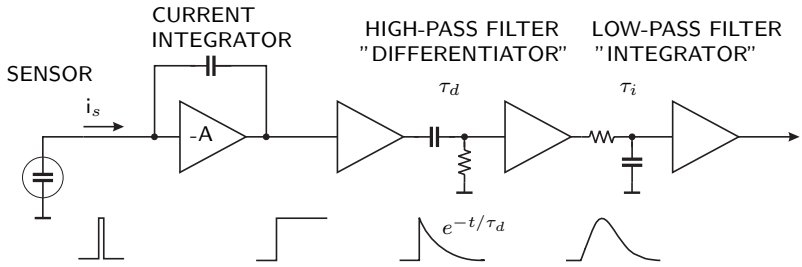

Figure B.1: Basic sketch of the readout electronics for a radiation detector.

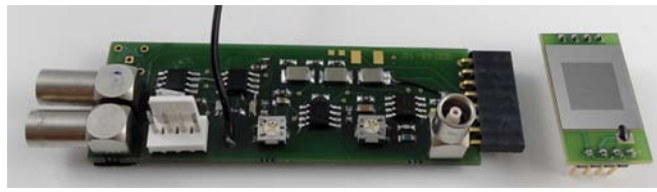

Figure B.2

Figure B.3: Photograph of the portable readout electronics - The portable electronics is 10 cm length and a silicon sensor glued to a board that will be connected to the readout electronics is also shown on the right of the picture.

board powered by ±5 V. In this system, the parameters of the amplification stages can be adapted or changed easily in order to use the system with different types of detectors and particles, with different input signals. The silicon semiconductor sensor is connected in a different board to allow the user to test different sensors with the same readout system.

Figure B.4 shows in detail the electronic diagram of the total integrated system. To obtain the spectrum of the measured radiation, this electronics is combined with a computer-controlled multichannel pulse-height analyzer (MCA) which is previously calibrated in energy through the injection of an electronic pulse (see appendix C).

Two other readout electronics have been recently assembled by the IMB-CNM radiation group with the aim of improving the signal-to-noise

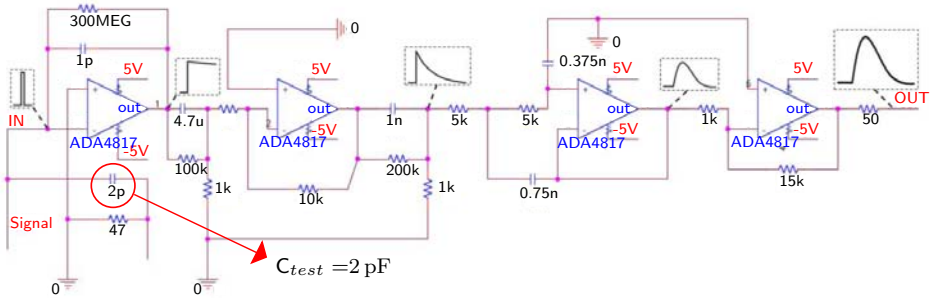

Figure B.4: Electronic diagram of the readout electronics - with preamplifier, amplifier and pulse shaping. The test capacimeter to perform the energy calibration is also depicted on the diagram.

ratio. Calibrations and noise measurements with different manufactured sensors in the institute laboratory are still in process so no experimental results will be presented in this thesis with these new electronics. The readout electronics have been assembled with preamplifier and shaping modules from Amptek, Inc. and Cremat, Inc products respectively.

Appendix C

Energy calibration

To obtain the spectrum of the measured radiation, the output signal of the readout electronics was connected to an Amptek MCA8000A Multichannel Analyzer. The default spectrum provided by MCA is displayed in counts vs. channels so an energy calibration needs to be done to get the energy-spectrum. This calibration was made with the injection of an square electronic pulse across a 2 pF test capacitance in the PCB (see Figure B.4).

The injected voltage pulse simulates the sensor output signals, i.e. simulates the detection of a nuclear particle interaction in a semiconductor sensor. The relation between the voltage of the injected pulse and the energy that it simulates is 22.25 mV=1 MeV because: the energy required to create an electron-hole pair in silicon is ε=3.6 eV so, an energy deposit of 1 MeV will create $2.78{\cdot}10^5$ electrons or $4.45{\cdot}10^{-}14$ C. To simulate this energy deposit across the 2 pF test capacimeter, a voltage of $V = Q/C$ =22.25 mV is required. The error associated to this calibration basically depends on the capacitance's value and other factor like the accuracy of the peak determination. For our case an error of ± 5 channels in the peak position is considered in all calibrations.

Figure C.1 shows the used setup for the energy calibration. The calibration was done for each kind of detector and, in some cases, for different

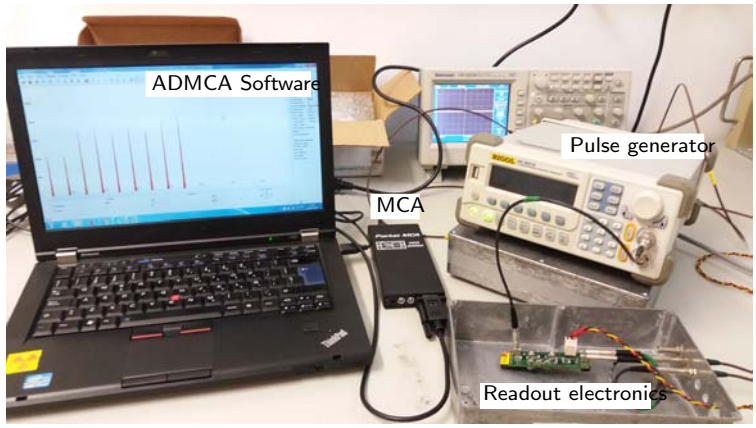

Figure C.1: Setup used for the energy calibration - It consists of: a pulse generator connected to the readout electronics, a MCA multichannel analyzer and a PC with the ADMCA Display and Acquisition Software. In the computer screen different pulses of different pulse voltages are displayed.

bias voltages due to the influence of the sensor capacitance in the peak position.

Scientific contributions

Publications

- **S. Esteban**, C. Fleta, C. Guardiola, C. Jumilla, G. Pellegrini, D. Quirion, J. Rodriguez, M. Lozano, *Microstructured silicon neutron detectors for security applications*, Journal of Instrumentation, 10^{th} International Conference on Position Sensitive Detectors, September 2014.

- C. Fleta, C. Guardiola, **S. Esteban**, C. Jumilla, G. Pellegrini, D. Quirion, J. Rodríguez, A. Lousa, L. Martínez-de-Olcoz, M. Lozano, *Fabrication and nuclear reactor tests of ultra-thin 3D silicon neutron detectors with a boron carbide converter*, Journal of Instrumentation, doi: 10.1088/1748-0221/9/04/P04010, March 2014.

- C. Guardiola, A. Carabe, F. Gómez, G. Pellegrini, C. Fleta, **S. Esteban**, D. Quirion, M. Lozano, *First silicon microdosimeters based on cylindrical diodes*, Sensors and Transducers, Vol. 183, December 2014.

- C. Fleta, C. Guardiola, **S. Esteban**, G. Pellegrini, D. Quirion, J. Rodriguez, F. Gomez, A. Carabe-Fernández, M. Lozano, *First investigations of Ultra-Thin 3D silicon detectors as microdosimeters*, Radiotherapy and Oncology, ICTR-PHE - 2014, http://dx.doi.org/10.1016/S0167-8140(15)34093-7

- C. Guardiola, D. Quirion, G. Pellegrini, C. Fleta, **S. Esteban**, M.A. Cortés-Giraldo, F. Gómez, T. Solberg, A. Carabe, M. Lozano, *Silicon-based three-dimensional microstructures for radiation dosimetry in hadrontherapy*, Applied Physics Letters, doi: http://dx.doi.org/10.1063/1.4926962, June 2015.

- C. Fleta, **S. Esteban**, M. Baselga, D. Quirion, G. Pellegrini, C. Guardiola, M.A. Cortés-Giraldo, J. García López, M.C. Jiménez Ramos, F. Gómez, M. Lozano, *3D cylindrical silicon microdosimeters: fabrication, simulation and charge collection study*, Journal of Instrumentation, doi: 10.1088/1748-0221/10/10/P10001, September 2015.

- F. Gómez, C. Fleta, **S. Esteban**, D. Quirion, G. Pellegrini, M. Lozano, Y. Prezado, M. Dos Santos, C. Guardiola, G. Montarou, J. Prieto-Pena, J. Pardo-Montero, *Measurement of carbon ion microdosimetric distributions with ultrathin 3D silicon diodes*, Physics in medicine and biology, doi: 10.1088/0031-9155/61/11/4036, May 2016.

Conferences

- *Microstructured silicon neutron detectors for security applications*, PSD 10, 10th International Conference on Position Sensitive Detectors, 7-12 September 2014, University of Surrey, U.K. (Poster session).

- *Simulation and fabrication of pixel neutron detectors*, 17^{th} iWoRiD, International Workshop on Radiation Imaging Detectors, 28 June - 02 July 2015, DESY, Hamburg, Germany (Poster session).

- *Microdosímetros de silicio basados en diodos cilíndricos*, XXXV Reunión Bienal de la Sociedad Espaola de Física, 13 -17 June 2015, Gijón, Spain (Oral presentation).

Participation in Projects

- **REWARD**: Real-time Wide-Area Radiation Surveillance System
  Granted by: 7th Framework Programme for Research (FP7-SEC-2011-1)
  Directed by: Manuel Lozano Fantoba (IMB-CNM)

- **NEUS**: Neutron Detector and Imaging System
  Co-funded by: European Fund for Regional Development (FEDER)